

**DESIGN OF THERMOPLASTIC COMPOSITE MANUFACTURING WITH
AUTOMATED FIBER PLACEMENT TOWARDS IN-SITU CONSOLIDATION**

by
ALI BARZEGAR OSGOUEI

Submitted to the Graduate School of Engineering and Natural Sciences
in partial fulfilment of
the requirements for the degree of Doctor of Philosophy

Sabanci University

December 2024

ALI BARZEGAR OSGOUEI 2024 ©

All Rights Reserved

ABSTRACT

DESIGN OF THERMOPLASTIC COMPOSITE MANUFACTURING WITH AUTOMATED FIBER PLACEMENT TOWARDS IN-SITU CONSOLIDATION

ALI BARZEGAR OSGOUEI

Manufacturing Engineering, Ph.D. Thesis, December 2024

Thesis Supervisor: Assoc. Prof. Dr. Hatice Sinem ŞAŞ ÇAYCI

Thesis Co- Supervisor: Prof. Dr. Mehmet YILDIZ

Keywords: Laser-Assisted Fiber Placement (LAFP), Thermoplastic Composites, In-Situ Consolidation, Process Modeling, Composite Manufacturing Optimization

The increasing demand for lightweight, high-performance materials in the aerospace sector has driven the evolution of advanced manufacturing techniques for thermoplastic composites. This thesis focuses on the design and optimization of thermoplastic composite manufacturing using Automated Fiber Placement (AFP) with an emphasis on in-situ consolidation. A systematic approach is undertaken to address the challenges associated with the AFP process, including temperature distribution, degree of intimate contact, interlaminar bonding, and multi-scale permeability.

The research employs a combination of experimental and numerical methods to evaluate and enhance the thermal and mechanical performance of carbon fiber/polyetherketoneketone (CF/PEKK) composites. Key studies include the development and validation of thermal models incorporating thermal contact resistance to predict temperature histories during layup. Experimental investigations quantify the effects of fiber orientation and layup speed on the degree of intimate contact and interlaminar bonding strength. Novel correction factors for bonding prediction models are introduced to improve the accuracy of process outcomes.

Results reveal that optimized thermal and mechanical conditions significantly improve bonding quality and reduce void formation. Multi-scale permeability analysis using pulse-decay and micro-computed tomography methods highlights the interplay between process parameters and microstructural properties. The findings contribute to the broader understanding of AFP process dynamics, paving the way for sustainable, efficient manufacturing of high-performance thermoplastic composites.

The study concludes with recommendations for process optimization and avenues for future research to further enhance the application of AFP in thermoplastic composite production. This work provides a comprehensive framework for integrating advanced manufacturing techniques with materials science to meet industry requirements.

ÖZET

OTOMATİK ELYAF YERLEŐTİRME İLE YERİNDE KONSOLİDASYONA YÖNELİK TERMOPLASTİK KOMPOZİT ÜRETİMİNİN TASARIMI

ALI BARZEGAR OSGOUEI

Üretim Mühendisliđi, Doktora Tezi, Aralık 2024

Tez Danışmanı: Doç. Dr. Hatice Sinem ŞAŞ ÇAYCI

Tez Eş-Danışmanı: Prof. Dr. Mehmet YILDIZ

Anahtar Kelimeler: Lazer Destekli Elyaf Yerleőtirme (LAFP), Termoplastik Kompozitler, Yerinde Konsolidasyon, Süreç Modellemesi, Kompozit Üretim Optimizasyonu

Havacılık sektöründe hafif ve yüksek performanslı malzemelere olan artan talep, termoplastik kompozitlerin ileri üretim tekniklerinin gelişimini tetiklemiştir. Bu tez, yerinde konsolidasyon vurgusuyla Otomatik Elyaf Yerleőtirme (AFP) kullanılarak termoplastik kompozit üretiminin tasarımı ve optimizasyonuna odaklanmaktadır. AFP süreciyle ilgili sıcaklık dağılımı, yüzey teması derecesi, tabakalar arası bağlanma ve çok ölçekli geçirgenlik gibi zorlukları ele almak için sistematik bir yaklaşım benimsenmiştir.

Araştırmada, karbon fiber/polieterketonketon (CF/PEKK) kompozitlerinin termal ve mekanik performansını değerlendirmek ve geliőtirmek amacıyla deneysel ve sayısal yöntemlerin bir kombinasyonu kullanılmaktadır. Anahtar çalışmalar, serim sırasında sıcaklık geçmişlerini tahmin etmek için termal temas direncini içeren termal modellerin geliştirilmesini ve doğrulanmasını kapsamaktadır. Deneysel araştırmalar, fiber yönelimi ve serim hızının yüzey teması derecesi ve tabakalar arası bağlanma dayanımı üzerindeki etkilerini nicel olarak belirlemektedir. Bağlanma tahmin modelleri için yenilikçi düzeltme faktörleri, süreç sonuçlarının doğruluđunu artırmak amacıyla sunulmaktadır.

Sonuçlar, optimize edilmiş termal ve mekanik koşulların bağlanma kalitesini önemli ölçüde artırdığını ve boşluk oluşumunu azalttığını ortaya koymaktadır. Darbe-boşalma ve mikro-bilgisayarlı tomografi yöntemleri kullanılarak yapılan çok ölçekli geçirgenlik analizi, süreç parametreleri ile mikro yapısal özellikler arasındaki ilişkiyi vurgulamaktadır. Bulgular, AFP süreç dinamiklerinin daha iyi anlaşılmasına katkıda

bulunarak, yüksek performanslı termoplastik kompozitlerin sürdürülebilir ve verimli üretimi için yol açmaktadır.

Çalışma, termoplastik kompozit üretiminde AFP'nin uygulanmasını daha da geliştirmek için süreç optimizasyonuna ve gelecekteki araştırma yollarına yönelik önerilerle sonlandırılmaktadır. Bu çalışma, ileri üretim tekniklerini malzeme bilimiyle entegre etmek için kapsamlı bir çerçeve sunarak endüstri gereksinimlerini karşılamaktadır.

ACKNOWLEDGEMENTS

Finishing this PhD thesis has been a journey full of learning and hard work. I am so thankful to everyone who helped and supported me along the way. First, I want to thank my advisors, Dr. Hatice Sinem Şaş Çaycı and Dr. Mehmet Yıldız, for their guidance, support, and advice. Their feedback and encouragement helped me improve my work and grow as a researcher. My sincere thanks go to the jury members, Dr. Burcu Saner Okan, Dr. Burç Mısırlıoğlu, Dr. Volkan Eskizeybek, and Dr. Bertan Beylergil, for their time and valuable feedback. Their comments made my thesis better and stronger.

I feel lucky to have great friends at Sabancı University who supported me. A big thank you to my friend and collaborator, Sasan, for all the discussions and teamwork. Your friendship made this journey easier and more enjoyable. I also want to thank Sina, Payam, Sajad, Peyman, Mahsa, and Vahid for being there for me. Your presence, insightful conversations, and encouragement added so much positivity and motivation to this journey. I am also grateful to Ehsan, whose phone calls from across the ocean, where we discussed different aspects of life, motivated and comforted me. I thank Amir, Hosein, Aslan, Arsalan, and Arman who, even from far away, have supported me with their friendship. During my time in Istanbul, I am thankful to Sahar, Salim, Aysan, and Farzin who made my time here much better.

To my family, I can't thank you enough. I wish my father, Jalil Barzegar, could have been here to see this moment. He gave me confidence and taught me to believe in myself. My mother, Akram Talebi, always encouraged me to continue my academic journey and gave me so much love and support. My sister, Nasim, and her husband, Faraz, have always been there for me and kept me going. Your love means everything to me.

I also want to thank everyone at SU-IMC. You created a supportive and collaborative environment that made work more enjoyable. Working with all of you was a great experience. Finally, I extend my gratitude to Sabancı University for funding my research and supporting my work.

This milestone would not have been possible without all of you. To everyone who has been part of this journey, your support means the world to me, and I will always be grateful.

Thank you.

To Baba and Maman...

TABLE OF CONTENTS

LIST OF TABLES	xiii
LIST OF FIGURES	xiv
LIST OF SYMBOLS	xvii
LIST OF ABBREVIATIONS	xix
CHAPTER 1: INTRODUCTION.....	1
1.1. Thermoset and Thermoplastic Composites.....	1
1.2. Manufacturing Methods for Composites	2
1.3. Automated Fiber Placement (AFP).....	3
1.4. Applications and Advancements in AFP	4
1.5. State of the Art	4
CHAPTER 2: EFFECT OF FIBER ORIENTATION ON TEMPERATURE HISTORY DURING LASER ASSISTED THERMOPLASTIC FIBER PLACEMENT.....	7
2.1. Introduction.....	7
2.2. Material and Methods	10
2.2.1. Specimen Manufacturing	10
2.2.2. Surface Temperature Measurement	11
2.2.3. Thermal Contact Resistance Measurement.....	12
2.2.4. Material Characterization of Composite Specimens.....	15
2.3 Thermal Model.....	16
2.3.1. Discretization of the FDM	19
2.4. Results and Discussion.....	21
2.4.1. Effect of Fiber Orientation on the Degree of Intimate Contact	22
2.4.2. The Validation of Thermal Model	24
2.4.3. Prediction of Thermal History	26
2.4.4. The Effect of Fiber Orientation on the Temperature of Process Nip Point .	27
2.4.5. The Effect of Fiber Orientation on Temperature History of Consolidation Region.....	29
2.4.6. The Effect of Fiber Orientation on Cooling Rate	31
2.5. Summary	33

CHAPTER 3: ENHANCING INTERLAMINAR BONDING QUALITY ESTIMATION IN LASER-ASSISTED FIBER PLACEMENT OF CF/PEKK COMPOSITES: A CORRECTION FACTOR APPROACH FOR IMPROVED PREDICTION OF INTIMATE CONTACT..... 35

3.1. Introduction..... 35

3.2. Materials and Experimental Methods 41

 3.2.1. Laser-Assisted Fiber Placement System and Sample Manufacturing 41

3.3. Contact Length and Pressure for the LAFP System 43

3.4. Experimental Degree of Intimate Contact Measurement..... 47

3.5. T-peel Test and Interlaminar Bonding Strength Characterization 47

3.6. Interlaminar Bonding Model..... 49

 3.6.1. Mantell and Springer Degree of Intimate Contact Model 49

3.7. Degree of Healing Model..... 51

3.8. Degree of Bonding Model..... 52

3.9. Results and Discussion..... 52

 3.9.1. Experimental Degree of Intimate Contact 52

 3.9.2. Temperature Profile 54

 3.9.3. Degree of Intimate Contact from Mantell and Springer (MS) and Introduction of Modified Mantell and Springer (MMS) Model 56

 3.9.4. Degree of Healing 59

 3.9.5. Degree of Bonding 61

3.10. Summary 64

CHAPTER 4: MULTI-SCALE PERMEABILITY CHARACTERIZATION OF COMPOSITES FABRICATED VIA LASER-ASSISTED FIBER PLACEMENT: A COMPARATIVE ANALYSIS OF PULSE-DECAY AND MICROCT TECHNIQUES..... 66

4.1. Introduction..... 66

4.2. Materials and Experimental Methods 70

 4.2.1. Air Permeability Assessment with Pulse-Decay Method 72

 4.2.2. X-ray Micro Computed Tomography 75

4.3. Results and Discussion..... 77

 4.3.1. Pulse-Decay Method Permeability Calculation 77

 4.3.2. Micro-CT Permeability Analysis 81

4.4. Summary	84
CHAPTER 5: GENERAL CONCLUSION AND FUTURE STUDIES	85
5.1. General Conclusion.....	85
5.2. Future Studies	87
REFERENCES.....	89

LIST OF TABLES

Table 1. Overview of the required input parameters for the heat transfer model.....	19
Table 2. The β_n coefficients in Equation (2.6) for grid points based on location in computational domain.....	21
Table 3. The degree of intimate contact and thermal contact resistance for different manufacturing conditions.	23
Table 4. The calculated cooling rate within the consolidation and cooling regions for different specimen manufacturing.	32
Table 5. Process parameters for LAFP placement trials of the samples.....	42
Table 6. Degree of intimate contact values from experiment, Mantell and Springer (MS) and Modified Mantell and Springer (MMS) with respect to normalized AFP process parameters.....	54
Table 7. Experimental data from Celik et al. [36] and simulation results validating the accuracy of the proposed CFLR formula.....	59
Table 8. Degree of bonding values obtained from the experiment (T-peel test), Mantell and Springer (MS), and Modified Mantell and Springer (MMS) methods, relative to normalized AFP process parameters.....	64
Table 9. LAFP placement trial parameters for the fabrication of the samples.	72
Table 10. Manufacturing and permeability characteristics of in situ consolidated LAFP samples.....	80
Table 11. Micro-CT analysis results for equivalent radius, porosity, and permeability over porosity for various stacking sequences at different lay-up velocities.	83

LIST OF FIGURES

Figure 1. Laser assisted fiber placement robot.	9
Figure 2. A typical LWIR image during the placement of the third layer with a UD orientation of the substrate for the layup speed of $v = 100$ mm/s.	12
Figure 3. A schematic for the thermal contact resistance between the plies of a UD composite laminate.	13
Figure 4. Representing surface roughness of an unprocessed tape as successive rectangular elements.	14
Figure 5. The variation of visible nip point temperature during the placement of the third layer for UD laminate with layup speed of $v = 100$ mm/s. Regions 1 and 3 represent acceleration and deceleration part and region 2 indicates nearly constant temperature distribution.	14
Figure 6. A schematic for the geometry of the thermal model along with the relevant boundary conditions.	18
Figure 7. The degree of intimate contact between second and third layers for (a) $[0^\circ/0^\circ]$, (b) $[45^\circ/0^\circ]$ and (c) $[90^\circ/0^\circ]$ interfaces at the deposition speed of $v = 100$ mm/s.	22
Figure 8. Degree of intimate contact between the first and second layers for (a) $[0^\circ/0^\circ]$, (b) $[45^\circ/0^\circ]$, and (c) $[90^\circ/0^\circ]$ interfaces at a layup speed of 100 mm/s.	22
Figure 9. The comparison of experimental and numerical thermal profile for (a) substrate and (b) tape during the placement of the third layer with the layup speed of 100 mm/s.	24
Figure 10. Numerically computed thermal profile with the calibrated absorptance parameter for (a) substrate and (b) tape surface during the placement of the third layer with the layup speed of 100 mm/s.	25
Figure 11. A representative numerical temperature history of the substrate-tape interface at different region of the layup for the UD configuration with the layup speed of 100 mm/s and full degree of intimate contact.	26
Figure 12. Temperature history prediction with thermal model for tape-substrate interface in different fiber orientation of substrate and layup speed of 100 mm/s.	27
Figure 13. Temperature history prediction with thermal model for tape-substrate interface in different fiber orientation of substrate and layup speed of 400 mm/s.	28
Figure 14. The percent improvement in the process nip point temperature, $\delta TPNP$ for different fiber orientations of the substrate at two layup speeds.	29

Figure 15. Prediction of temperature history for tape-substrate interface in different fiber orientations with two different layup speeds.	30
Figure 16. DSC heating and cooling curves of laminates with different fiber orientations at two layup speeds: (a) 100 mm/s (heating), (b) 400 mm/s (heating), (c) 100 mm/s (cooling), and (d) 400 mm/s (cooling).....	32
Figure 17. Contact length and static pressure measurement by utilizing pressure sensitive film with the LAFP device.....	44
Figure 18. Procedure for converting Fujifilm color density to pressure values in the contact area.	45
Figure 19. Change in grayscale and pressure with the color density of the LAFP device.	45
Figure 20. Nonlinear behavior of the roller applied consolidation force in relation to the contact length and consolidation pressure.	46
Figure 21. Microscopy images with grayscale representations, emphasizing the intimate contact region, facilitating the experimental degree of intimate contact measurement at the tape-substrate with (a) $[0^\circ/0^\circ]$ interface of Sample #2 and (b) $[90^\circ/0^\circ]$ interface of Sample #6.	47
Figure 22. T-peel test (a) experimental setup and (b) peeling force per unit width vs. extension for Sample #2 (autoclaved) and Sample #1.....	48
Figure 23. Illustration of the geometric features of the incoming tape and the idealized contact surface of the substrate.....	50
Figure 24. Comparison of experimental degree of intimate contact for laminates manufactured using different processes with degree of intimate contact obtained from Mantell and Springer (MS) and Modified Mantell and Springer (MMS) models.....	53
Figure 25. Flow chart illustrating the calculations of degree of intimate contact, degree of healing and degree of bonding using MS and MMS models.....	55
Figure 26. Temperature profiles during AFP lay-up for Sample #1 at $[0^\circ/0^\circ]$ interface with full ($Dic = 1$) and partial degree of intimate contact ($Dic, exp = 0.936$).....	55
Figure 27. Comparison of experimental degree of intimate contact reported by Celik et al. [36] with degree of intimate contact obtained from Mantell and Springer (MS) and Modified Mantell and Springer (MMS) models.	59
Figure 28. Degree of healing results for different process parameters and fiber orientations with intimate contact values derived from MS and MMS models.	60

Figure 29. Comparison of experimental degree of bonding for laminates manufactured using different processes with a degree of bonding obtained with the incorporation of Mantell and Springer (MS) and Modified Mantell and Springer (MMS) models.....	62
Figure 30. Representative SEM images of the typical fracture surfaces observed in T-peel test specimens for process parameters of 100 mm/s and 600 N (a) Sample #2 at [0°/0°] interface and (b) Sample #6 at [90°/0°] interface, and for process parameters of 400 mm/s and 300 N (c) Sample #3 at [0°/0°] interface, and (d) Sample #7 at [90°/0°] interface.	63
Figure 31. Workflow of the study showing the steps involved in composite manufacturing using LAFP and permeability analysis through pulse-decay and micro-CT methods. ..	71
Figure 32. Schematic (top) and experimental setup (bottom) of pulse-decay gas flow characterization.	73
Figure 33. Working principle of a micro computed tomography system.	76
Figure 34. Cross-section A-B with lowest porosity from 3D micro-CT reconstruction for permeability analysis	77
Figure 35. Pressure records from the pulse-decay method for different samples over time.	78
Figure 36. Numerical and experimental nondimensional pressure–time diagrams for in situ consolidated LAFP samples.....	80
Figure 37. Micro-CT scans of CF/PEKK laminates fabricated using LAFP with three stacking sequences ([0°/0°/0°], [0°/45°/0°], [0°/90°/0°]) and two layup velocities (100 mm/s and 400 mm/s).....	82
Figure 38. Comparison of permeability determined using the pulse-decay method (PDM) and micro-CT (μ CT) for [0°/45°/0°] and [0°/90°/0°] laminates at flow velocities of 100 mm/s and 400 mm/s.....	83

LIST OF SYMBOLS

a	Absorptance
a_0	Depth of surface asperities in unprocessed tape
b	Klinkenberg parameter
b_0	Width of surface asperities in unprocessed tape
CF_{exp}	Experimental correction factor
CF_{LR}	Linear regression correction factor
c_p	Specific heat
D_b	Degree of bonding
$D_{b,exp}$	Experimentally measured degree of bonding
D_h	Degree of healing
D_{ic}	Degree of intimate contact
$D_{ic,exp}$	Experimentally measured degree of intimate contact
$D_{ic,MS}$	Degree of intimate contact by Mantell and Springer (MS) model
D_{ic,t_0}	Degree of intimate contact in unprocessed tape
F	Compaction force
\hat{F}	Normalized force
h	Laser spot height
h_a	Ambient heat transfer coefficient
h_r	Roller heat transfer coefficient
h_s	Laser spot height on substrate
h'_s	Laser-illuminated length on the substrate
h_t	Laser spot height on tape
h'_t	Laser-illuminated length on tape
K	Permeability
k_{air}	Air thermal conductivity

K_g	Gas permeability
K_i	Intrinsic liquid permeability
k_y	Laminate through-thickness thermal conductivity
L	Maximum mesh size in Finite Difference Method (FDM)
l	Domain length
l_c	Roller contact length
P_{app}	Applied consolidation pressure
Pe	Peclet number
$(PF)_{LAFP_{avg}}$	Average peel force per unit width of the LAFP process only
$(PF)_{AC_{avg}}$	Average peel force per unit width with autoclave post-processing
P_f	Final vacuum pressure
P_i	Atmospheric pressure
\hat{P}	Nondimensionalized pressure
\hat{P}_s	Shape parameter of the pressure decay function
q	Heat flux
q_n	Normal component of the heat flux vector
q_s	Heat flux on substrate
q_t	Heat flux on tape
\dot{q}	Heat source per unit volume
R_c	Thermal contact resistance
R_{eq}	Average pore radius
T	Temperature
T_a	Air temperature
T_b	Boundary temperature
T_g	Glass transition temperature
T_i	Ambient temperature
T_{PNP}	Process nip point temperature
T_r	Roller temperature
T_s	Substrate temperature
T_t	Tape temperature
T_{tl}	Tool temperature
t_c	Characteristic time

t_s	Substrate thickness
t_t	Tape thickness
t_w	Welding time
\hat{t}	Nondimensionalized time
v	Velocity
\hat{v}	Normalized velocity
w_0	Gap between surface asperities in unprocessed tape
w_s	Laser-illuminated width on substrate
w_t	Laser-illuminated width on tape
X_c	Degree of crystallinity
\hat{x}	Nondimensionalized length
α	Thermal diffusivity
β_n	Coefficients in the Finite Difference Method (FDM) equation
γ	Ratio of Δy to Δx
ΔH_m	Melting enthalpy obtained from the melting peak area
ΔH_m°	Melting enthalpy corresponding to PEKK material with 100% crystallinity
Δx	Mesh size in the layup direction
Δy	Mesh size in the laminate thickness direction
$\mu(T)$	Temperature-dependent viscosity of the thermoplastic resin
\emptyset	Effective porosity
ρ	Density
θ	Laser incident angle
$\hat{\theta}$	Normalized fiber orientation

LIST OF ABBREVIATIONS

Abs	Absolute
AFP	Automated fiber placement
BAC	Bearing area curve
CF	Carbon fiber
FIC	Full degree of intimate contact
ILSS	Interlaminar shear strength
LAFP	Laser-assisted fiber placement
LWIR	Long-wave infrared
MMS	Modified Mantell and Springer
MS	Mantell and Springer
OaA	Out of Autoclave
PEEK	Polyether Ether Ketone
PEI	Polyetherimide
PEKK	Polyether Ketone Ketone
PDM	Pulse-decay method
PPS	Polyphenylene Sulfide
PIC	Partial degree of intimate contact
PDE	Partial differential equation
RRSQ	Residual sum of squares
SBS	Short beam strength
SEM	Scanning electron microscopy
UD	Unidirectional
XCT	X-ray computed tomography
μ CT	Micro-CT

CHAPTER 1: INTRODUCTION

Composite materials have become an integral part of modern engineering and manufacturing due to their superior mechanical properties and lightweight nature. These materials are composed of two or more constituent phases, typically a reinforcement (e.g., fibers) embedded within a matrix (e.g., polymers, ceramics, or metals). The synergy between these constituents enables composites to exhibit a unique combination of strength, stiffness, and durability, which surpasses those of their individual components [1]. Applications of composites span diverse industries such as aerospace, automotive, wind energy, and sports equipment, highlighting their versatility and significance in advancing technological capabilities [2].

The development and application of composite materials have been driven by the increasing demand for materials that can provide high performance while reducing weight and fuel consumption. In aerospace, for example, the use of advanced composites in aircraft structures has resulted in lighter airframes and enhanced fuel efficiency. Similarly, the automotive sector has embraced composites to achieve weight reductions, contributing to lower emissions and improved performance. The wind energy industry relies on composites for manufacturing large and durable turbine blades capable of withstanding harsh environmental conditions [3].

1.1. Thermoset and Thermoplastic Composites

The matrix material in composites plays a pivotal role in determining their overall performance, and polymer-based matrices are among the most commonly used. These matrices can be broadly classified into thermosets and thermoplastics based on their chemical and physical behavior.

Thermoset polymers, such as epoxy, polyester, and vinyl ester, cure irreversibly through a chemical crosslinking process. This process creates a rigid, three-dimensional molecular network, offering high thermal and chemical resistance as well as dimensional stability. Thermosets are widely used in structural applications due to their high mechanical properties and resistance to environmental degradation. However, thermosets are not reprocessible or recyclable, which poses challenges in terms of sustainability. Their use also involves complex and time-intensive curing cycles, which may limit manufacturing efficiency [3].

Thermoplastics, including polyetheretherketone (PEEK), polyetherketoneketone (PEKK), and polypropylene (PP), differ significantly from thermosets in their ability to be reheated and reshaped. These materials exhibit excellent toughness, impact resistance, and recyclability, making them increasingly popular in applications demanding high performance and environmental considerations. Thermoplastic composites are characterized by their short cycle times, suitability for automated manufacturing processes, and compatibility with modern design-for-recycling strategies [4]. Among thermoplastics, CF/PEKK composites, which combine carbon fiber reinforcement with a PEKK matrix, have garnered significant attention due to their exceptional strength-to-weight ratio, high-temperature performance, and resistance to harsh chemical environments [5].

CF/PEKK composites are particularly suited for aerospace applications, where stringent requirements for mechanical strength, thermal stability, and durability must be met. Their ability to endure high operational temperatures and maintain structural integrity under demanding conditions has made them a preferred choice for critical components such as engine parts, primary structures, and fasteners. Additionally, CF/PEKK composites offer advantages in terms of fatigue resistance and chemical compatibility, further extending their application potential [6].

1.2. Manufacturing Methods for Composites

Composite manufacturing encompasses a variety of techniques tailored to specific material properties, component geometries, and application requirements. Traditional

methods such as hand lay-up, resin transfer molding (RTM), and filament winding are widely used but may have limitations in automation and scalability. While these methods are suitable for small-scale or customized production, they often involve labor-intensive processes that are not conducive to high-throughput manufacturing [7].

In contrast, advanced manufacturing methods, particularly Automated Fiber Placement (AFP), have revolutionized the production of high-performance composite structures. AFP is a highly automated process that involves the precise placement of fiber tows onto a mold or mandrel using a robotic head. This technology allows for the creation of complex geometries with minimal waste and reduced production time compared to manual methods. AFP is especially advantageous in applications requiring large, intricate, and structurally demanding components, such as aircraft fuselages and wind turbine blades [8].

1.3. Automated Fiber Placement (AFP)

AFP technology represents the pinnacle of composite manufacturing innovation. The process integrates robotics, advanced control systems, and real-time monitoring to achieve unparalleled precision and efficiency. Fiber tows, typically pre-impregnated with resin (prepreg), are laid down layer by layer in specific orientations to meet the desired mechanical properties and design specifications. The ability to tailor fiber placement results in optimized weight and performance characteristics [9].

A key advantage of AFP lies in its compatibility with both thermoset and thermoplastic composites. For thermoplastics like CF/PEKK, AFP enables in-situ consolidation, where the matrix material is melted and bonded during the placement process, eliminating the need for separate curing steps. This not only enhances production efficiency but also reduces energy consumption and environmental impact [10].

The in-situ consolidation capability of AFP has been particularly transformative for thermoplastic composites, offering a continuous manufacturing process that integrates material deposition and consolidation. This approach eliminates the need for autoclaves or other post-processing equipment, enabling cost savings and increased production rates. However, achieving consistent quality during in-situ consolidation requires precise

control over parameters such as temperature, pressure, and placement speed. Research in this area has focused on optimizing these parameters to improve bond strength, reduce void content, and ensure uniform material properties across the laminate [11].

Challenges associated with AFP include high initial costs, equipment complexity, and sensitivity to process parameters. The integration of sensors and data analytics into AFP systems has emerged as a promising solution to address these challenges, enabling real-time monitoring and adaptive control of the process. Advanced simulation tools have also been developed to predict the behavior of fiber tows during placement, helping manufacturers optimize layup strategies and minimize defects [12].

1.4. Applications and Advancements in AFP

AFP has found widespread adoption in aerospace and other high-performance industries, where its ability to produce large and lightweight structures with exceptional precision is highly valued. Notable examples include the manufacture of aircraft wings, fuselage sections, and empennages, as well as components for space exploration vehicles and satellites. The automotive industry has also begun exploring AFP for producing lightweight structural components, driven by the need for fuel efficiency and emission reduction [13].

In the context of CF/PEKK composites, AFP provides an optimal manufacturing approach due to its ability to leverage the material's high performance while addressing the complexities associated with thermoplastic processing [14].

1.5. State of the Art

This thesis aims to provide a comprehensive understanding of the manufacturing process of thermoplastic composites, particularly CF/PEKK, utilizing Automated Fiber Placement (AFP) technology. By delving into the effects of fiber orientation, processing parameters, and material behaviors, this research addresses the challenges and opportunities in achieving high-quality in-situ consolidated composite laminates. The

innovative approach combines experimental investigations, process modeling, and optimization strategies to enhance the applicability and efficiency of AFP in advanced composite manufacturing.

The state-of-the-art review reveals that thermoplastic composites, such as CF/PEKK, offer significant advantages over thermoset composites, including higher toughness, rapid processing, and recyclability. AFP technology, particularly with laser-assisted systems, has emerged as a key enabler for efficient manufacturing of these materials. However, challenges such as achieving optimal temperature distribution, interlaminar bonding, and material permeability persist, necessitating further research. This thesis aims to bridge these gaps through a systematic investigation of critical factors influencing the AFP process.

This thesis is organized into five comprehensive chapters, each dedicated to exploring critical aspects of the research:

In Chapter 1, the introduction presents an extensive review of composite materials, the distinction between thermosets and thermoplastic composites, manufacturing techniques, and the significance of AFP technology. It establishes the research context, outlines the state of the art in thermoplastic composite manufacturing, and lays the foundation for understanding the motivations and objectives of this study.

In Chapter 2, the influence of fiber orientation on temperature distribution during the AFP process is investigated. Using both experimental and numerical methods, the study evaluates how different stacking sequences affect the degree of intimate contact, thermal contact resistance, and the overall thermal history. These insights are critical for optimizing thermal management during the AFP process and achieving high-quality laminates.

In Chapter 3, interlaminar bonding, a key determinant of composite performance, is explored. This chapter introduces a correction factor approach to improve the prediction and measurement of intimate contact. The research includes detailed experimental methodologies, interlaminar bonding strength assessments, and theoretical modeling. By addressing bonding challenges, this chapter contributes to enhancing the structural integrity and performance of CF/PEKK composites.

In Chapter 4, the permeability of composite laminates, a vital property for their mechanical performance and durability, is examined. By comparing pulse-decay and micro-CT techniques, the research investigates how fiber orientation, layup speed, and consolidation conditions influence the permeability of CF/PEKK laminates. The chapter underscores the importance of multi-scale analysis in understanding and optimizing material behavior, directly supporting the goal of improving AFP processes.

In Chapter 5, the concluding chapter synthesizes the findings from the preceding chapters, providing a cohesive overview of the research contributions. It also outlines potential future studies, including advancements in AFP technology, further exploration of innovative AFP applications and techniques, and broader industrial applications. By summarizing the key outcomes, this chapter ties the research back to its overarching objective of advancing AFP technology for thermoplastic composites.

By systematically addressing these aspects, this thesis contributes to advancing the state of the art in thermoplastic composite manufacturing and underscores the transformative potential of AFP technology in high-performance industries. The findings presented here not only enhance the understanding of CF/PEKK processing but also provide actionable insights for improving AFP-based manufacturing, paving the way for future innovations in composite materials and structures.

CHAPTER 2: EFFECT OF FIBER ORIENTATION ON TEMPERATURE HISTORY DURING LASER ASSISTED THERMOPLASTIC FIBER PLACEMENT

In this chapter, the effect of fiber orientation on the temperature history during the layup process is comprehensively investigated experimentally and numerically. Specimens with three different fiber orientations (i.e., $[0^\circ/0^\circ/0^\circ]$, $[0^\circ/45^\circ/0^\circ]$, and $[0^\circ/90^\circ/0^\circ]$) are manufactured at two layup speeds and characterized for determining the degree of intimate contact and then calculating the thermal contact resistance. Then, an improved thermal model with thermal contact resistance is developed and validated to predict the temperature history accurately. The experimental results indicate that the degree of intimate contact decreases by increasing the difference in fiber orientation between the interfaces of successive plies, revealing a relationship between substrate fiber orientations and cooling rates. The effect of cooling rate on the degree of crystallinity is studied for all stacking configurations at two layup speeds and found that as the angle between the subsequent plies decreases, the cooling increases, leading to a drop in the degree of crystallinity. The outcomes of this study address the need for an improved thermal model approach for accurately predicting the thermal history of the manufactured composite by the LAFP process.

2.1. Introduction

Automated technologies like automated fiber placement (AFP) have started emerging to overcome the shortcomings of traditional composite manufacturing techniques such as hand layup methods, which operate with a slow production rate and deliver non-repeatable high-quality parts [14] AFP techniques have different heating sources, such as laser, infrared, heat lamp, or hot gas torch [9]. The laser-assisted fiber placement (LAFP)

process has been a viable manufacturing technique for manufacturing fiber reinforced thermoplastic composite components. In a typical LAFP process, an end effector or fiber placement head places several juxtaposed slit tapes or tow-prepreg on a tool, which are then simultaneously in-situ consolidated through the concurrent usage of a consolidation roller and laser heat source, both of which are installed on the end effector. An essential advantage of LAFP can be eliminating the need for time-consuming and expensive post-consolidation with the autoclave process [15]. Moreover, the AFP process provides immense flexibility for the design space since fibers can be steered in any orientation [16].

In the AFP process shown in Figure 1, the quality of the manufactured part is significantly affected by the thermal history [17], [18]. Temperature distribution influences all temperature-related processes such as intimate contact development [19], [20], [21], inter-laminar bond strength [22], [23], void dynamics [24], [25], thermal degradation [26], residual stress [27], [28] and the crystallinity level of the composite laminate [29], [30]. In literature, one may find various one- [24], [31], [32], two- [17], [33], [34], [35] or three-dimensional [36], [37] thermal models which study the effect of AFP process parameters such as layup speed, laser heat source properties (power and incident angle), and consolidation force on the thermal history of unidirectional (UD) layup. Nevertheless, none of these investigations has considered the effect of different fiber orientations on the thermal history of the layup in the AFP process with the intimate contact perspective. In literature, it was proposed that the change in the fiber orientation with respect to the laser heat source might affect the absorbed and scattered level of laser radiation by fibers, respectively, due to (i) the alteration of the local amount of fibers exposed to the laser heat source since the laser beam is mainly absorbed by carbon fibers [38], [39] and (ii) the anisotropic scattering behavior of composite laminate such that the modified fiber orientation changes the reflection amount of laser beam from the substrate to the tape surface [39]. Stokes-Griffin and Compston [38] studied the effect of substrate fiber orientation on the temperature history from an optical perspective with a 3D ray-tracing model. However, their numerical results showed that the temperature history of the tape-substrate interface was not influenced much by different ply orientations. This can be attributed to the omission of intimate contact at the interface for different fiber orientations in their thermal model. Furthermore, it was experimentally shown in various studies that fiber orientation could affect fiber nesting [40] and the formation of resin-rich

areas (due to the anisotropic permeability behavior of composites [41], [42]), which are two critical factors in the development the intimate contact at subsequent ply interfaces. Levy et al. [31] studied the relationship between the degree of intimate contact and the resulting thermal contact resistance (R_c) between thermoplastic composite layers. Their experimental results showed that R_c values obtained for poorly consolidated samples were high and, thereby, caused a significant drop in the through-thickness thermal conductivity. They also developed a correlation in which R_c is related to the degree of intimate contact of the raw and processed tape. Recently, Celik et al. [36] have experimentally and numerically examined the effect of R_c between thermoplastic UD composite layers on the temperature history of newly placed tape. Their results indicated that the R_c could have a significant effect on the temperature history such that the difference between temperatures on the top surface of newly placed tapes after the consolidation region can be as high as 30°C for partial and full degree of intimate contact cases.

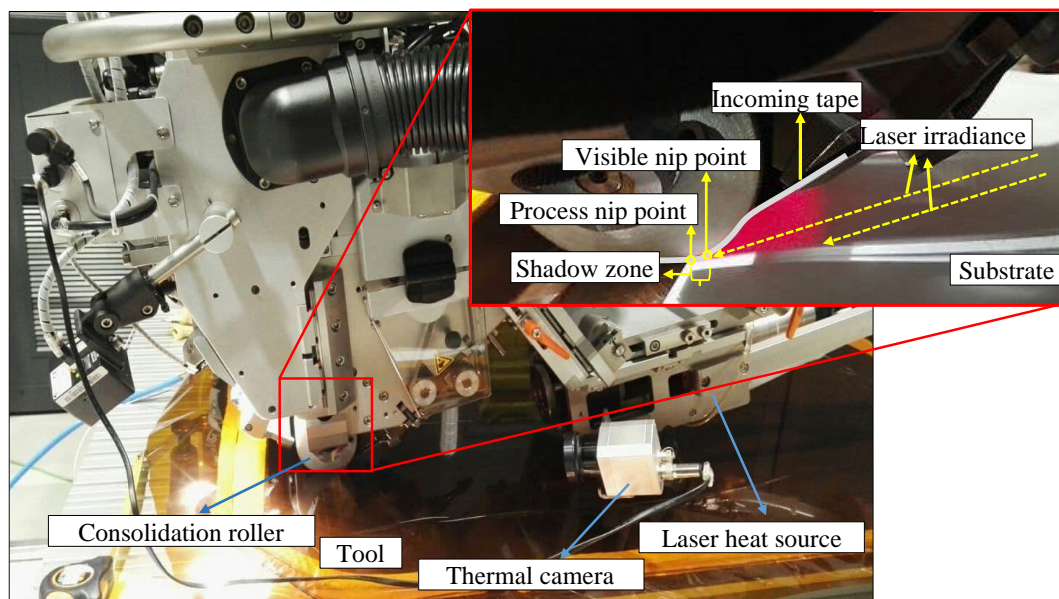


Figure 1. Laser assisted fiber placement robot.

As can be understood from the concise literature review provided above, the effect of fiber orientation on the temperature history has only been studied from the optical perspective and yet has not been investigated from the intimate contact point of view while considering the coupling between R_c and intimate contact. It is evident that R_c should be included in the thermal modeling of composite laminate manufacturing processes with AFP to accurately predict the thermal history of the manufactured composite with the LAFP process. To this end, there is a need for an experimentally

validated, comprehensive, and robust thermal model which considers these effects on the overall thermal history in the LAFP process. To achieve this goal, composite laminates with different fiber orientations are manufactured at two different layup speeds by employing the LAFP method. To determine the degree of intimate contact and R_c , optical microscopic images are taken from a cross-sectional area bounded by the thickness and the width of the manufactured laminates and then processed with image processing approaches. Furthermore, a 2D steady-state thermal model is developed along with the inclusion of R_c to predict the temperature history at the interface between the substrate and newly placed tapes for different fiber orientations. Based on simulation results, it is shown that there is a strong relationship between substrate fiber orientation and temperature history, particularly at a high layup speed. Finally, the effect of thermal history during the fiber placement process on the properties of manufactured composite is investigated by correlating the cooling rate with the degree of crystallinity.

2.2. Material and Methods

2.2.1. Specimen Manufacturing

A robotic-based automated fiber placement (AFP) method is employed to manufacture composite laminates, as depicted in Figure 1. The AFP system in question has an end-effector or fiber placement head with the capability of laying up eight juxtaposed 6.35 mm wide slit tapes simultaneously and continuously at a nominal maximum speed of 800 mm/s, a 6 kW laser heat source (Laserline LDF series diode laser unit) for in-situ compaction and consolidation between the layers, and optic lens with a 250 mm focal distance which can create a rectangular laser spot with an illuminated area of 8 mm \times 56 mm, and a conformable consolidation roller with the hardness of 60 shore and the diameter of 70 mm. For consolidation, the temperature of the layup tool is set to be 155°C. The thermoplastic slit tape used in this study is purchased from Toray Cetex Company with the manufacturing code of TC1320 CF/PEKK and has a fiber volume fraction of 66%, a nominal thickness, and width 0.15 mm and 6.35 mm, respectively.

The AFP manufactured thermoplastic laminates have the length and width of 1100 mm and 50.8 mm, respectively, and consist of three layers with the following stacking

sequences $[0^\circ/0^\circ/0^\circ]$, $[0^\circ/45^\circ/0^\circ]$, and $[0^\circ/90^\circ/0^\circ]$. Each laminate with these stacking sequences is produced at two layup speeds, namely, $v = 100$ mm/s and 400 mm/s. During placement of the second layer, the consolidation force is adjusted to a higher value of 1000 N to ensure the creation of full intimate contact, thereby eliminating or minimizing the R_c between the first and the second layers for all manufactured laminates. Throughout the remaining part of the current study, the first and the second layers together will be referred to as the substrate. Here, it should be remarked that the focus of this study is to scrutinize the temperature history during the layup of the third layer on the substrate with different fiber orientations. The consolidation force is set to 500 N to place the third layer on the substrate, having different fiber orientations for each stacking sequence. During the manufacturing of laminates, the laser power for two different layup speeds is adjusted to achieve a similar visible nip point temperature, specifically, the laser powers of 1386 W and 3427 W are used for 100 mm/s and 400 mm/s layup speeds, respectively.

2.2.2. Surface Temperature Measurement

To measure the surface temperature of the substrate and tape as a function of distance from the visible nip point during the manufacturing process without interfering with the surface intimate contact, a non-contact temperature measurement method is employed using a long-wave infrared (LWIR) camera (the Optris PI 400i). The thermal camera has 80 frames per second recording capability, an IR detector with a resolution of 382×288 pixels and is calibrated in the temperature range of -20 °C and 900 °C with the accuracy of ± 2 °C or ± 2 %. In the consolidation region, the temperature cannot be recorded by the thermal camera. To this end, a thermal model developed and presented in Section 2.3 is instead employed to predict the temperature under the consolidation roller and is validated concerning the thermal camera measurements. The validated thermal model for the substrate and tape is performed as follows. For the substrate, several thermal image frames are chosen from the recorded video during the third layer's layup, which corresponds to steady-state process conditions. From one of the images, the geometrical location of the visible nip point is identified based on the contact line between the substrate and tape. For each captured frame, seven 50 mm long measurement lines are defined on the heated area of the substrate in the vicinity of the visible nip point along the placement direction and run parallel to the roller axis. The first line is at 2.5 mm from the

visible nip point, and lines are placed at an equidistance of about 3 mm with respect to each other. Figure 2 shows a representative thermal image on which an indicative measurement line (the black one) is illustrated. The average temperature distribution on each line is obtained for all frames where there are roughly 25 temperature points on each line, and then line based average values are used to compute frame-based average temperature values, which are then assigned to corresponding point temperatures at the locus of the line with respect to the visible nip point. Essentially, seven average point temperatures along the placement direction are attained. As for the temperature field for the tape surface, a similar procedure is implemented. Five parallel temperature measurement lines are drawn as a function of the distance from the visible nip point. In this case, the distance of the line from the visible nip point is defined as the arc length. The first line is at a 2.5 mm arc length distance from the visible nip point, and the distance between each line is equal to the arc length of about 2 mm. The identical line and frame-based temperature averaging methodology are utilized, and the obtained average temperature values are recorded as point temperatures.

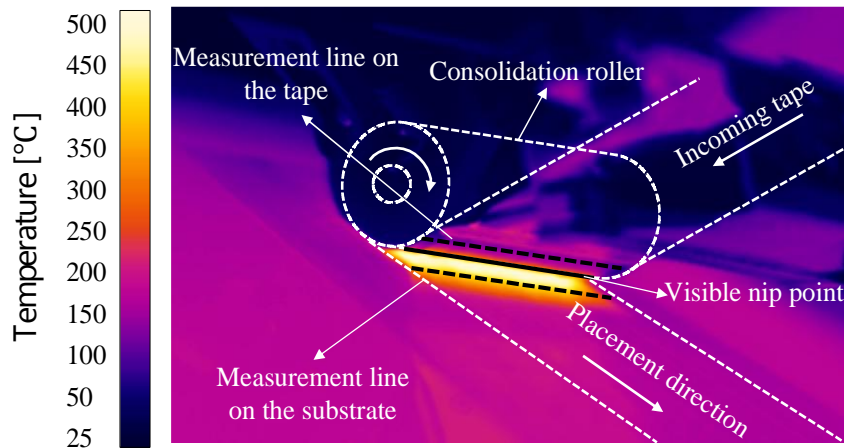


Figure 2. A typical LWIR image during the placement of the third layer with a UD orientation of the substrate for the layup speed of $v = 100$ mm/s.

2.2.3. Thermal Contact Resistance Measurement

If there is any inter-laminar void between tapes, as illustrated in Figure 3, there will be a rather poor heat transfer through the thickness direction of the laminate due low thermal conductivity value of air. Consequently, the heat flux (q) from the bottom surface of the newly placed tape to the top surface of the substrate is dependent on the thermal contact resistance, R_c , which can be formulated as

$$q = (T_t - T_s)/R_c \quad (2.1)$$

where T_t and T_s are the temperature of tape and substrate at the interface, respectively, that R_c can be computed by using the relation given in Equation (2.2) [31].

$$R_c = D_{ic,t_0} a_0 \left(\frac{1}{k_y D_{ic}^2} + \frac{1 - D_{ic}}{k_{air} D_{ic}} + \frac{1}{k_y} \right) \quad (2.2)$$

where D_{ic,t_0} is the initial degree of intimate contact, a_0 is the depth of the asperities of the raw tape and D_{ic} is after layup interface intimate contact, which is named the final degree of intimate contact. Additionally, k_y and k_{air} the thermal conductivities of the CF/PEKK composite in the through-thickness direction and air are equal to 0.73 W/mK and 0.0043 W/mK, respectively [41], [43].

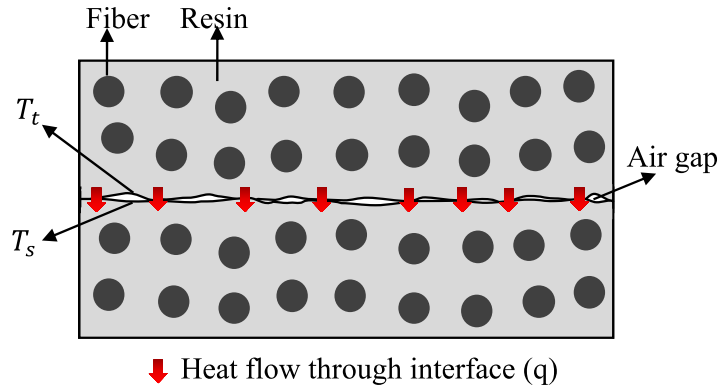


Figure 3. A schematic for the thermal contact resistance between the plies of a UD composite laminate.

To obtain D_{ic,t_0} and a_0 , the surface profile of the raw tape is measured in 800 μm by 800 μm square domain in a perpendicular direction to fibers by using the μsurf laser profilometer from nanofocus[®] as illustrated in Figure 4(a). Then the depth information of the surface topology along the red dashed line is extracted from the surface profile data and plotted in Figure 4(b), as a function of the distance on the line, from which the standard deviation of depth information is also computed. To calculate D_{ic,t_0} from the surface profile data, the model proposed by Lee and Springer [44] is employed. In this model, the irregularities of the initial tape surfaces are represented as a series of identical rectangular features with the geometrical parameters of a_0 , b_0 , and w_0 as depicted in Figure 4(c). The numerical values of these parameters are obtained by following the procedure proposed by Schaefer et al. [45]. Here, a_0 and b_0 are the height and the width of the rectangular element for unprocessed tape, respectively, and w_0 is the initial width

of the gap between two adjacent rectangular elements. It should be stated that a_0 is equal to twice the standard deviation of the surface profile, which is calculated to be $4.02 \mu\text{m}$. Accordingly, the degree of intimate contact for the unprocessed tape can be expressed in terms of b_0 and w_0 as $D_{ic,t_0} = b_0/(b_0 + w_0)$, whereby its numerical value is calculated as 0.392.

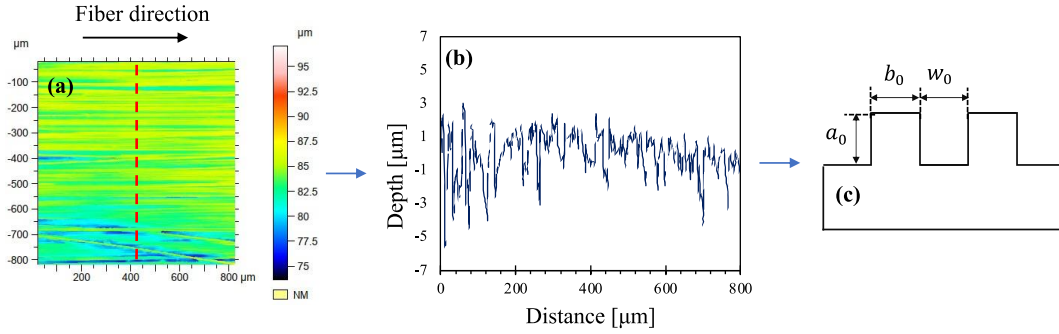


Figure 4. Representing surface roughness of an unprocessed tape as successive rectangular elements.

During the LAFFP process, the fiber placement head experiences an acceleration and deceleration at the initial and final fiber placement stages, denoted as regions 1 and 3 in Figure 5, respectively. These circumstances can affect the microstructure of composite laminate due to the lack of steady-state processing conditions at these stages.

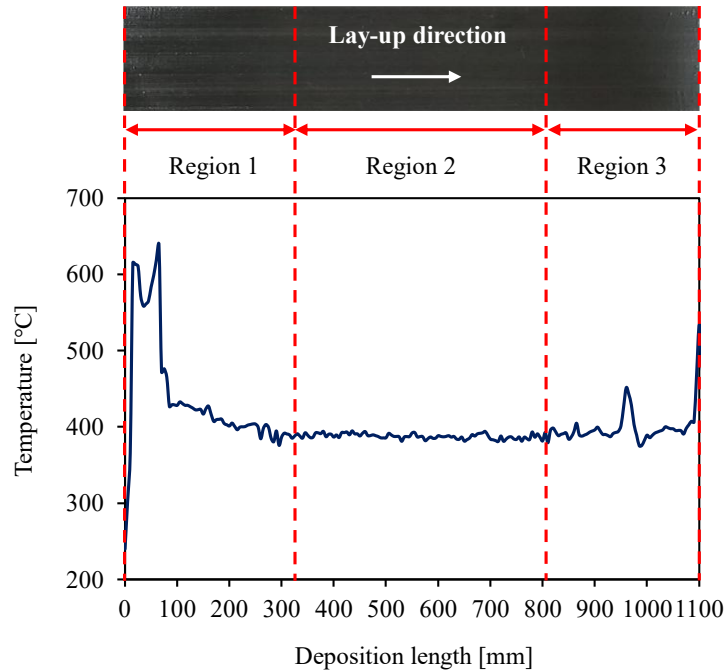


Figure 5. The variation of visible nip point temperature during the placement of the third layer for UD laminate with layup speed of $v = 100 \text{ mm/s}$. Regions 1 and 3 represent acceleration and deceleration part and region 2 indicates nearly constant temperature distribution.

Figure 5 also shows the thermal camera recording, which reveals the temperature variations in the vicinity of the visible nip point during the layup of the third layer with the layup speed of 100 mm/s for UD laminate. As can be seen, a nearly constant temperature profile can be attained within region 2, which corresponds to an almost constant layup speed.

Accordingly, for each manufactured laminate, four microscopic tests specimens are extracted from this region to calculate the final degree of intimate contact. The specimens are microscopically examined using a Nikon ECLIPSE LV100ND microscope with a 50x-magnification lens. For each specimen, several images are taken from the surface bounded by the width and thickness of the laminate and are then stitched together with an image processing software of ImageJ for thresholding analysis to determine the average value of the final D_{ic} for each laminate.

2.2.4. Material Characterization of Composite Specimens

Differential scanning calorimetry (Mettler Toledo DSC+3) analyses are performed to study the effects of cooling rate on the degree of crystallinity of the CF/PEKK laminates with different fiber angles and the layup speeds. The samples (~5 mg) are sealed in pinholes aluminum pans, heated up in the temperature range of 25–400 °C with a 10.0 °C/min heating rate, and then cooled with a rate of 10.0 °C/min under a nitrogen atmosphere with a 50 ml/min airflow rate. The degree of crystallinity (X_c) is calculated using Equation (2.3) [46].

$$X_c = \frac{\Delta H_m}{\Delta H_m^\circ \times (1 - x)} \times 100[\%] \quad (2.3)$$

where ΔH_m is the melting enthalpy obtained from the melting peak area, ΔH_m° is the melting enthalpy corresponding to PEKK material with 100% crystallinity (130 J/g) [47] and x is the fiber weight fraction of a laminate measured according to the ASTM D3171/Method B by the matrix digestion with acid treatment.

2.3. Thermal Model

Assuming a uniform temperature distribution along the width direction of the tape and substrate, a steady state and two-dimensional thermal model is developed to predict the temperature field in the substrate and tape interface. To consider the motion of the heat source attached to the moving robotic head, the Eulerian framework is utilized such that the roller and heat source are considered fixed, and instead, the deposited material moves in the opposite direction of the robotic fiber placement head at a constant velocity (v). The conservation of energy considered herein can be written accordingly as,

$$\rho c_p \left(v \frac{\partial T}{\partial x} \right) = \ddot{q} + k_x \left(\frac{\partial^2 T}{\partial x^2} \right) + k_y \left(\frac{\partial^2 T}{\partial y^2} \right) \quad (2.4)$$

where $T(x,y)$ is the temperature expressed as a function of x and y coordinate axes, corresponding to the material layup and through the thickness directions, ρ is the density, c_p is the specific heat capacity, \ddot{q} is the heat source per unit volume, k_x and k_y are the thermal conductivities of the lamina in respective directions. The convective heat transfer term on the left-hand side of Equation (2.4) is present to account for the effect of moving heat sources in the model. The heat generation due to crystallization enthalpy is neglected since it is much smaller than the laser heat source [32].

The geometry and boundary conditions of the modeling domain are schematically provided in Figure 6. Three main types of thermal boundary conditions are applied to the modeling domain, namely, (i) $T = T_b$ with T_b being the temperature of the boundary, (ii) $q_n = -k_n \partial T / \partial n$ where q_n is the normal component of the heat flux vector, $\partial / \partial n$ is a partial derivative operator along the normal direction, n , and k_n is the thermal conductivity along the direction of the normal heat flux, and (iii) $q_n = h_i (T - T_i)$. Here, h_i is the convection heat transfer coefficient between the heat transfer surface and external medium, T_i is the temperature of the external (ambient) medium, and subscript $i = r, a$ corresponds to mediums as roller and air, respectively.

To clearly address the physics of the LAFP process and introduce the implementation of relevant boundary conditions, the process domain is divided into four regions, namely, heating, shadow, consolidation, and cooling. Moreover, to simplify the problem, the effect of the tool and roller on the temperature field is incorporated into the numerical

model as boundary conditions. For the tool, the Dirichlet boundary condition is imposed on the bottom surface of the substrate (B_{15} , $T = T_{tl} = 155 \text{ }^\circ\text{C}$). The boundary condition between the roller and tape (B_2 , including heating, shadow, and consolidation regions), denoted with orange arrows in Figure 6, is defined as a convective boundary condition such that $q_y = h_r(T - T_r)$. For model simplification without altering the physics of the problem, at the heating region, the tape feed is considered horizontally, and a very large thermal contact resistance ($R_c = 10^{20} \text{ m}^2\text{K/W}$) is defined between the substrate and the tape to ensure that they are not in physical contact with each other. Moreover, Dirichlet boundary condition is applied on the left vertical boundary of the substrate (B_9) and the incoming tape (B_1) as $T = T_t$ and $T = T_a$, respectively. The bottom surface of the tape (B_8) and the top surface of the substrate (B_{10}) are subjected to constant heat flux boundary condition for the illuminated lengths of h'_s and h'_t , respectively since they receive laser power until the beginning of shadow region. The relation between the laser power, P and heat flux [48],

$$q_s = \left(P \frac{h_s}{h} \right) \frac{1}{h'_s w_s} a, q_t = \left(P \frac{h_t}{h} \right) \frac{1}{h'_t w_t} a \quad (2.5)$$

where q_s and q_t are the heat fluxes, h_s/h and h_t/h are the fractions of laser irradiances, h'_s and h'_t are the illuminated lengths, and w_s and w_t are the illuminated widths on the surfaces of the substrate and tape, respectively, and a is the absorptance. The geometrical parameters, h'_s, h'_t, w_s, w_t and laser incident angle, θ are obtained by on-site measurements and related parameters, h_s, h_t and h are calculated using simple geometrical relations. Moreover, both the top surface of the substrate and the bottom surface of the incoming tape are also subjected to convective boundary condition between the inception of illuminated region (heating) and the end of shadow region, depicted by blue arrows in Figure 6. In the shadow region (B_7 and B_{11}), temperature field will experience sudden drop because the laser irradiance cannot reach to surfaces of the tape and the substrate. In the consolidation region (B_6 and B_{12}), as the name implies, new incoming tape is bonded to the previously placed plies (substrate) due to the applied roller pressure. This region starts with a process nip point wherein the bottom surface of the tape and top surface of substrate begin to contact each other thereby forming the tape-substrate interface. This interface continues until the end of cooling region. Recalling from Section 2.2.3, the heat flux across the interface (red arrows in Figure 6) is dependent on thermal contact resistance. It should be remembered that thermal contact resistance is

only defined for the interface between the second and the third plies (top interface). In the cooling region the laminate is exposed to air temperature and cools down until its temperature becomes equal to tool temperature. Hence, there is a convective heat transfer between the tape top surface and air (B_3).

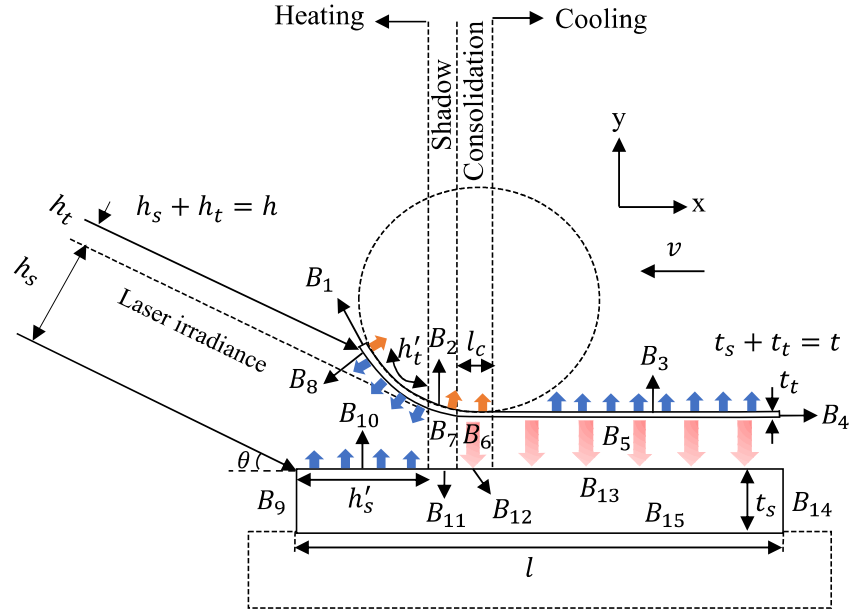


Figure 6. A schematic for the geometry of the thermal model along with the relevant boundary conditions.

It should be remarked that in composite materials, the laser beam power is mainly absorbed by fibers. Hence, absorptance should be a function of fiber orientation and fiber volume fraction [38], [39]. In all stacking sequences, the incoming tape has always unidirectional (UD) orientation, but the ply orientation for the top surface of the substrate changes with respect to the laser heat source. Therefore, it is necessary to update the absorptance for cross-ply orientation. This is realized by continuously comparing numerically computed and experimentally measured temperature fields at several predefined locations while iteratively changing absorptance until the difference between the temperature values of the model and experiment are minimized. The absorptance parameter of CF/PEEK tape is used as an initial value for CF/PEKK material in accordance with the laser incident angle used in this study [49], assuming that these materials have very similar material properties. All the required input parameters for the thermal model are summarized in Table 1 and the thermal properties of the CF/PEKK tape are $c_p = 1675 \text{ J/kg}\cdot^\circ\text{C}$, $\rho = 1506 \text{ kg/m}^3$, $k_x = 6 \text{ W/m}\cdot\text{K}$ and $k_y = 0.73 \text{ W/m}\cdot\text{K}$ at $200 \text{ }^\circ\text{C}$ [41].

Table 1. Overview of the required input parameters for the heat transfer model.

Parameter	Value	Parameter	Value
Tape thickness (t_t)	0.15 mm	Laser spot height (h)	8 mm
Tape illuminated width (w_t)	50.8 mm	Placement rate (v)	100 and 400 mm/s
Fraction of laser irradiance on the tape (h_t/h)	0.36	Laser angle (θ)	15°
Length of the illuminated tape (h'_t)	10.5 mm	Incoming tape temperature (T_t)	25 °C
Substrate thickness (t_s)	0.3 mm	Incoming substrate temperature (T_s)	155 °C
Substrate illuminated width (w_s)	56 mm	Air temperature (T_a)	25 °C
Fraction of laser irradiance on the substrate (h_s/h)	0.64	Tool's constant temperature (T_{tl})	155 °C
Length of the illuminated substrate (h'_s)	20.3 mm	Roller constant temperature (T_r)	25 °C
Absorptance (a)	0.6 [49]	Heat transfer coefficient of air-CF/PEKK (h_a)	20 W.K/m ² [32]
Domain length (l)	70 mm	Heat transfer coefficient of roller-CF/PEKK (h_r)	200 W.K/m ² [32]
Roller contact length (L_c)	16 mm		

2.3.1. Discretization of the FDM

In this study, the computational domain is composed of the substrate and the tape, which is represented as a two-dimensional rectangular region with the length of l and the width of t as given in Figure 6. The computational domain is discretized with equidistance structured mesh in the layup and through thickness directions with the mesh sizes of $\Delta x = 2 \times 10^{-4}$ m and $\Delta y = 1.5 \times 10^{-5}$ m, respectively, leading to the total mesh number of 350×33 . The steady-state energy balance equation with a convective energy transport in the layup direction and the associated boundary conditions are linearized using the finite difference approach as given in Equation (2.6), which are solved through developing an in-house code written in MATLAB. The first and second order derivatives are discretized with forward and central differencing schemes. The formulation presented

in Equation (2.6) is applied to all nodes with varying β_n coefficients depending on the position of the node in the domain to account for boundary conditions and source terms in the governing equation. The convective heat transfer term on the left-hand side of Equation (2.4) can impose a limitation on the mesh size in the layup direction due to the convergence of the numerical solution. To ensure that the numerical solution is convergent, Peclet number ($Pe = vL/\alpha$) should be less than unity, which is calculated to be 0.8 for this study where v is the velocity of the material flow, L is the maximum mesh size and α is the thermal diffusivity ($\alpha = k/\rho c_p$) [38]. This condition entails the usage of a rather small mesh size which drastically increases the computational time. Due to the dominance of convective heat transfer over the conductive heat conduction along the lay-up direction, the thermal conductivity in lay-up direction, k_x , has a rather small effect on the temperature field. Therefore, instead of reducing the mesh size for decreasing the values of Pe , the thermal conductivity can be increased artificially to reduce computational time significantly [50].

$$\begin{aligned}
& \beta_1[\rho c_p v_x \gamma (T_{m,n+1} - T_{m,n})] = \beta_2(T_{m,n} - 155) + \beta_3(T_{m,n} - 25) + \\
& k_x \gamma [\beta_4(T_{m,n-1} - T_{m,n}) + \beta_5(T_{m,n+1} - T_{m,n})] + k_y \frac{1}{\gamma} [\beta_6(T_{m+1,n} - T_{m,n}) + \\
& \beta_7(T_{m-1,n} - T_{m,n})] + \frac{\Delta x \Delta y}{2} (\beta_8 Q_s + \beta_9 Q_t) + \beta_{10} h_i \Delta x (T_i - T_{m,n}) + \\
& \beta_{11} [(T_{m+1,n} - T_{m,n})/R_c] + \beta_{12} (T_{m,n} - T_{m,n-1})
\end{aligned} \tag{2.6}$$

where $T_{m,n}$ indicates the node temperature and γ is equal to $\Delta y/\Delta x$. In Table 2, the coefficients of Equation (2.6) are provided for each part of computational domain.

Table 2. The β_n coefficients in Equation (2.6) for grid points based on location in computational domain.

Location of node	Region name			
	Heating	Shadow	Consolidation	Cooling
Top surface of the tape (B ₂ and B ₃)	$\beta_{7,\text{and } 10} = 1, \beta_{1,4,\text{and } 5} = 1/2, \text{ and } \beta_{2,3,6,8,9,11,\text{and } 12} = 0$ (For B ₂ : i = r and B ₃ : i = a)			
Bottom surface of the tape (B ₅₋₈)	For B ₈ : $\beta_{6,9-11} = 1$ $\beta_{1,4,\text{and } 5} = 1/2$ $\beta_{2,3,7,8,\text{and } 12} = 0$ $R_c = 10^{20} \text{ m}^2\text{K/W}$ i = a	For B ₇ : $\beta_{6,10,\text{and } 11} = 1$ $\beta_{1,4,\text{and } 5} = 1/2$ $\beta_{2,3,7,8,9,\text{and } 12} = 0$ $R_c = 10^{20} \text{ m}^2\text{K/W}$ i = a	For B ₆ and B ₅ : $\beta_{6,10,\text{and } 11} = 1$ $\beta_{1,4,\text{and } 5} = 1/2$ $\beta_{2,3,7,8,9,\text{and } 12} = 0$ R_c from Table 3	
Right side of the tape (B ₁)	$\beta_3 = 1$ $\beta_{1,2,4-12} = 0$	—		
Left side of the tape (B ₄)	—			$\beta_{12} = 1$ $\beta_{1-11} = 0$
Top surface of the substrate (B ₁₀₋₁₃)	For B ₁₀ : $\beta_{7,8,10 \text{ and } 11} = 1$ $\beta_{1,4,\text{and } 5} = 1/2$ $\beta_{2,3,6,9,\text{and } 12} = 0$ $R_c = 10^{20} \text{ m}^2\text{K/W}$ i = a	For B ₁₁ : $\beta_{7,10 \text{ and } 11} = 1$ $\beta_{1,4,\text{and } 5} = 1/2$ $\beta_{2,3,6,8,9,\text{and } 12} = 0$ $R_c = 10^{20} \text{ m}^2\text{K/W}$ i = a	For B ₁₂ and B ₁₃ : $\beta_{7,10,\text{and } 11} = 1$ $\beta_{1,4,\text{and } 5} = 1/2$ $\beta_{2,3,6,8,9,\text{and } 12} = 0$ R_c from Table 3	
Bottom surface of the substrate (B ₁₅)	$\beta_2 = 1 \text{ and } \beta_{1,3-12} = 0$			
Right side of the substrate (B ₉)	$\beta_2 = 1$ $\beta_{1,3-12} = 0$	—		
Left side of the substrate (B ₁₄)	—			$\beta_{12} = 1$ $\beta_{1-11} = 0$
Interior nodes	$\beta_{1,4-7} = 1 \text{ and } \beta_{2,3,8-12} = 0$			

2.4. Results and Discussion

2.4.1. Effect of Fiber Orientation on the Degree of Intimate Contact

Recalling from Section 2.2.3, the final degree of intimate contact between the incoming tape and the substrate is determined for region 2 given in Figure 5 through taking several microscopy images which are stitched together for detailed image processing. In Figure 7, representative stitched microscopy images are presented for three different laminates with the layup speed of 100 mm/s, where the final degree of intimate contact between the incoming tape and the substrate is determined by thresholding. Microscopy images between first and second layers with 1000 N force are provided in Figure 8.

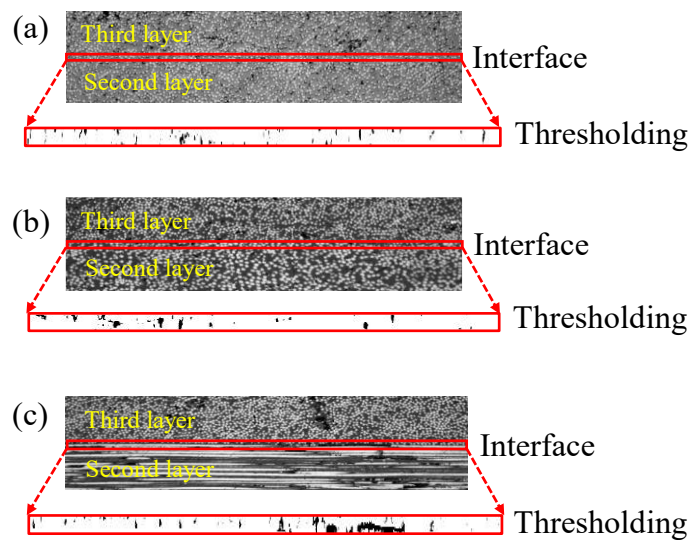


Figure 7. The degree of intimate contact between second and third layers for (a) $[0^\circ/0^\circ]$, (b) $[45^\circ/0^\circ]$ and (c) $[90^\circ/0^\circ]$ interfaces at the deposition speed of $v = 100$ mm/s.

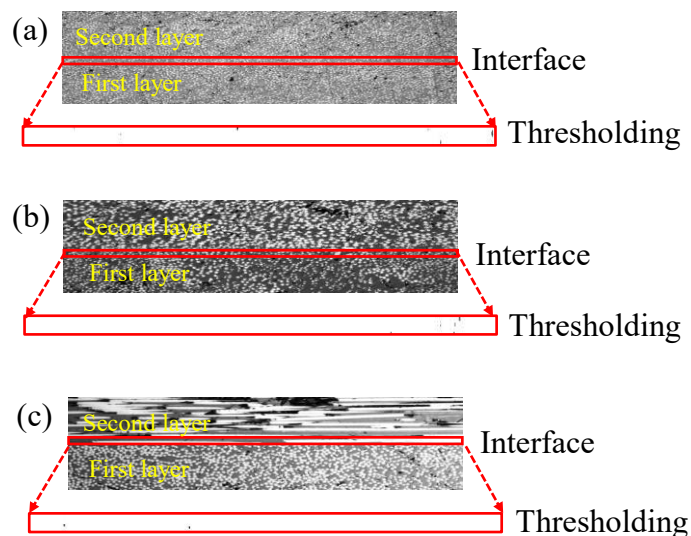


Figure 8. Degree of intimate contact between the first and second layers for (a) $[0^\circ/0^\circ]$, (b) $[45^\circ/0^\circ]$, and (c) $[90^\circ/0^\circ]$ interfaces at a layup speed of 100 mm/s.

The calculated intimate contact values calculated as the average value of four samples for three layup configurations with two different layup speeds of 100 mm/s and 400 mm/s are reported in Table 3 with their standard deviation values. The interface for UD fiber orientation has a higher degree of final intimate contact (D_{ic}) than the other two stacking sequences for both placement speeds, which can be related to two phenomena, namely, fiber nesting and permeability of the fiber bed. Nesting is a geometric phenomenon that occurs inevitably throughout the ply stacking process [40] such that when fiber bundles are aligned in parallel to each other, nesting is easily realized. Hence, the intimate contact between plies with the fiber same orientation is higher than those with different fiber orientations. Fiber beds have anisotropic permeability, which is higher when the resin flow is along the fiber axes (0° aligned fibers). As the angle of fiber orientation between successive plies increases, the permeability of fiber bed decreases due to the increase in tortuosity [51]. Accordingly, resin rich areas in UD fiber beds are higher than those in the cross-ply interface, thereby leading to the development of better intimate contact between successive layers in the UD laminate. Moreover, the results reveal that as the tape layup speed increases, the degree of intimate contact for all three stacking configurations decreases. This is because the consolidation time is reduced because of a higher placement rate. Consequently, the interface between the new incoming tape and the top surface of the substrate does not have sufficient time to develop full intimate contact.

Table 3. The degree of intimate contact and thermal contact resistance for different manufacturing conditions.

Stacking configuration	v (mm/s)	D_{ic} (%)	R_c (m^2K/W)
[$0^\circ/0^\circ$]	100	$94.6 \pm 7.42\%$	$2.549e-5$
[$45^\circ/0^\circ$]	100	$91.2 \pm 8.14\%$	$4.011e-5$
[$90^\circ/0^\circ$]	100	$84.3 \pm 7.67\%$	$7.344e-5$
[$0^\circ/0^\circ$]	400	$91.7 \pm 7.91\%$	$3.789e-5$
[$45^\circ/0^\circ$]	400	$86.2 \pm 6.58\%$	$6.373e-5$
[$90^\circ/0^\circ$]	400	$76.1 \pm 8.02\%$	$1.209e-4$

As can also be noticed from Table 3, the reduction in the degree of intimate contact at a higher layup speed ($v = 400$ mm/s) becomes greater with the increase in the angle of fiber orientation between different plies. Table 3 also presents thermal contact resistance

calculated for different manufacturing conditions. It can be easily noticed that the thermal contact resistance at the interface of the given plies is directly affected by the degree of intimate contact.

2.4.2. The Validation of Thermal Model

In Figure 9, numerically obtained thermal profile in the heating region of both substrate and tape is validated with the experimental data for different ply orientations and the placement speed of 100 mm/s. One can note that for the UD stacking sequence, there is a good agreement between the results of simulation and experiment for both tape and substrate, with the maximum difference of 3.75% and 3.21%, respectively. As for the other two stacking configurations, [45°/0°] and [90°/0°], the difference between numerically computed and experimentally measured thermal profile is slightly larger for the substrate but is the same for the tape in comparison to the UD configuration. The increasing difference between numerical and experimental thermal profile for the substrate as a function of fiber angle can be attributed to the possible uncertainty in the exact value of absorptance for the CF/PEKK composite material, which can affect the amount of laser energy reflected off, absorbed by, or transmitted through the composite material. The absorptance is typically influenced by laser wavelength, the volume fraction of constituents (fiber and matrix) in composite, and the orientation of fiber with respect to the laser heat source [16], [38], [39], [49], [52]. However, as the incoming tape is always in the UD state, its absorptance remains constant.

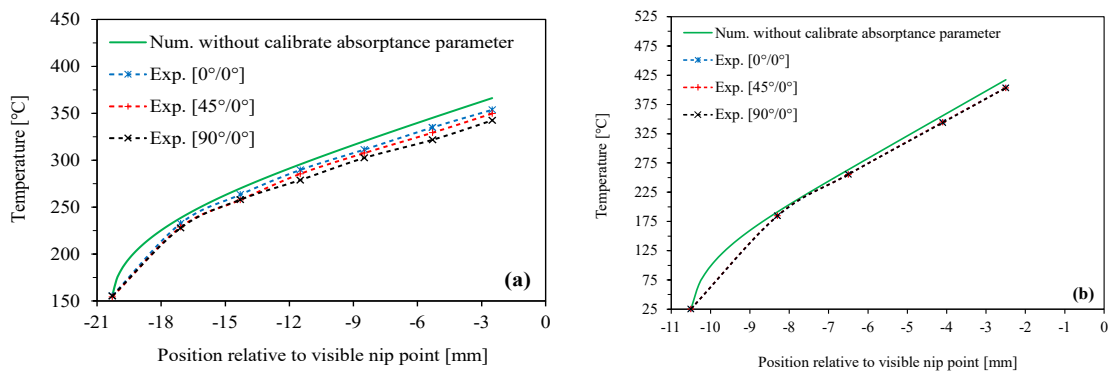


Figure 9. The comparison of experimental and numerical thermal profile for (a) substrate and (b) tape during the placement of the third layer with the layup speed of 100 mm/s.

To demonstrate that the absorptance significantly affects the temperature profile and being able to calibrate the experimental absorptance value obtained from the literature (0.6) with respect to the experimental thermal profile of this study, numerical simulations are performed using different absorptance for heating part of both substrate and tape. From these results, the absorptance that leads to the closest thermal prediction to the experimental thermal profile are determined such that the maximum difference between the numerical and experimental results is less than 1.5% as can be seen in Figure 10.

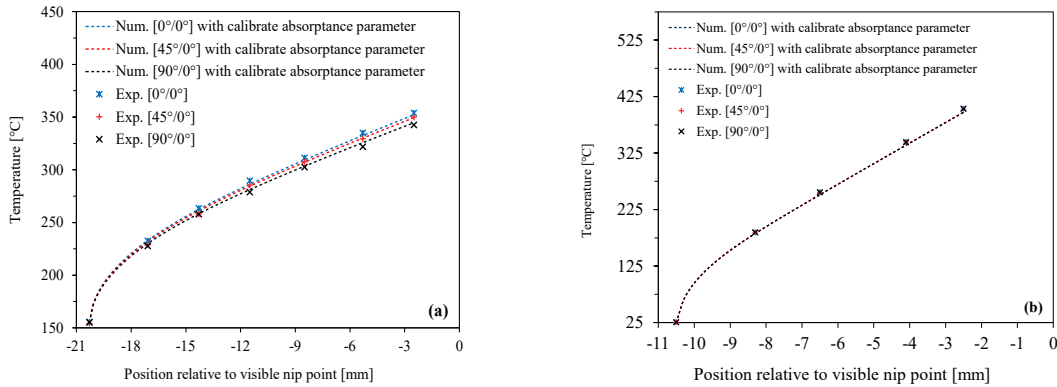


Figure 10. Numerically computed thermal profile with the calibrated absorptance parameter for (a) substrate and (b) tape surface during the placement of the third layer with the layup speed of 100 mm/s.

For the UD stacking sequence, the calibrated value of the absorptance parameter for the substrate and the tape is found to be 0.58. As for [45°/0°] and [90°/0°] stacking sequences, the calibrated values of the absorptance of the substrate laminate are determined to be 0.57 and 0.56, respectively. It is noticed that the absorptance of the substrate decreases by approximately 4% when the fiber angle of the substrate changes between [0°] to [90°]. It should be stated that the surface reflectance of composite is affected by the fiber orientation due to the anisotropic scattering [16], [39], [49], [50]. Since in this study, the incoming tape is always in the UD orientation with respect to the heat source, the reflectance of laser beams from tape on the substrate surface remains unchanged. However, the reflectance of laser beams from the substrate to tape surface will change depending on the fiber orientation of the substrate. It is observed that the experimentally measured surface temperature distribution of the tape with a thermal camera does not change much for different orientations of the substrate. To this end, in this study, the anisotropic scattering behavior of the composite is ignored.

2.4.3. Prediction of Thermal History

Figure 11 presents a numerically obtained representative temperature history of the substrate-tape interface at different regions of the layup for the UD configuration, which is obtained with the layup speed of 100 mm/s and with the assumption of the full degree of intimate contact (FIC), which means that there is no thermal contact resistance between new incoming tape and substrate ($R_c \sim 0$).

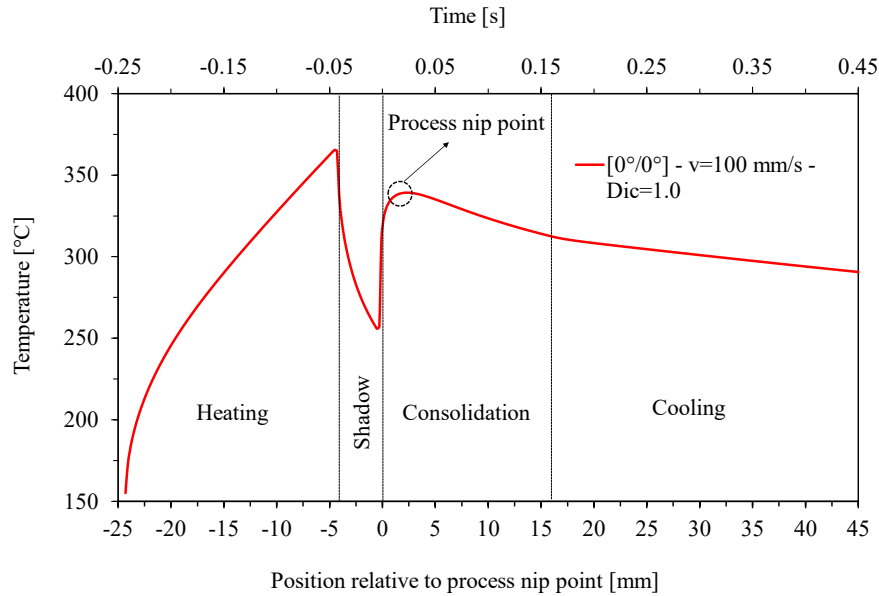


Figure 11. A representative numerical temperature history of the substrate-tape interface at different region of the layup for the UD configuration with the layup speed of 100 mm/s and full degree of intimate contact.

As can be seen from the Figure 11, the substrate surface is heated by a laser heat source to the highest temperature in the heating region. In the shadow region created by the deformation of the roller, the laser beam cannot illuminate the sections of the substrate and the incoming tape between the visible and the process nip points. Therefore, the substrate temperature begins to drop. In the consolidation region, which is adjacent to the shadow region, the top surface of the substrate and the bottom surface of tape come into contact and form an interface. Due to the higher temperature of the incoming tape, at the consolidation region, the interface temperature initially increases suddenly and reaches the process nip point temperature (T_{PNP}) and subsequently drops down. The fall in temperature continues in the cooling part with a lower cooling rate since the heat transfer coefficient of the roller is higher than the air.

2.4.4. The Effect of Fiber Orientation on the Temperature of Process Nip Point

In Figure 12 and Figure 13, the computed temperature history of the interface is shown for three different laminate configurations, which are manufactured with layup speed of 100 mm/s and 400 mm/s. For each laminate, the temperature distribution is calculated in two modes, namely, FIC ($R_c \sim 0$) and partial intimate contact (PIC where $R_c \neq 0$) at the interface. The value of R_c for each lamination configuration is provided in Table 3.

As shown from Figure 12 and Figure 13, the temperature history for PIC starts deviating from that for FIC at the onset of process nip point where the incoming tape and the substrate contact each other within the consolidation region. Although the process nip point occupies a very small region in the overall process domain, its temperature bears a direct relationship with the ultimate quality of the manufactured composite part in the LAFP process.

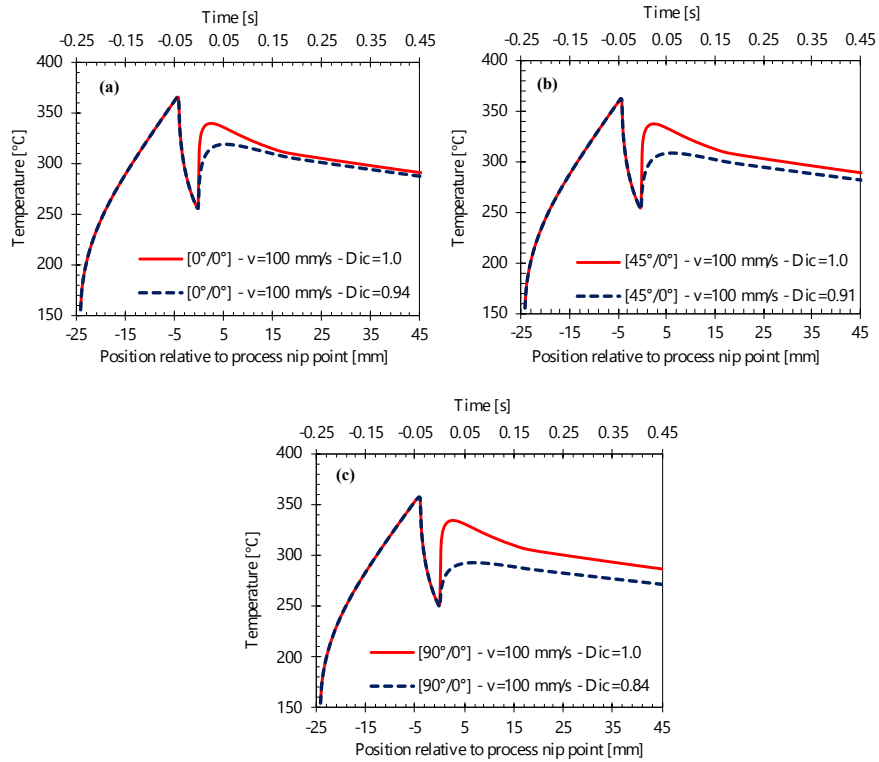


Figure 12. Temperature history prediction with thermal model for tape-substrate interface in different fiber orientation of substrate and layup speed of 100 mm/s.

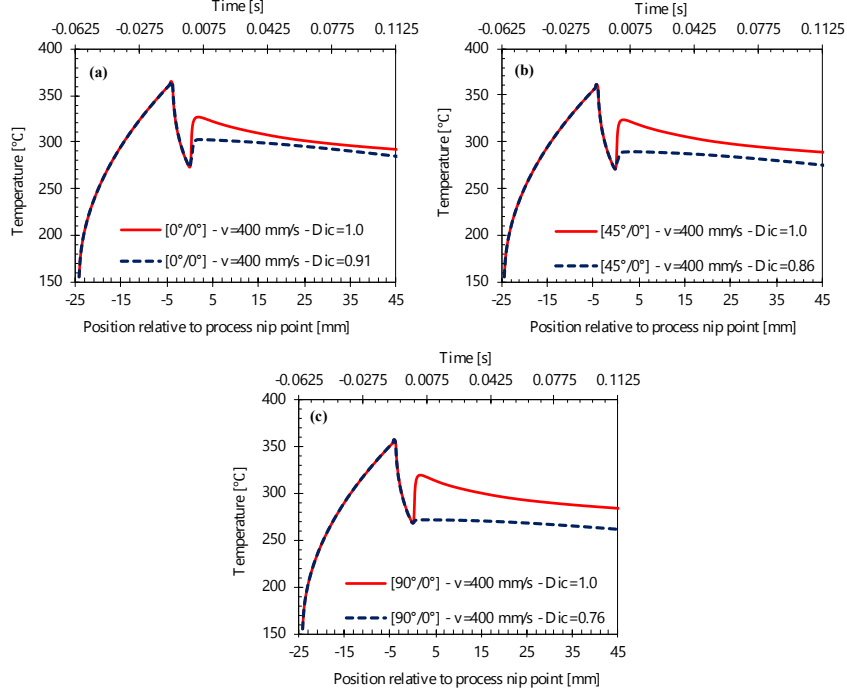


Figure 13. Temperature history prediction with thermal model for tape-substrate interface in different fiber orientation of substrate and layup speed of 400 mm/s.

The existence of thermal contact resistance in the case of PIC reduces the heat transfer between the incoming tape and the substrate. As a result, the T_{PNP} in PIC case is less than the one in FIC. By changing the fiber orientation of the substrate from $[0^\circ]$ to $[90^\circ]$, the difference between the process nip point temperatures of FIC and PIC cases increases. This observation is related to the reduction of degree of intimate contact at the interface of two sequential layers (Section 2.4.1). As a result of considering PIC in the thermal model for different fiber orientations, the percent change or improvement in the process nip point, $\delta_{T_{PNP}}$ can be expressed as Equation (2.7):

$$\delta_{T_{PNP}} = \frac{(T_{PNP})_{FIC} - (T_{PNP})_{PIC}}{(T_{PNP})_{PIC}} \times 100 \quad (2.7)$$

In Figure 14, $\delta_{T_{PNP}}$ is reported for all the cases. As can be seen from the figure, for both fiber placement rates, $\delta_{T_{PNP}}$ increases for substrates with fiber orientations of $[45^\circ]$ and $[90^\circ]$ due to the reduction in the degree of intimate contact. Moreover, there is a non-linear relation between the change in fiber orientation and $\delta_{T_{PNP}}$. Another important point to note is that considering the same fiber orientation in the substrate, the increase in the layup speed enhances the percent improvement in the process nip point, $\delta_{T_{PNP}}$, which is directly associated with the further reduction in the degree of intimate contact in higher

layup velocity for the same lamination configuration. These overall results emphasize the importance of including thermal contact resistance in the thermal model to predict the process nip point temperature accurately.

As stated in Section 2.4.1, at a higher fiber placement rate, the roller compaction time is reduced. Moreover, the substrate and tape pass the shadow region faster and thus experience a smaller temperature drop therein in comparison to the case with a lower fiber placement rate due to reduced convection to the ambient environment. As a result, the temperature at the onset of the consolidation region for both substrate and tape are higher for the higher fiber placement rate. At higher temperatures, the resin flow is enhanced because of the drop in the viscosity of resin. Therefore, it should be expected that a higher degree of intimate contact is achieved. However, referring to D_{ic} results in Table 3, the degree of intimate contact is lower at higher deposition rate. This discrepancy can be attributed to the fact that the effect of time duration for the applied roller pressure on the development of the degree of intimate contact is more prominent than temperature.

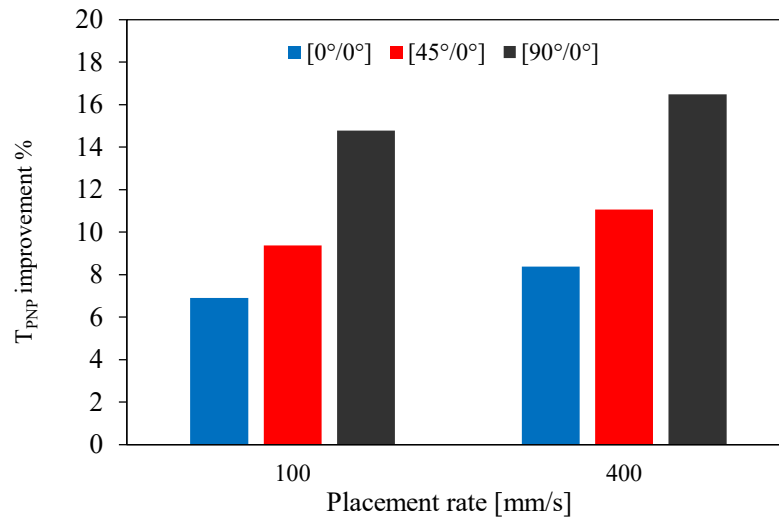


Figure 14. The percent improvement in the process nip point temperature, $\delta_{T_{PNP}}$ for different fiber orientations of the substrate at two layup speeds.

2.4.5. The Effect of Fiber Orientation on Temperature History of Consolidation Region

In the LAFP process, the temperature history in the consolidation region is rather critical and important since it affects the bonding, crystallinity, and residual stress of the manufactured part and governs the overall consolidation quality. Moreover, it is used as

an input for the other consolidation models [16], [32]. Hence, the accurate prediction of the temperature history in this region is of paramount significance. As previously discussed, one of the factors influencing the temperature distribution in the process domain is the fiber angle of the stacking sequence which has been shown to affect thermal contact resistance. From Figure 12 and Figure 13, the temperature in the consolidation region for FIC is higher than that for PIC. This difference becomes more prominent with increasing fiber orientation of the substrate and layup speed, which can be attributed to the decrease in the degree of intimate contact and the duration of the applied consolidation force. The temperature difference is the largest for the $[90^\circ/0^\circ]$ interface with a deposition speed of 400 mm/s, which indicates the importance of considering thermal resistance in the thermal model for the correct prediction of thermal history.

Figure 15 shows the simulation results of the thermal model for different fiber orientations at two layup speeds of 100 mm/s (solid lines) and 400 mm/s (dashed lines).

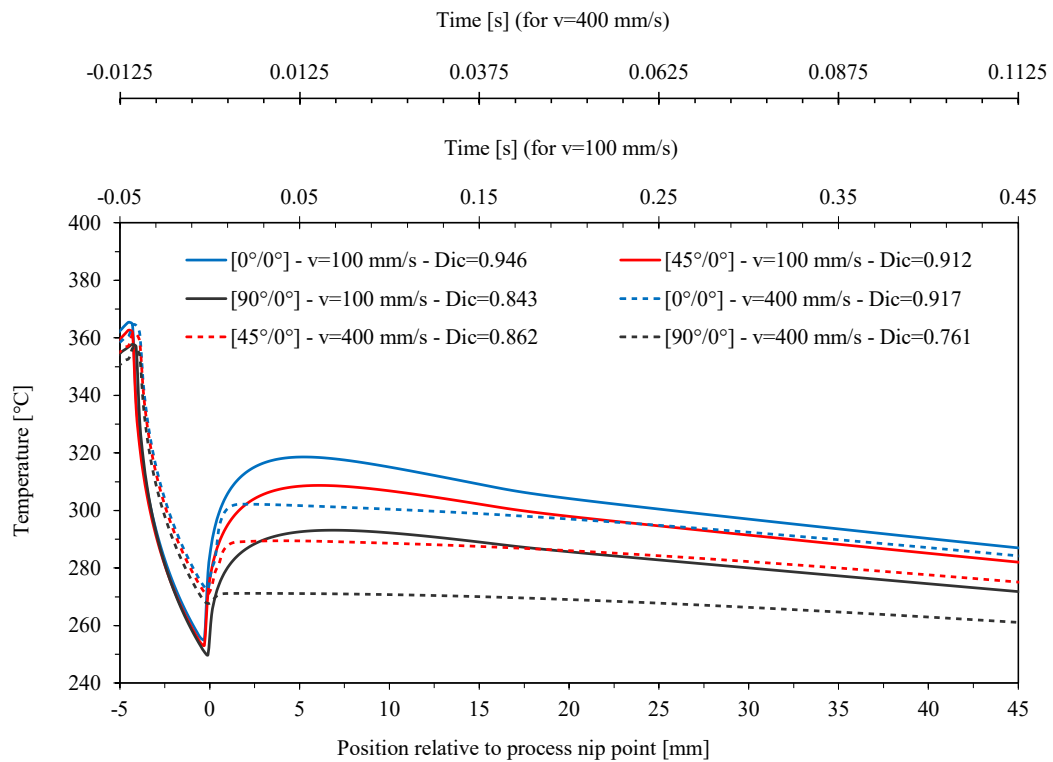


Figure 15. Prediction of temperature history for tape-substrate interface in different fiber orientations with two different layup speeds.

As expected, by increasing the fiber orientation difference between sequential layers, the amount of heat flow from the newly placed tape to the substrate decreases due to reduced degree of intimate contact between these layers. In both consolidation and cooling

regions, the difference in temperature distribution between $[45^\circ/0^\circ]$ and $[90^\circ/0^\circ]$ is greater than that between $[0^\circ/0^\circ]$ and $[45^\circ/0^\circ]$, which is further amplified at higher layup speed. Referring to Table 3, the reason for this outcome can be attributed to the non-linear relationship between decreasing intimate contact and increasing difference in fiber orientations of the sequential plies. The decrease in temperature within the consolidation region due to the fiber orientation and placement rate leads to the development of poor bonding quality. Moreover, upon increasing the layups speed from 100 mm/s to 400 mm/s, the duration of the applied consolidation pressure and heat conduction between the incoming tape and the substrate is naturally reduced by a factor of four, which adversely affects the bond quality of plies within the laminate.

2.4.6. The Effect of Fiber Orientation on Cooling Rate

The cooling rate is an important parameter in determining the degree of crystallinity of thermoplastic materials, which is regarded as an important property since it can notably affect the mechanical and thermal properties of laminated composite structures [9]. Thermoplastic composites processed at lower cooling rates have been reported to provide enhanced in-plane compressive, interlaminar shear strengths, mode-II fracture toughness, and impact resistance as the lower cooling rates render stronger interfacial bonds [53]. One may conclude from Figure 15 that at the same layup speed, stacking configurations with a higher process temperature profile at the interface of the substrate and tape result in a larger cooling rate at both consolidation and cooling regions. This is due to the higher rate of conductive heat transfer through the laminate thickness since the larger the temperature gradient, the higher the magnitude of the heat flux. Hence, the cooling rate decreases as the difference between fiber angles for successive layers increases. Moreover, by increasing the placement rate from 100 mm/s to 400 mm/s, a higher cooling rate is obtained, thereby decreasing the degree of crystallinity. The calculated cooling rates and degree of crystallinity within the consolidation and cooling regions for different laminate configurations are reported in Table 4. The aforementioned numerical observations are validated experimentally based on the degrees of crystallinity of the specimens, which are calculated using the melting enthalpies obtained from the melting peak of the DSC curves given in Figure 16.

Table 4. The calculated cooling rate within the consolidation and cooling regions for different specimen manufacturing.

Stacking configuration	v (mm/s)	Cooling rate in consolidation region (°C/s)	Cooling rate in cooling region (°C/s)	Degree of crystallinity, X _c (%)
[0°/0°]	100	116.84	71.95	17.94
[45°/0°]	100	84.23	66.01	18.26
[90°/0°]	100	62.57	56.76	18.76
[0°/0°]	400	132.22	198.08	17.10
[45°/0°]	400	96.75	167.69	17.37
[90°/0°]	400	73.18	121.3	18.20

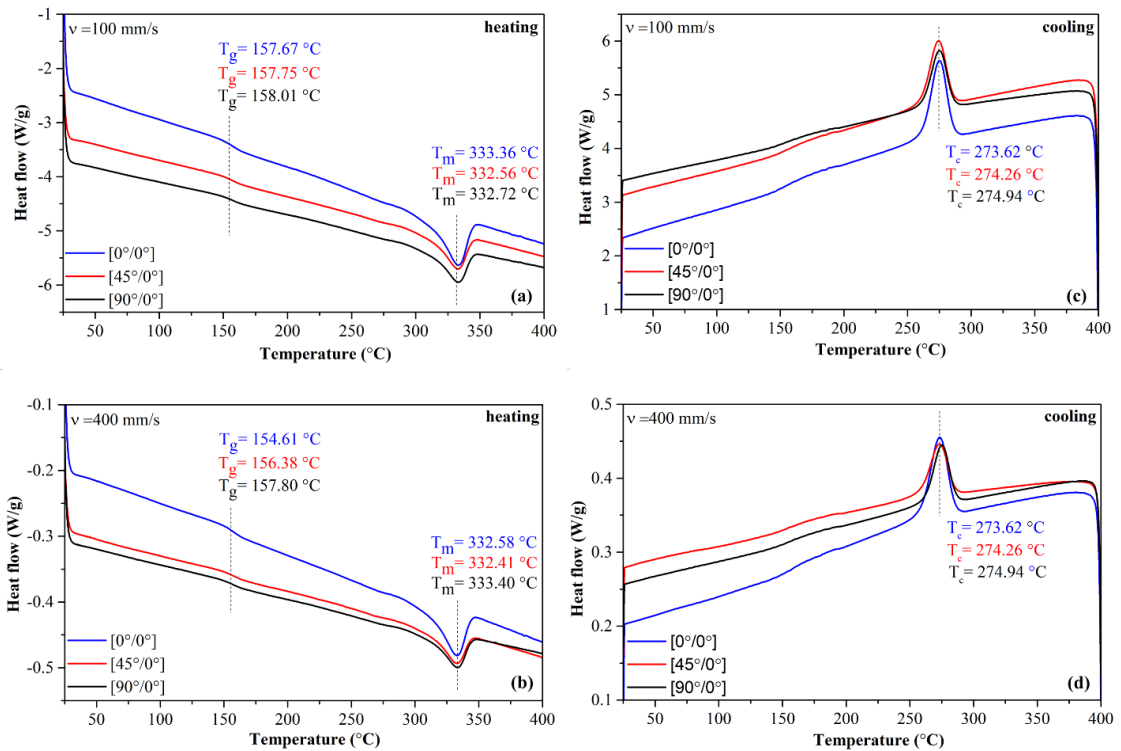


Figure 16. DSC heating and cooling curves of laminates with different fiber orientations at two layup speeds: (a) 100 mm/s (heating), (b) 400 mm/s (heating), (c) 100 mm/s (cooling), and (d) 400 mm/s (cooling).

The degrees of crystallinity of composite laminates with the layup speed of 100 mm/s and the stacking configuration of [0°/0°], [45°/0°], and [90°/0°] are determined to be 17.94 %, 18.26 %, and 18.76 %, in the given order, revealing an inverse relationship between the cooling rate and the degree of crystallinity. The decrease in the degree of crystallinity

with increasing cooling rate can be attributed to the fact that as the cooling rate increases, the polymer chains do not find enough time to fully organize themselves in the microstructure [54]. Additionally, as shown from Table 4, the same inverse relationship between the cooling rate and the degree of crystallinity (17.10 %, 17.37 %, and 18.20 %) is also obtained for specimens with a layup speed of 400 mm/s. Comparing the same stacking sequences for two different placement rates also shows an inverse relationship between the crystallinity and the placement rate. To this end, this study reveals that the mechanical properties of thermoplastic laminates can be additionally controlled by considering the fiber placement angle and rate, which influence the cooling rate during the layup process.

2.5. Summary

This study is a combined experimental and numerical effort to investigate the effect of thermoplastic fiber orientation on temperature distribution during the LAFP process. Composite laminates with three different stacking sequences are produced with low and high layup speeds employing the LAFP method. The degree of intimate contact is microscopically quantified and then used to determine thermal contact resistance (R_c) between two subsequent layers. Experimental results show that the increase in the fiber orientation between subsequent plies reduces the degree of intimate contact and, in turn, raises R_c . This phenomenon is more prominent at a higher layup speed. A two-dimensional thermal model is developed to predict the temperature history of the manufactured part while accounting for the effect of R_c . The numerical simulations reveal that as the difference in the fiber orientation of subsequent plies increases, the consolidation region temperature curve for the tape-substrate interface shifts down. Upon comparing numerical results for different fiber stacking sequences and layup speeds, one can clearly note a strong relationship between substrate fiber orientation and temperature history at both low and high layup speeds. Specifically, the cooling rate in consolidation and cooling regions increases as the fiber angle difference decreases. Moreover, based on DSC analysis for determining melting enthalpies, the degree of crystallinity for all specimen configurations is calculated and then correlated with cooling rates. The results reveal an inverse relationship between the degree of crystallinity and the cooling rate. The

findings of this study clearly show that the thermal history developed during manufacturing should be incorporated into the design stage of composite structures where fiber orientations are determined.

**CHAPTER 3: ENHANCING INTERLAMINAR BONDING QUALITY
ESTIMATION IN LASER-ASSISTED FIBER PLACEMENT OF CF/PEKK
COMPOSITES: A CORRECTION FACTOR APPROACH FOR IMPROVED
PREDICTION OF INTIMATE CONTACT**

This chapter introduces an innovative Modified Mantell and Springer (MMS) model to more accurately assess degree of intimate contact with improved accuracy, which also significantly enhances the subsequent degree of healing estimation and enables the presentation of an improved degree of bonding. Process parameters such as placement speed and consolidation forces, and fiber orientation are identified as key determinants of bonding quality. Lower placement speeds and higher consolidation forces are linked to increased healing intimate contact between layers, crucial for achieving desired degree of bonding. The MMS model proves effective in capturing the influence of fiber orientation, revealing that $[0^\circ/0^\circ]$ orientation exhibits superior bonding strength. Validation through T-peel tests provides tangible evidence of the model's precision, aligning fracture surface observations with model predictions. This research contributes to a comprehensive understanding and prediction of composite bonding quality, offering valuable insights for optimizing manufacturing processes and enhancing the mechanical performance of composites manufactured with Laser-Assisted Fiber Placement (LAFFP).

3.1. Introduction

In recent years, the composite industry has undergone a significant transformation with the increasing adoption of automation, particularly through advanced manufacturing processes like Automated Fiber Placement (AFP) [55]. The AFP method involves the fabrication of composite structures layer by layer, utilizing either gantry-type or robotic systems to precisely place continuous fibers in accordance with design requirements onto

a mold even with complex geometries. It revolutionizes composite fabrication, offering advantages such as increased production rates, improved part quality, reduced material waste, and enhanced design flexibility with a material selection opportunity such as thermosets, thermoplastics and dry fiber tapes [56], [57]. Particularly, the possibility of using high-performance thermoplastic resin systems (i.e., Polyether Ether Ketone (PEEK) [18], [48], [58], Polyether Ketone Ketone (PEKK) [59], [60], Polyphenylene Sulfide (PPS) [46], [61], and Polyetherimide (PEI) [62], [63]) in the AFP process further widens efficient manufacturing windows of advanced composites. These thermoplastic resin systems exhibit exceptional mechanical properties, chemical resistance, and recyclability and when processed with AFP method, they can significantly contribute to attainment of shorter processing times, enhanced part consolidation, and superior damage tolerance [64].

Ongoing advancements in AFP technology have led to the development of laser-assisted fiber placement (LAFP), a cutting-edge approach that combines the precision of AFP with the versatility of laser technology. In LAFP, lasers are employed to heat up thermoplastic resin or prepreg, which is immediately consolidated with a consolidation roller. During the LAFP process, a lamina is formed by laying up strips of thermoplastic tape juxtaposed on a mold or substrate following laser heating and roller consolidation. In a typical LAFP layup process, there exists four successive phases, namely, heating, shadowing, consolidation, and cooling. During the heating phase, the incoming flexible tape (composed of fiber and matrix) is heated. In the second stage, the deformation of the non-rigid roller prevents the laser heat flux from reaching the tape and substrate surface. During the consolidation phase, the incoming tape is deformed and pressed toward the substrate because of applied pressure by the roller. Finally, in the cooling stage, the newly placed lamina experiences no additional roller pressure and starts cooling down and accelerated crystallization takes place based on the selected cooling rate [9]. One of the most critical steps in the LAFP process is the consolidation since it significantly influences the interlaminar bond strength between successive layers or lamina. The successful consolidation in LAFP process can pave a way towards in-situ consolidation, which may potentially eliminate the need for post-processing after layup with the thermoplastic resin systems. In situ consolidation is a compelling goal for time- and energy-efficient manufacturing of advanced composite structures. Thus, a secondary consolidation processes like autoclave, Out of Autoclave (OoA), and hot press molding

are required to obtain aerospace-grade performance, especially for large and complex geometries [65], [66]. Additionally, 3D printing provides excellent formability for complex shapes but may not yet match the mechanical properties achievable with LAFP [67], [68]. Therefore, to facilitate in-situ consolidation gaining a comprehensive understanding of the underlying physical phenomena behind the consolidation process is of paramount importance.

Inherently, a consolidation process in thermoplastic layup involves two critical mechanisms which directly control bonding quality and in turn strength with the laminate: the formation of intimate contact that is quantified by the degree of intimate contact (D_{ic}) which is defined as the ratio of the area in contact to the entire interface area, and the creation of a fusion bond, to the extent to which its quality is determined by the degree of healing (D_h) [69]. In the context of AFP, intimate contact pertains to the close physical proximity of two adjacent layers of thermoplastic composite material during the fiber placement process. This involves the dispersion of surface asperities, which are microscopic roughness features between two plies that are in physical contact [70]. The degree of intimate contact is affected by various parameters, including process temperature, consolidation force, fusion time, and the viscosity of the mixed fiber-matrix system, essentially, all parameters affecting AFP lamination process [11]. To this end, understanding the stages in the formation of full intimate contact from multiple perspectives is crucial since it plays an important role in controlling the bonding strength between successive plies and thereby directly affect the overall mechanical and thermomechanical performance of the manufactured laminate [71]. To be specific, the intimate contact facilitates bonding between surfaces through diffusion and entanglement of polymer molecules via reptation, a process operative only in regions of intimate contact [72]. Moreover, intimate contact influences the inter-laminar void content of the final structure. The presence of voids can lead to fractures and degrade the mechanical performance of the final product, particularly concerning inter-laminar shear strength, compression strength, transverse tensile strength, and fatigue life [32], [68], [73], [74]. Additionally, insufficient intimate contact can reduce heat transfer across the ply interfaces, impacting temperature-induced issues such as lower crystallinity, insufficient healing, formation of void compaction/decompression, and the emergence of residual stresses during LAFP [14]. Consequently, developing a clear understanding on the degree of intimate contact through a combined experimental and computational modeling studies

becomes essential. Such a combined approach lends itself to establishing a reliable and accurate correlation between AFP lamination process parameters and final product quality.

There is several modeling efforts in literature dedicated to predicting the degree of intimate contact between two surfaces to be bonded. Dara and Loos [75] developed an intimate contact model for a prepreg system through the integration of the viscoelastic characteristics of the resin with reinforced fibers, the uneven distribution of tow height, and the processing factors of pressure, temperature, and time. They employed a statistical distribution of geometric non uniformity of tow heights to describe the roughness at the ply interfaces and modeled the viscoelastic response of the thermoplastic based on the squeezing flow of homogeneous fluid between two plates. Lee and Springer [44] simplified this model [75] by employing a series of rectangles with identical height and width separated by equal-width spaces. They proposed a one-dimensional laminar Newtonian flow of asperities (rectangles) into the gaps and calibrated the dimensions of rectangles to better capture the experimental results. However, this model ignores the variation of pressure and viscosity over time. Mantell and Springer [76] improved Lee and Springer's model by incorporating time-dependent properties of both applied pressure and viscosity. In literature, this model has been adapted for the AFP process since it considers these two critical AFP process variables, namely, pressure and viscosity. Furthermore, there are several other models for predicting the degree of intimate contact between two surfaces to be bonded in composite manufacturing. Yang and Pitchumani [21] proposed a model based on fractal Cantor set construction for depicting surface roughness, and squeeze flow for resin flow modeling, thus avoiding the simplistic use of identical rectangles in previous models. Kok [32] proposed empirical model to study intimate contact based on key process parameters in the LAFP process. This model considers the penetration of matrix material to saturate dry fibers on the tape's surface. Although Kok's model [32] underestimated the degree of intimate contact compared to experimental data, it could qualitatively predict how process parameters influence the degree of intimate contact. Celik et al. [41] introduced concept of "effective intimate contact," which is calculated experimentally through accounting for resin content on the surface of a composite material. The experimentally obtained degree of effective intimate contact was then compared to existing models in literature. This study of Celik et al. [41] demonstrated that it is essential to consider the through-thickness percolation flow of

resin (resin flow into dry fiber beds at the interface) to have more accurate intimate contact prediction in addition to the squeeze flow mechanism upon which previous intimate contact models have been built. Khodaei and Shadmehri [77] have recently suggested an experimental approach, referred to as “BAC method,” which combines the uniform rectangular model with the Bearing Area Curve (BAC) constructed from surface roughness. This approach was utilized to analyze how different AFP process parameters impact the degree of intimate contact.

Considering the tradeoff between simplicity/applicability and accuracy of previously discussed intimate contact models in literature, the Mantell and Springer model (MS model) [76] has become widely preferred approach in numerous studies to investigate the effect of AFP process parameters such as placement speed, consolidation force, heat source intensity, and tool temperature on the degree of intimate contact [18], [28], [69], [78]. Albeit its wide acceptance in the field, the MS model has two significant shortcomings that need to be addressed. First, it assumes that the transverse squeeze flow of surface asperities is the fundamental mechanism for intimate contact development while ignoring percolation flow. As a result, the degree of intimate contact is underestimated [32], [41]. Second, the model overlooks the effect of fiber orientation at the interface on the degree of intimate contact. However, it has been shown in Chapter 2 that, in addition to the LAFP process parameters, the variation in fiber orientation between two subsequent layers affects the degree of intimate contact and heat dissipation at the interface. Despite the progress made by various models in accurately predicting the degree of intimate contact in the LAFP process, there remains a need for a practical and reliable model that effectively combines the advantages of existing approaches while addressing the limitations in question.

Moreover, under the influence of heat and pressure during LAFP layup, the thermoplastic material undergoes a process of polymer chain diffusion and rearrangement at the interface. This phenomenon is known as healing and leads to the formation of intermolecular bonds. Healing process amplifies the strength of bonding between neighboring plies as a result of rejoining or fusion that occurs at the interfaces within thermoplastic composites [79]. The degree of healing (D_h) is defined as the ratio of the actual bond-line strength to maximum achievable strength of the material system. The healing process is influenced by various factors, such as temperature, pressure, and time, as well as the material properties of the thermoplastic matrix and the carbon fiber

reinforcement. The degree of healing is a critical parameter in composite manufacturing, particularly in processes like LAFP, where precise control of interfacial bonding is essential for achieving structural integrity and optimizing the mechanical performance of the final product. Accurate modeling and assessment of the degree of healing lends itself to the design and production of advanced thermoplastic composites with optimized and enhanced mechanical performance. In this context, the movement of polymer chains at ply interfaces has been studied under isothermal conditions by Gennes [80], with further developments by Wool [81]. Nonetheless, it is important to bear in mind that the in-situ thermoplastic LAFP method inherently involves significant non-isothermal process phases. To address this, different degree of healing models has been developed by Bastien and Gillespie [82] and Sonmez and Hahn [28]. These models are based on reptation theory [80]. Additionally, Yang and Pitchumani [72] developed a non-isothermal model based on the fundamental principles of reptation theory. The outcomes of the model were compared with the results of non-isothermal experiments for CF/PEEK and CF/PEKK wherein a good correlation between the model and experiments were reported [72], [83]. Consequently, the model developed by Yang and Pitchumani have been widely used in various studies related to the AFP process [18], [37], [69], [84], [85], including this study.

It should be recalled that both the degree of intimate contact and healing are crucial inputs in evaluating the degree of bonding within the laminates [28], [69]. Proper bonding has a direct impact on the strength and efficiency of the interfacial bond which controls the level of load transfer within composite structure and in turn its and overall mechanical performance. Specifically, insufficient bonding can lead to premature damage formation such as delamination and therefore compromises structural integrity and durability of the composite structure subjected to various loading conditions.

This study presents an overarching approach to shed light on the physics behind the bonding process and then proposes a novel model which can accurately and robustly predict bonding quality across composite plies in the LAFP process. Initially, our model modifies MS model by introducing an experimentally obtained correction function for degree of intimate contact, which accounts for the fiber orientation and LAFP process parameter (placement speed and consolidation force). Henceforth, this modification will be referred to as the modified MS model, abbreviated as MMS. The correction factor in this study refers to the ratio of the experimentally obtained intimate contact based on image processing and the intimate contact calculated using the formulation of the MS

model. The intimate contact values calculated using the proposed MMS model are validated experimentally as well as the results of literature. Recall that intimate contact affects computationally obtained thermal profile during the LAFP process, which directly controls the degree of healing through thermal contact resistance. Hence, in the calculation of thermal profile, the degree of intimate contact based on MMS model is utilized thereby incorporating the influence of fiber orientation and LAFP process parameters on the degree of healing. Having accurately predicted the degree of intimate contact and healing values, the degree of bonding is calculated and then validated with respect to the experimental results generated using T-peel tests on the fabricated samples. The degree of bonding is also analyzed with Scanning Electron Microscopy (SEM) imaging of fracture surfaces, particularly understating the impact of fiber orientation on the bonding quality. To recapitulate, the proposed model advances the understanding and prediction of composite bonding quality and can serve as a valuable approach or tool for optimizing manufacturing processes, which can enhance the mechanical performance of composite materials manufactured with LAFP.

3.2. Materials and Experimental Methods

3.2.1. Laser-Assisted Fiber Placement System and Sample Manufacturing

The LAFP system used in this study is equipped with a robotic fiber placement head as an end-effector, capable of continuously laying up eight side by side 6.35 mm wide slit tapes at a maximum speed of 800 mm/s. The system involves a 6-kW laser heat source (Laserline LDF series diode laser unit) having a 250 mm focusing optic lens, which can produce a rectangular laser spot with an illuminated area of 8 mm by 56 mm. For a consolidation step, a deformable consolidation roller with a Shore hardness of 60 and a diameter of 70 mm is utilized in the process [86]. To monitor temperatures, long-wave infrared (LWIR) cameras are employed to measure the surface temperature of the substrate and incoming tape until the nip point. The non-contact temperature measurement is achieved at 80 frames per second using the Optris PI 400i camera with a detector resolution of 382 x 288 pixels. The camera is calibrated with a temperature range of -20 °C to 900 °C and elicits an accuracy of ± 2 °C.

In this study, the LAFP machine is used to laminate three layers of samples of thermoplastic slit tapes, obtained from Toray Cetex Company with the manufacturing code of TC1320 CF/PEKK. These tapes have a fiber volume fraction of 66%, a thickness of 0.15 mm, and a width of 6.35 mm [87]. For the manufacturing of samples, two different stacking sequences, $[0^\circ/0^\circ/0^\circ]$ and $[0^\circ/90^\circ/0^\circ]$, are employed to form laminates, each with a length of 1100 mm and a width of 50.8 mm. During all layup processes, the tool temperature is set to 155 °C. The layup process involves utilizing specific process parameters for placement speed, consolidation force, and fiber orientation, with corresponding laser power values for each sample as listed in Table 5. An additional set of Sample #2 is manufactured with LAFP and then post-processed with autoclave using the recommended process parameters [87]. This sample is used as a reference in T-peel tests for calculating the experimental degree of bonding ($D_{b,exp}$).

Table 5. Process parameters for LAFP placement trials of the samples.

Sample No.	Substrate fiber orientation	Tape fiber orientation	Placement speed (mm/s)	Consolidation force (N)	Corresponding laser power (W)
1	$[0^\circ]$	$[0^\circ]$	100	300	1386
2	$[0^\circ]$	$[0^\circ]$	100	600	1386
3	$[0^\circ]$	$[0^\circ]$	400	300	3427
4	$[0^\circ]$	$[0^\circ]$	400	600	3427
5	$[90^\circ]$	$[0^\circ]$	100	300	1386
6	$[90^\circ]$	$[0^\circ]$	100	600	1386
7	$[90^\circ]$	$[0^\circ]$	400	300	3427
8	$[90^\circ]$	$[0^\circ]$	400	600	3427

In the LAFP process, the microstructure of the composite laminate can be affected by variations in speed, acceleration, and deceleration of the robot head during the landing and take-off phases. Thus, T-Peel test samples with dimensions of 200 mm length and 20 mm width are obtained from the central portion of the laminates where uniform process parameters are achievable. To facilitate the separation of the layers and to create peel arms for the T-peel test, 50 mm strips of polyimide tape are affixed to the interlaminar area during the lamination process. For microscopic imaging to determine the

experimental degree of intimate contact, additional samples are cut from around the central regions, adjacent to the T-peel test samples.

3.3. Contact Length and Pressure for the LAFP System

In this study, the Mantell and Springer (MS) model [76] is employed to calculate the initial numerical degree of intimate contact, which is based on the contact length (to obtain the consolidation time) and pressure distribution in the intimate contact area between the incoming tape and the substrate (see Section 3.6.1). To accurately integrate the contact length and the pressure data during the consolidation for the available LAFP system, experimental measurements are conducted at different roller consolidation forces.

For this purpose, the Fujifilm Prescale LLLW model, designed for ultra super low-pressure measurements ranging from 0.2 to 0.6 MPa and functioning within a temperature range of 20°C to 35°C, is employed as a pressure-sensitive film. This film consists of two layers: an A-Film coated with micro encapsulated color-forming material and a C-Film coated with color-developing material (Figure 17). The application of pressure causes the micro capsules in the A-Film to rupture, leading to a reaction between the color-forming material and the color-developing material on the C-Film. This reaction produces a red hue whose intensity varies based on the magnitude of applied pressure. To measure the contact length and pressure, the Fujifilm Prescale film is affixed to the tool, as shown in Figure 17, and a series of consolidation forces, ranging from 100 N to 900 N with increments of 200 N, are applied. The mean contact length (L_c) for a given roller force is calculated as an average of discrete contact lengths across the red-colored Fujifilms due to the applied roller pressure. Figure 17 presents red-colored Fujifilms with eight equally spaced discrete contact lengths represented by dashed vertical lines for a roller force of 500 N. Subsequently, the mean contact length is incorporated into the thermal model previously developed, as described in Chapter 2, to calculate the degree of intimate contact and healing.

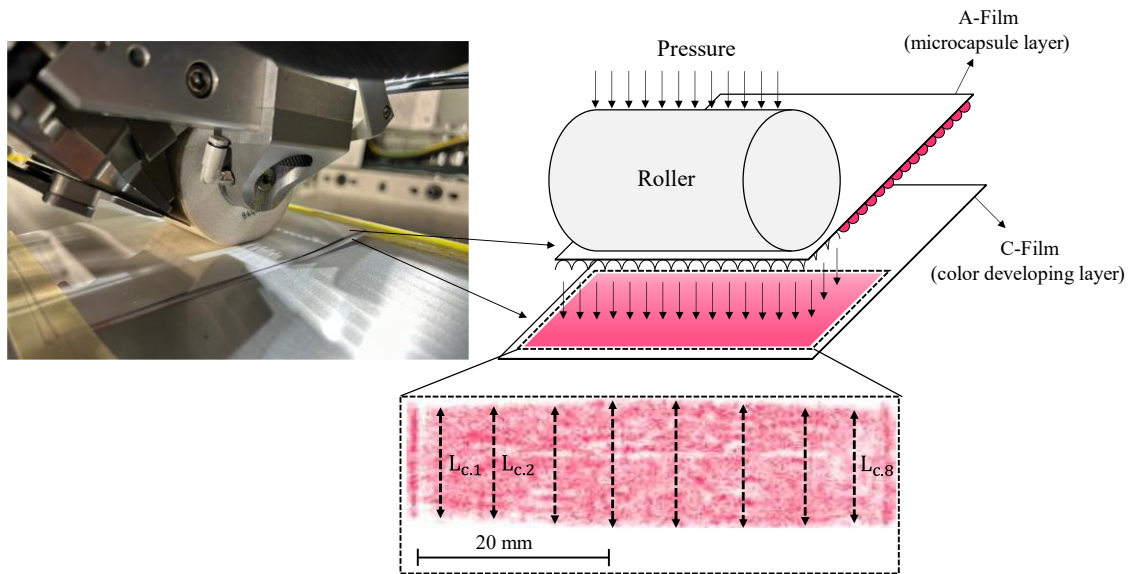


Figure 17. Contact length and static pressure measurement by utilizing pressure sensitive film with the LAFP device.

For the pressure evaluations, Figure 18 outlines the process for translating Fujifilm color density to pressure values. Initially, Fujifilm's color density scales are converted into a grayscale-color density chart using ImageJ software (Figure 18 (a)). The red Fujifilm samples from roller pressure tests are also grayscale-converted using ImageJ, generating the average gray scale value X_1 (Figure 18 (b)). Using the gray scale-color density chart, the corresponding color density value X_2 for X_1 is determined. Subsequently, the Fujifilm Corporation's pressure-color density chart (Figure 19) is used to derive the corresponding pressure value X_3 based on the determined X_2 color density (Figure 18 (c)). This systematic procedure converts obtained grayscale values (X_1) into corresponding pressure values (X_3) via intermediary color density values (X_2), leveraging data from ImageJ and Fujifilm Corporation. Moreover, Figure 19 presents a comprehensive diagram illustrating the relationship between color density, grayscale, and pressure. The color density-pressure chart provided by Fujifilm Corporation, tailored for the LLLW model, encompasses pressures up to 0.6 MPa and the diagram notably exhibits a linear pattern for elevated pressures. This linear trend is extrapolated (highlighted by the dashed lines) up to a color density of 1.3 to represent the pressure values up to 0.9 MPa.

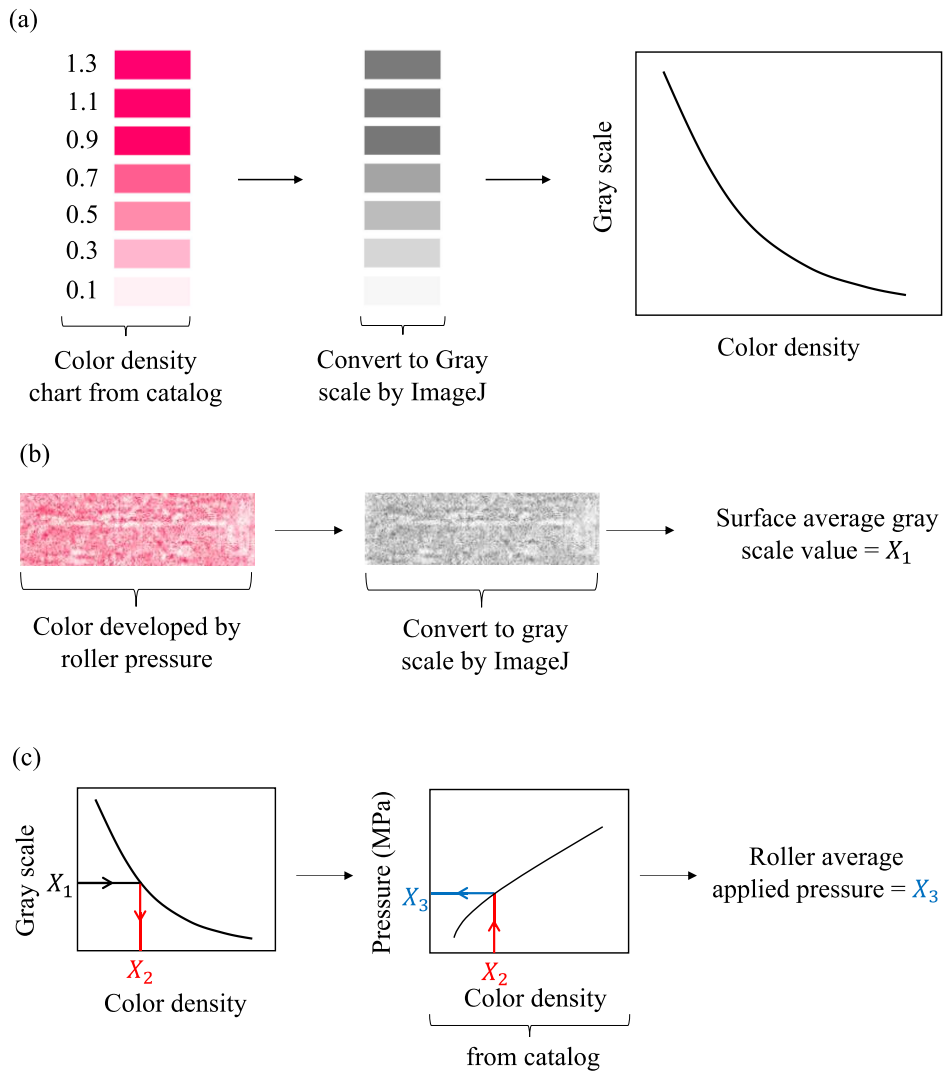


Figure 18. Procedure for converting Fujifilm color density to pressure values in the contact area.

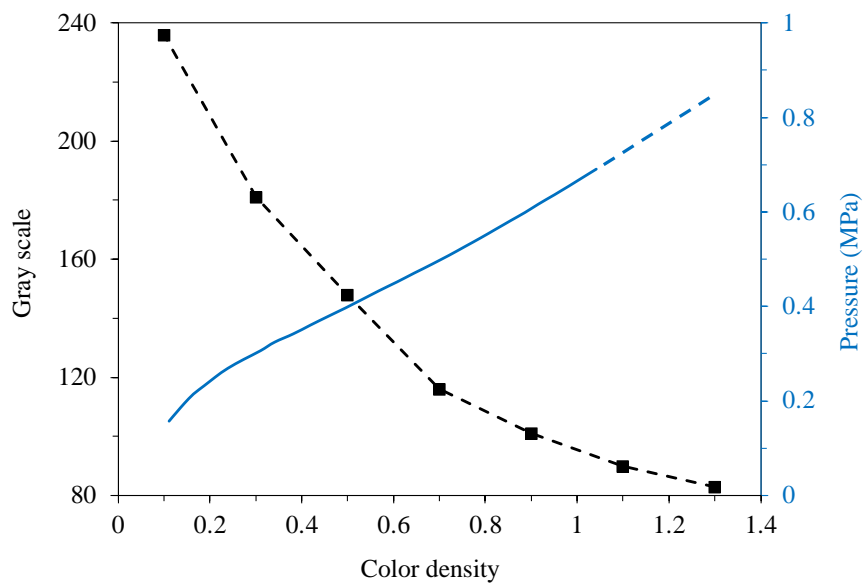


Figure 19. Change in grayscale and pressure with the color density of the LAFP device.

Figure 20, illustrates the contact length and pressure measurements obtained from the respective Fujifilm patterns at each consolidation force. Notably, nonlinear relationships are evident for both contact length and consolidation pressure concerning the consolidation force. These observations align with the conclusions drawn in earlier studies conducted by Celik et al. [41] and Khodaei and Shadmehri [77].

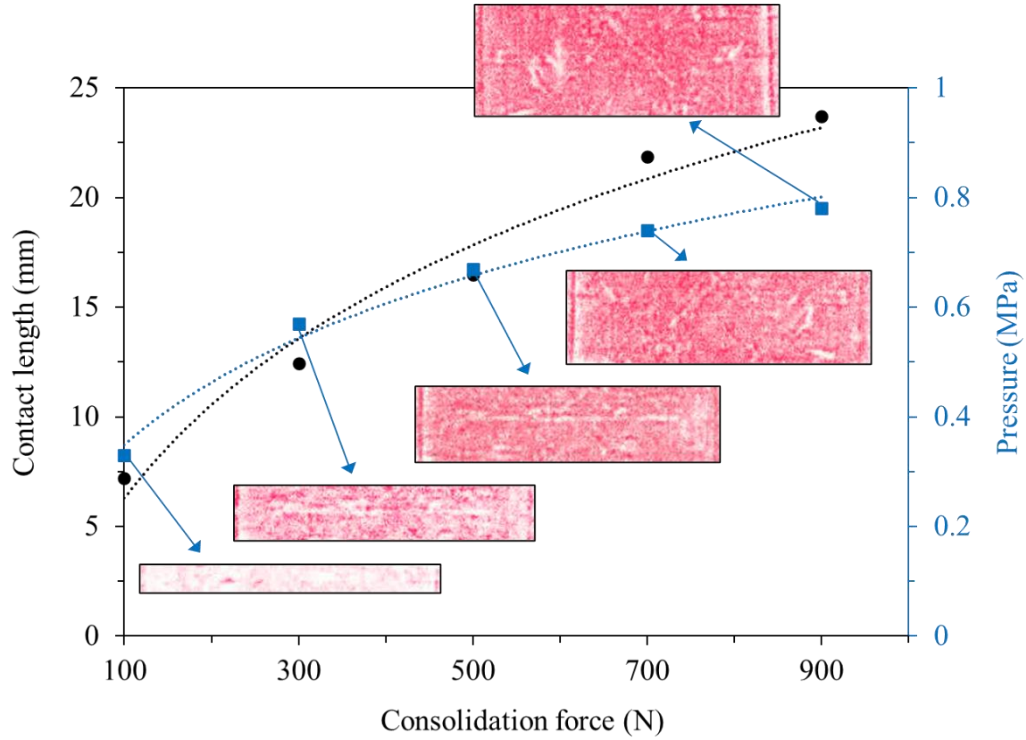


Figure 20. Nonlinear behavior of the roller applied consolidation force in relation to the contact length and consolidation pressure.

To be able to obtain continuous values for mean contact length and roller pressure, corresponding discrete values are curve fitted as a function of consolidation force using a logarithmic function with the R^2 values of 0.9716 and 0.9872 for L_c and P_{app} , respectively. The resulting equations are as follows:

$$L_c = 10.509 \ln(F) + 6.2821 \quad (3.1)$$

$$P_{app} = 0.2809 \ln(F) + 0.3491 \quad (3.2)$$

where L_c in [mm] for contact length during roller compaction, F in [N] for applied consolidation force as set value and P_{app} in [MPa] stands for applied consolidation pressure.

3.4. Experimental Degree of Intimate Contact Measurement

To assess the experimental degree of intimate contact ($D_{ic,exp}$), the methodology detailed in Chapter 2 is followed. The coupons selected for microscopic analysis (as described in Section 3.2.1) are embedded in epoxy and polished with different grits of sandpaper. The intimate contact is then examined using a Nikon ECLIPSE LV100ND microscope equipped with a 50X objective. This evaluation involves stitching, grayscale conversion, and thresholding analysis steps for each sample. Moreover, this procedure is repeated three times for all samples obtained from different locations. Figure 21 provides illustrative examples, showing two microscopy images with grayscale representations and the intimate contact regions of the top interface used for the $D_{ic,exp}$ evaluation. Specifically, samples manufactured with a placement speed of 100 mm/s and consolidation force of 600 N with the stacking sequences of $[0^\circ/0^\circ/0^\circ]$ (Sample #2 - subject to LAFP consolidation only) and $[0^\circ/90^\circ/0^\circ]$ (Sample #6) are considered.

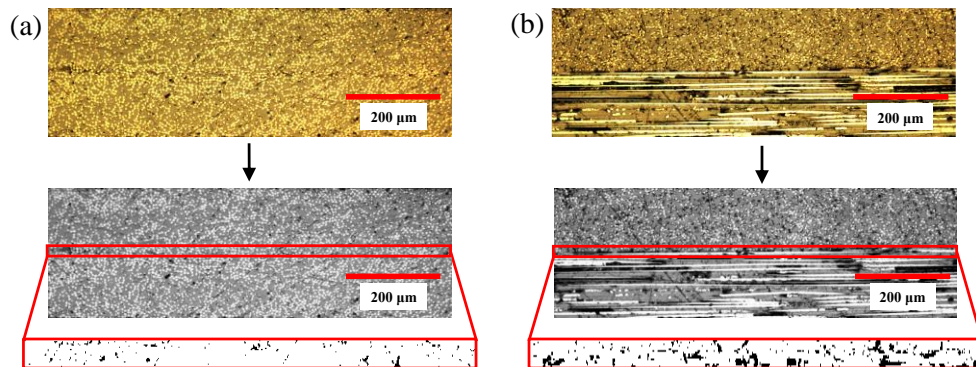


Figure 21. Microscopy images with grayscale representations, emphasizing the intimate contact region, facilitating the experimental degree of intimate contact measurement at the tape-substrate with (a) $[0^\circ/0^\circ]$ interface of Sample #2 and (b) $[90^\circ/0^\circ]$ interface of Sample #6.

3.5. T-peel Test and Interlaminar Bonding Strength Characterization

In this study, the T-peel test is used to quantify the interlaminar bonding strength and to validate the results of the degree of bonding model. While some researchers have used the Short Beam Strength (SBS) test to measure bonding strength [88], this method has inherent limitations. In particular, the SBS test requires the fabrication of multilayered

samples, making it challenging to accurately predict fracture initiation layers and fracture patterns during testing. Moreover, it becomes difficult to evaluate the bonding strength of individual interfaces between plies with varying fiber orientations using the SBS test. Conversely, the T-peel test enables the measurement of bonding strength in single interfaces. The testing procedure with $[0^\circ/0^\circ]$ lamination involves the fixation of pre-cracked samples with two peeling arms into the tension apparatus. Conducting T-peel test on $[90^\circ/0^\circ]$ lamination requires special attention to ensure that delamination damage should propagate along the $[0^\circ]$ and $[90^\circ]$ plies interfaces. In this study, it is ensured that all tested samples with $[90^\circ/0^\circ]$ stacking sequence have consistent delamination progressing at this interface, indicating the reliability of our experimental results.

Figure 22 (a) depicts a T-peel test conducted using an Instron universal tension machine equipped with a 100 KN load cell, following the ASTM D413 standard. The experimental degree of bonding ($D_{b,exp}$) is calculated from the peel force per unit width of the samples from T-peel test using the following equation:

$$D_{b,exp} = \frac{(PF)_{LAFP_{avg}}}{(PF)_{AC_{avg}}} \quad (3.3)$$

where $(PF)_{LAFP_{avg}}$ represents the average peel force per unit width of the LAFP fabricated samples without any post-processing (LAFP consolidation only), and $(PF)_{AC_{avg}}$ corresponds to the average peel force per unit width of Sample #2 with autoclave post-processing.

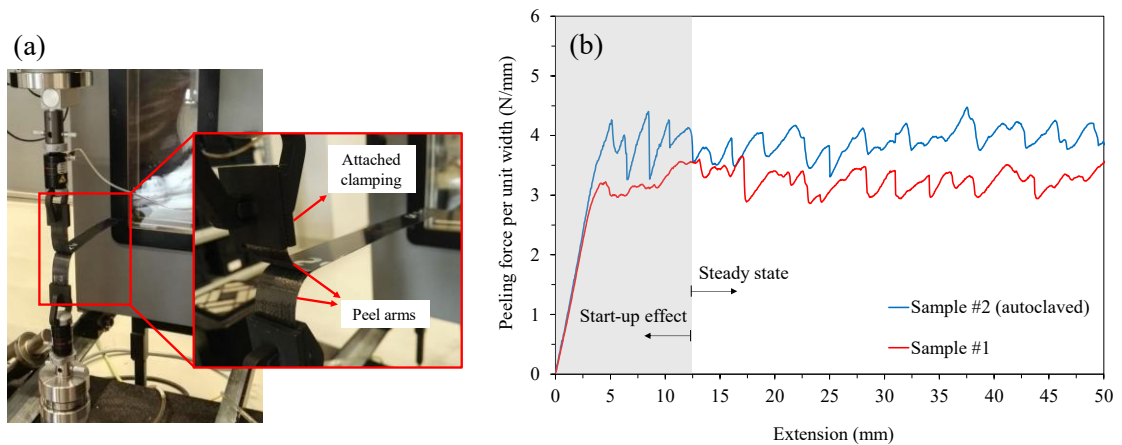


Figure 22. T-peel test (a) experimental setup and (b) peeling force per unit width vs. extension for Sample #2 (autoclaved) and Sample #1.

Figure 22 (b) illustrates the relationship between the peel force per unit width and the extension length for two cases, namely, Sample #2 (autoclaved) and Sample #1. From the graph in Figure 22 (b), a start-up effect is observable up to an extension length of 12.5 mm. Thus, the average peel force $(PF)_{avg}$ in Equation (3.3) for each sample is determined from the segment of the graph corresponding to a steady-state peeling force. Specifically, for the reference sample subjected to autoclave post-processing, an average peel force per unit width, $(PF)_{AC_{avg}}$, is measured to be 3.91 N/mm. Additionally, to ascertain the principal failure mode during the T-peel test, scanning electron microscopy (SEM) is employed to analyze the fracture surfaces of the samples. This analysis aids in gaining insights into the characteristics of bond failure.

3.6. Interlaminar Bonding Model

In the context of the LAFP process, interlaminar bonding involves two key mechanisms: firstly, the creation of intimate contact between adjacent surfaces, and secondly, the subsequent healing process that takes place within these contact regions. To assess the effectiveness of interlaminar bonding between two successive layers, the analysis starts by using degree of intimate contact and healing models for obtaining quantitative values for these two phenomena. The data calculated from the intimate contact model is used in the thermal model which provides an input to healing model. The results of intimate contact and healing models are then combined to accurately predict the degree of bonding.

3.6.1. Mantell and Springer Degree of Intimate Contact Model

The Mantell and Springer (MS) intimate contact model [76], which is based on squeeze flow approach and approximates surface profile with uniform rectangles, is as follows:

$$[D_{ic}(t)]_{MS} = \frac{1}{1 + \frac{w_0}{b_0}} \left[1 + 5 \left(1 + \frac{w_0}{b_0} \right) \left(\frac{a_0}{b_0} \right)^2 \int_0^{t_c} \frac{P_{app}}{\mu(T)} dt \right]^{\frac{1}{5}} \quad (3.4)$$

where w_0 , b_0 , and a_0 correspond to the geometric features of the incoming tape (Figure 23), and $\mu(T)$ represent temperature-dependent viscosity of the thermoplastic resin

system. It should be stated that, P_{app} is determined through using pressure-sensitive Fujifilm films (as detailed in Section 3.3). The calculation of a_0/b_0 and w_0/b_0 involves measuring the surface profile of the raw tape within an $800 \mu\text{m}$ by $800 \mu\text{m}$ square area using the μsurf laser profilometer from nanofocus® [30, 44]. This calculation leads to 2.54 and 1.55 values for a_0/b_0 and w_0/b_0 , respectively. Since the MS model only considers the new incoming tape, the substrate (all previously placed layers) is assumed to have a smooth surface, as illustrated in Figure 23 [27, 43] since it has been already subjected to laser heating and roller compaction in the placement of previous layup. However, it is important to note that this assumption may introduce inaccuracies in the MS model, as it overlooks significant phenomena arising from fiber orientation, such as fiber nesting and fiber-fiber contact. Furthermore, t_c is the consolidation time which can be calculated using the following relationship [76];

$$t_c = \frac{L_c}{v} \quad (3.5)$$

where v is the placement speed of LAFP. Additionally, the temperature-dependent viscosity, $\mu(T)$, given in Equation (3.6) is defined for CF/PEKK composite material as follows [90];

$$\mu(T) = 4.362 \times 10^7 e^{-0.0401(T-623)} \text{ Pa}\cdot\text{s} \quad (3.6)$$

where T is the temperature distribution at the interface.

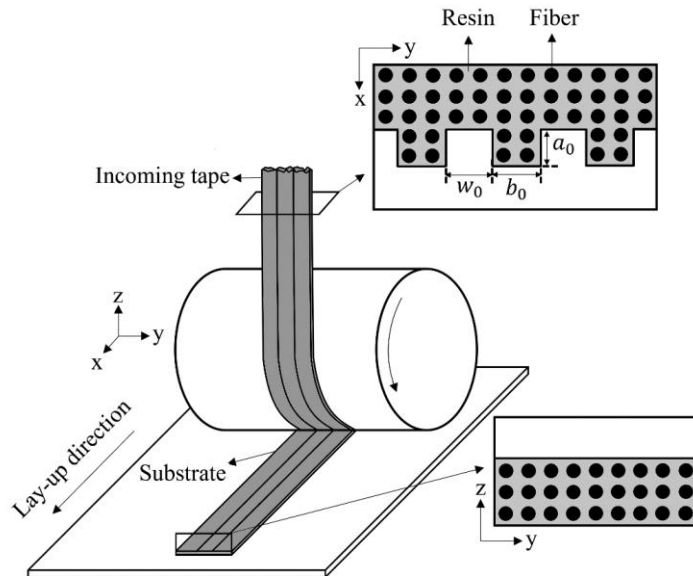


Figure 23. Illustration of the geometric features of the incoming tape and the idealized contact surface of the substrate.

To precisely predict the temperature distribution at the interface between the incoming tape and the substrate, the MATLAB-based thermal model developed in Chapter 2 is used. This model solves a two-dimensional heat transfer equation, incorporating a convective term to account for the fiber placement speed, a heat source term for laser heat flux, and appropriate boundary conditions, all based on finite difference discretization. In this thermal model, the thermal contact resistance (R_c) at the tape-substrate interface is calculated using the equation proposed by Levy et al [31], as described in Chapter 2 (Equation (2.2)).

3.7. Degree of Healing Model

In this study, the degree of healing in LAFP lamination under non-isothermal condition is obtained through the following equation proposed by Yang and Pitchumani's [72] as below:

$$D_h(t) = \left[\int_0^t \frac{1}{t_w(T)} dt \right]^{\frac{1}{4}} \quad (3.7)$$

where D_h is the degree of healing, t is the time at which healing could occur, and t_w represents the welding time of the polymer, which denotes the time required to achieve the maximum interfacial strength under an isothermal condition. The welding time, t_w , presented by Yan and Pitchumani [72] is adopted in this study is as follows:

$$t_w = A \exp \left[\frac{E}{R} \left(\frac{1}{T} - \frac{1}{T_{ref}} \right) \right] \quad (3.8)$$

with the model coefficients for CF/PEKK prepreg as $A = 4624s$, $E = 10^5 kJ/kmol$, $R = 8.314 kJ/kmol.K$, $T_{ref} = 643K$ [72] and T is interface temperature between tape and substrate which is obtained through the thermal model.

The degree of healing is dependent on the temperature profile and time of healing. Notably, research by Stokes-Griffin and Compston [69] delved into the bonding of CF/PEEK plies in the AFP process, highlighting that healing can transpire even at temperatures as low as the glass transition temperature (T_g). Thus, exclusively considering healing above the resin melting temperature might underestimate the degree

of healing. To address this, our study integrates this insight by accounting for the period that the temperature is above T_g during the consolidation and cooling phases of LAFP layup by utilizing the thermal model. Therefore, in our calculations for the degree of healing, we have considered a minimum temperature for healing as the T_g , which is 160°C for CF/PEKK material [87]. This approach ensures a more accurate assessment of healing phenomena, especially throughout the cooling process and its consequential impact on degree of bonding.

3.8. Degree of Bonding Model

Degree of bonding (D_b) for the thermoplastic AFP lay-up process refers to the quantitative measure of the inter-laminar bond strength between adjacent layers of thermoplastic composite material, indicating the effectiveness of the bonding achieved through intimate contact and healing. The inter-laminar bond strength, represented by the degree of bonding (D_b), is mathematically formulated as the product of the degree of intimate contact (D_{ic}) and the degree of healing (D_h), as expressed in Equation (3.9).

$$D_b = D_{ic}D_h \quad (3.9)$$

3.9. Results and Discussion

3.9.1. Experimental Degree of Intimate Contact

To ascertain the experimental degree of intimate contact ($D_{ic,exp}$) between the incoming tape and substrate, the methodology outlined in Section 3.4 is employed. The average values of $D_{ic,exp}$ for the samples manufactured at different fiber orientations, placement speed and consolidation force listed in Table 5 are graphically depicted in Figure 24. In the figure, the associated standard deviation values, obtained from four repetitions of each sample, are also provided. The obtained results are organized based on normalized fiber orientation and process parameters, as presented in Table 6, with additional experimental

intimate contact values (Sample #9 to Sample #15) from Chapter 2, which are marked with an asterisk, (*). The difference in interface fiber orientation for successive layers is normalized by 90° , the placement speed is normalized by 400 mm/s, and the consolidation force is normalized by 1000 N. These normalized parameters are denoted as $\hat{\theta}$, \hat{v} and \hat{F} , for normalized fiber orientation, placement speed and consolidation force, respectively. Specifically, $\hat{\theta}$ takes values of 0, 0.5, and 1, corresponding to $[0^\circ/0^\circ]$, $[45^\circ/0^\circ]$, and $[90^\circ/0^\circ]$ laminations, respectively.

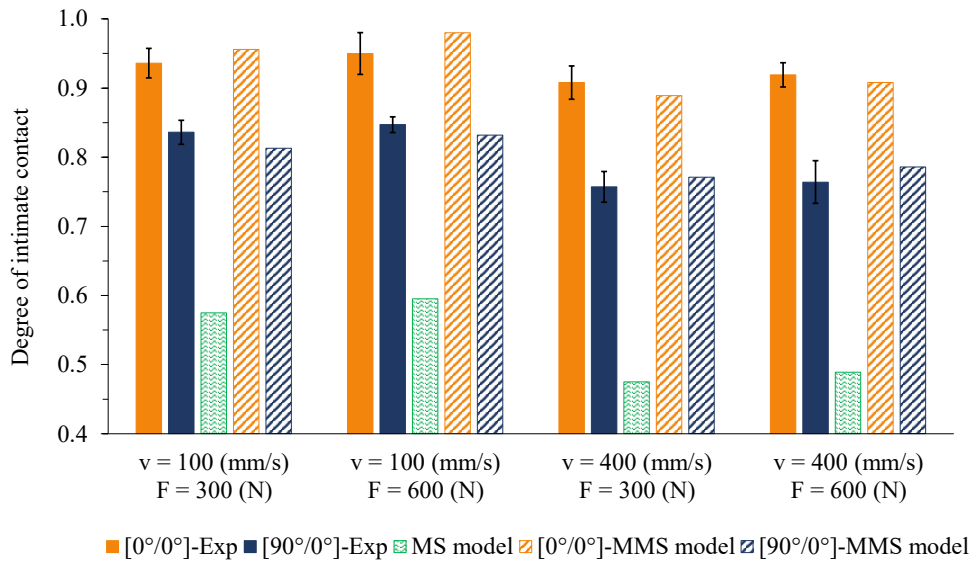


Figure 24. Comparison of experimental degree of intimate contact for laminates manufactured using different processes with degree of intimate contact obtained from Mantell and Springer (MS) and Modified Mantell and Springer (MMS) models.

As shown in Figure 24, the $[0^\circ/0^\circ]$ stacking sequences exhibit a higher degree of intimate contact values than $[90^\circ/0^\circ]$ interfaces for all process parameters. This distinction can be attributed to two primary phenomena: higher fiber nesting within the $[0^\circ/0^\circ]$ interface and lower fiber bed permeability to resin flow within the $[90^\circ/0^\circ]$ interface, as discussed in Chapter 2. Moreover, for both fiber orientations, a decrease in the degree of intimate contact values is observed because of increasing placement speed and reducing the consolidation force. The former can be elucidated by the shorter consolidation period that ensues due to higher placement speeds, leading to insufficient time for attaining full intimate contact between the incoming tape and the upper surface of the substrate. The latter phenomenon can be attributed to the reduction in the contact area arising from lower consolidation forces, thereby causing a decreased degree of intimate contact. Furthermore, Figure 24 suggests that the influence of placement speed on the degree of intimate contact is more pronounced than that of consolidation force. Consequently,

across both implemented consolidation forces, decreasing the placement speed from 400 mm/s to 100 mm/s yields a more substantial enhancement in the degree of intimate contact than elevating the roller consolidation force from 300 N to 600 N.

Table 6. Degree of intimate contact values from experiment, Mantell and Springer (MS) and Modified Mantell and Springer (MMS) with respect to normalized AFP process parameters.

Sample No.	$\hat{\theta}$	\hat{v}	\hat{F}	$D_{ic,exp}$	$D_{ic,MS}$	CF_{exp}	CF_{LR}	$D_{ic,MMS}$	Abs. Err. (%)
#1	0	0.25	0.3	0.936	0.575	1.628	1.662	0.956	2.11
#2	0	0.25	0.6	0.950	0.595	1.597	1.648	0.98	3.19
#3	0	1	0.3	0.908	0.475	1.912	1.872	0.889	2.07
#4	0	1	0.6	0.919	0.489	1.879	1.857	0.908	1.17
#5	1	0.25	0.3	0.836	0.575	1.454	1.413	0.813	2.81
#6	1	0.25	0.6	0.847	0.595	1.424	1.398	0.832	1.76
#7	1	1	0.3	0.757	0.475	1.594	1.623	0.771	1.83
#8	1	1	0.6	0.764	0.489	1.562	1.608	0.786	2.94
#9	0	0.25	0.5	0.946*	0.589	1.606	1.652	0.973	2.88
#10	0	0.25	1	1.000*	0.608	1.645	1.628	0.99	1.02
#11	0	1	0.5	0.917*	0.486	1.887	1.862	0.905	1.3
#12	0.5	0.25	0.5	0.912*	0.589	1.548	1.528	0.9	1.33
#13	0.5	1	0.5	0.862*	0.486	1.774	1.738	0.845	2.03
#14	1	0.25	0.5	0.843*	0.589	1.431	1.403	0.827	1.95
#15	1	1	0.5	0.761*	0.486	1.566	1.613	0.784	3.02

* Experimental intimate contact values (Sample #9 to Sample #15) obtained from Chapter 2.

3.9.2. Temperature Profile

For various AFP layup scenarios detailed in Table 6, the thermal model described in Chapter 2 is utilized to derive temperature distributions. These distributions are then employed to calculate the degree of intimate contact according to the MS model ($D_{ic,MS}$), as well as the degree of healing (D_h) following the procedure given in Figure 25. To illustrate the influence of incomplete in-situ intimate contact ($D_{ic} < 1$) on the temperature distribution at the tape-substrate interface, Figure 26 presents two different temperature profiles during AFP lay-up. The first case imitates an ideal scenario with complete intimate contact ($D_{ic} = 1$) whereas the second one mirrors an experimental instance with $D_{ic,exp} = 0.936$ with the process conditions of $v = 100$ mm/s and $F = 300$ N (Sample

#1). In the scenario of complete intimate contact, the absence of interlaminar thermal contact resistance promotes heat transfer across the contacting plies without the thermal contact resistance. Conversely, for the experimental case, thermal contact resistance, calculated using Equation (2.2), is incorporated into the thermal model. A comparative analysis of the two temperature profiles reveals that for an incomplete intimate contact between the substrate and tape (blue line), temperature values are lower beyond the shadowing region in comparison to scenarios featuring full intimate contact (red line). This difference can be explained by the fact that when the temperature of the tape exceeds that of the substrate, in the case of full intimate contact, heat can easily flow from the tape to the substrate without encountering thermal contact resistance, resulting in a higher interface temperature.

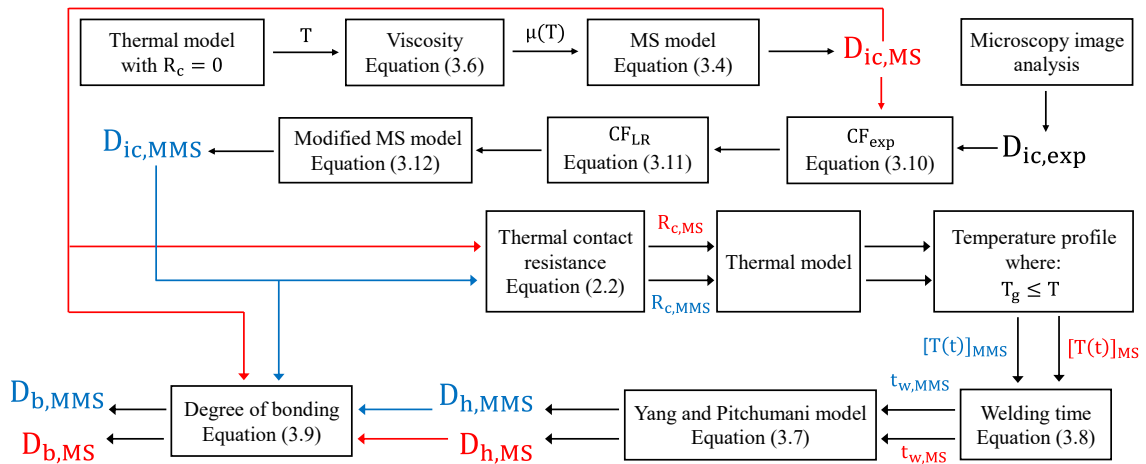


Figure 25. Flow chart illustrating the calculations of degree of intimate contact, degree of healing and degree of bonding using MS and MMS models.

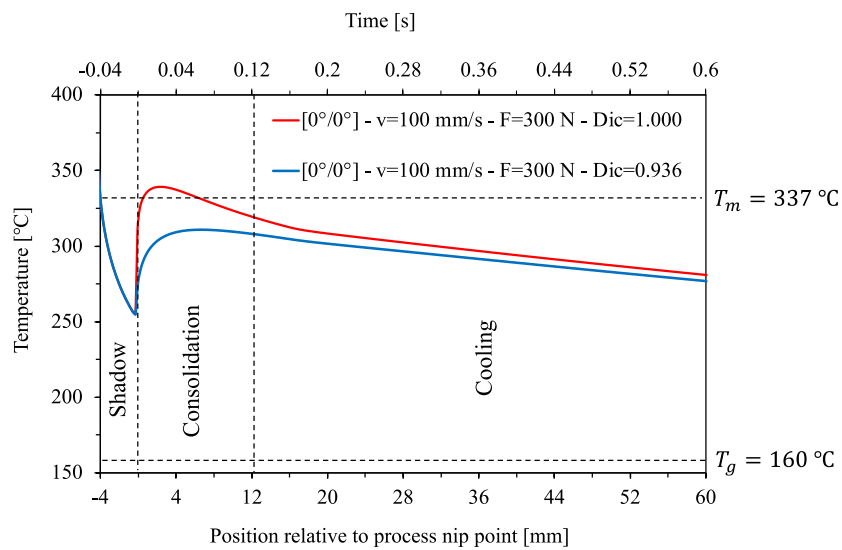


Figure 26. Temperature profiles during AFP lay-up for Sample #1 at $[0^\circ/0^\circ]$ interface with full ($D_{ic} = 1$) and partial degree of intimate contact ($D_{ic,exp} = 0.936$).

Notably, the temperature profile beyond the shadowing region plays a crucial role in determining both the degree of intimate contact, as defined by Equation (3.4), and the degree of healing, as expressed by Equation (3.7). The change in fiber orientation between adjacent plies introduces distinct interlaminar thermal contact resistance (R_c), thereby influencing the interface temperature and consequently affecting the values of both D_{ic} and D_h . Moreover, the incorporation of the glass transition temperature (T_g) profile aids in identifying the appropriate time interval for assessing the degree of healing (D_h).

3.9.3. Degree of Intimate Contact from Mantell and Springer (MS) and Introduction of Modified Mantell and Springer (MMS) Model

In this study, to assess the degree of intimate contact, the initial step involves employing the Mantell and Springer (MS) intimate contact model in accordance with the procedure outlined in Figure 25, resulting in $D_{ic,MS}$. The computed $D_{ic,MS}$ values are graphically depicted in Figure 24 and compiled in Table 6. The evident trend is that the MS model consistently yields significantly lower predictions of the degree of intimate contact compared to the experimental findings for all cases. This discrepancy can be owing to the model's exclusive focus on squeeze flow as the primary mechanism for generating intimate contact, while neglecting the influential percolation flow within the fiber bed – a parameter vital to resin flow [32], [41]. Furthermore, the MS model's predictions yield identical outcomes for both $[0^\circ/0^\circ]$ and $[90^\circ/0^\circ]$ interfaces. This difference can be attributed to variations in fiber orientation between successive plies, giving rise to various phenomena. Firstly, as for $[0^\circ/0^\circ]$ lamination, the phenomenon of fiber nesting causes the development of inter-laminar intimate contact. This occurs because the fibers share the same direction, enabling the upper layer fibers to interlace between the lower layer fibers and vice versa [40]. Secondly, the anisotropic permeability behavior of the composite fiber bed influences the interface. Notably, permeability is enhanced when the flow aligns with the fiber axes (0° -aligned fibers). Consequently, the change in fiber orientation at the interface – particularly pronounced in $[90^\circ/0^\circ]$ cases – decreases the permeability of the interface fiber bed for resin [51], leading to a drop in resin-resin contact and a hindered bonding process within the inter-laminar region. A third important factor is the fiber-fiber contact, which is prominent in $[90^\circ/0^\circ]$ lamination. As the orientation difference between successive layers deviates from unidirectionality, the nesting effect diminishes while the

influence of fiber-fiber contact prevails. Essentially, the applied force is embraced mainly by contacting fibers and thus resin does not experience enough pressure, leading to weak intimate contact level [91].

To integrate the above discussed phenomena into the MS model and thereby enhance its accuracy, a correction factor based on experimental findings (CF_{exp}) is introduced for all samples, which are tabulated in Table 6. The correction factor is of the form:

$$CF_{exp}(\hat{\theta}, \hat{v}, \hat{F}) = \frac{D_{ic,exp}(\hat{\theta}, \hat{v}, \hat{F})}{D_{ic,MS}(\hat{\theta}, \hat{v}, \hat{F})} \quad (3.10)$$

To correlate normalized process parameters and the set of CF_{exp} value listed in Table 6, a linear regression model is implemented utilizing MATLAB software. The linear regression model entails a comprehensive examination of a dataset encompassing normalized process parameters and their corresponding CF_{exp} values. The obtained correlation is presented as follows:

$$CF_{LR}(\hat{\theta}, \hat{v}, \hat{F}) = 1.6068 - 0.24908\hat{\theta} + 0.27979\hat{v} - 0.048724\hat{F} \quad (3.11)$$

where CF_{LR} represents the correction factor function obtained through linear regression. The statistical significance of the coefficients is evaluated through p-values. Notably, all predictor variables ($\hat{\theta}, \hat{v}, \hat{F}$) exhibited strong statistical significance ($p < 0.05$), signifying their substantial influence on CF_{LR} . However, the largest coefficient for normalized parameters in Equation (3.11) corresponds to \hat{v} , confirming the findings of Figure 24, which indicate that velocity is the most influential parameter in the intimate contact development process. The model's goodness-of-fit measures indicate a well-fitted nature. The root mean squared error (RMSE) is calculated as 0.0414, implying a minimal average discrepancy between the observed and predicted values generated by the model with R^2 value of 0.948. The correction factors for each sample are calculated using the CF_{LR} function listed in Table 6. Then, using CF_{LR} function as a multiplier to the MS model, a modified Mantell and Springer (MMS) degree of intimate contact model is defined as follows:

$$D_{ic,MMS} = (1.6068 - 0.24908\hat{\theta} + 0.27979\hat{v} - 0.048724\hat{F}) \times \frac{1}{1 + \frac{w_0}{b_0}} \left[1 + 5 \left(1 + \frac{w_0}{b_0} \right) \left(\frac{a_0}{b_0} \right)^2 \int_0^{t_c} \frac{P_{app}}{\mu(T)} dt \right]^{\frac{1}{5}} \quad (3.12)$$

Using the Equation (3.12), $D_{ic,MMS}$ values are evaluated and presented in Figure 24 and tabulated in Table 6. Furthermore, the absolute value of the error (Abs error) between $D_{ic,MMS}$ and $D_{ic,exp}$ which is calculated as $Abs.Error = |(D_{ic,MMS} - D_{ic,exp})/D_{ic,exp}| \times 100$ are reported in Table 6. It is important to highlight that the error values for all cases are below 3.2%. Thus, the MMS model effectively captures the behaviors of $D_{ic,exp}$ concerning changes in fiber orientation, placement speed, and consolidation force.

Additionally, to further evaluate the accuracy of the $D_{ic,MMS}$ model, the experimental degree of intimate contact data from a study conducted by Celik et al. [36] is utilized. The study involves the use of CF/PEEK composite material, which has similar characteristics to CF/PEKK [92]. Figure 27 and Table 7 presents the process parameters of the LAFP process employed by Celik et al. [36] to produce $[0^\circ/0^\circ]$ interfaces, along with their reported experimental degree of intimate contact. The corresponding temperature profiles for each case are estimated using the thermal model described in Chapter 2, which are subsequently validated by the thermal profiles provided by Celik et al. [36]. Notably, the roller specifications employed in Celik et al.'s study closely resemble those in the present investigation, facilitating the utilization of Equation (3.1) and (3.2) for the contact length and calculation of pressure, respectively. Once the temperature profiles are obtained, the Mantell and Springer (MS) model is applied to calculate the degree of intimate contact, $D_{ic,MS}$. In the MS model, the geometric parameters a_0/b_0 and w_0/b_0 for CF/PEEK are reported in the study of Celik et al. [36] as 1.75 and 1.288, respectively. The viscosity of the CF/PEEK composite is determined using the matrix-fiber equation provided by another study [76]. By applying Equation (3.12), the $D_{ic,MMS}$ values are determined for each case. The absolute error calculated between the experimental and MMS model values, as illustrated in Figure 27, highlights accuracy of Equation (3.12) in estimating the degree of intimate contact values. This validation underscores the reliability and applicability of the modified model in capturing the intricacies of the intimate contact phenomenon.

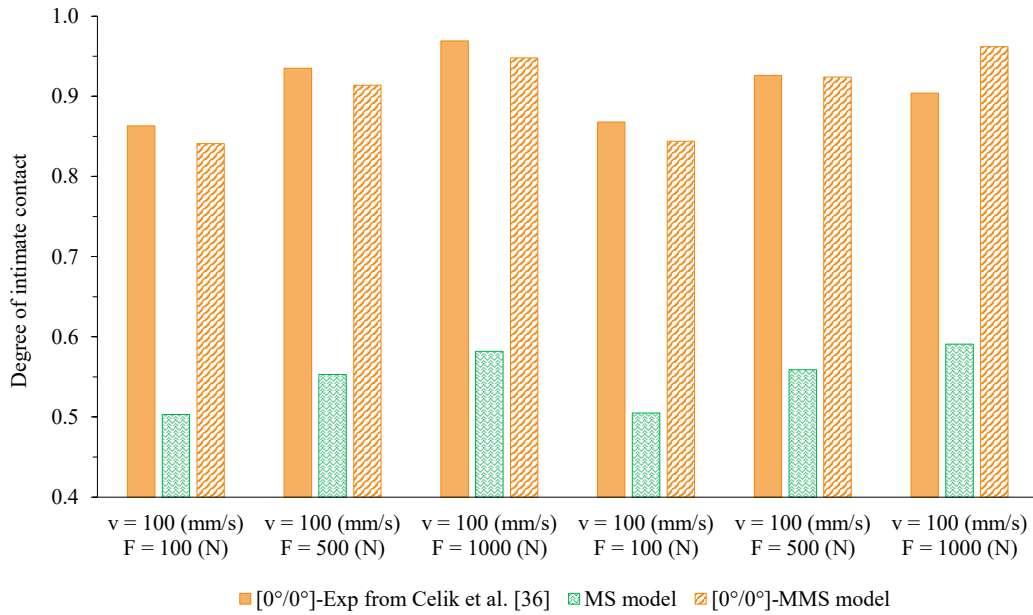


Figure 27. Comparison of experimental degree of intimate contact reported by Celik et al. [36] with degree of intimate contact obtained from Mantell and Springer (MS) and Modified Mantell and Springer (MMS) models.

Table 7. Experimental data from Celik et al. [36] and simulation results validating the accuracy of the proposed CF_{LR} formula.

$\hat{\theta}$	\hat{v}	\hat{F}	$D_{ic,exp}^*$	$D_{ic,MS}$	$D_{ic,MMS}$	Abs. Err. (%)
0	0.25	0.1	0.863	0.503	0.841	2.55
0	0.25	0.5	0.935	0.553	0.914	2.27
0	0.25	1	0.969	0.582	0.948	2.21
0	0.25	0.1	0.868	0.505	0.844	2.73
0	0.25	0.5	0.926	0.559	0.924	0.25
0	0.25	1	0.904	0.591	0.962	6.43

* Experimental data of Celik et al. [36].

3.9.4. Degree of Healing

Referring to Equation (3.7) and (3.8), it should be recalled that the degree of healing (D_h) is contingent on temperature and welding time. Employing the previously established thermal model, temperature distribution at the interface of the incoming tape and substrate is computed. The flowchart for calculating the degree of healing is depicted in Figure 25. For both the MS and MMS models, the corresponding degree of intimate contact values

are used to calculate interlaminar thermal contact resistance via Equation (2.2). The thermal model provides insights into both the temperature distribution and the duration for which the temperature exceeds the glass transition temperature (T_g). Figure 28 yields the results of D_h for $[0^\circ/0^\circ]$ and $[90^\circ/0^\circ]$ orientations, using both MS and MMS models. As can be understood from the figure, when employing the MS intimate contact model, the degree of healing appears nearly identical for both fiber orientations. This outcome stems from the identical calculation of D_{ic} using the MS model. However, upon refining the MS model with the CF_{LR} coefficient, the results change, leading to distinctive D_h values for two fiber orientations. Notably, in the $[0^\circ/0^\circ]$ case where there is a higher degree of intimate contact at the interface and thus a reduced thermal contact resistance, heat can be easily transferred from the tape to the substrate. This, in turn, yields higher temperatures and consequently, a higher degree of healing. Furthermore, due to the temperature and welding time dependency of the degree of healing, the velocity parameter exerts a more dominant influence on D_h values in comparison to the consolidation force. Lower velocity values result in higher degrees of healing according to the MMS model. This arises from the fact that lower layup velocities subject the laminate to extended periods of thermal exposure, thereby enhancing polymer healing through diffusion. This prolonged exposure culminates in a heightened degree of healing [85].

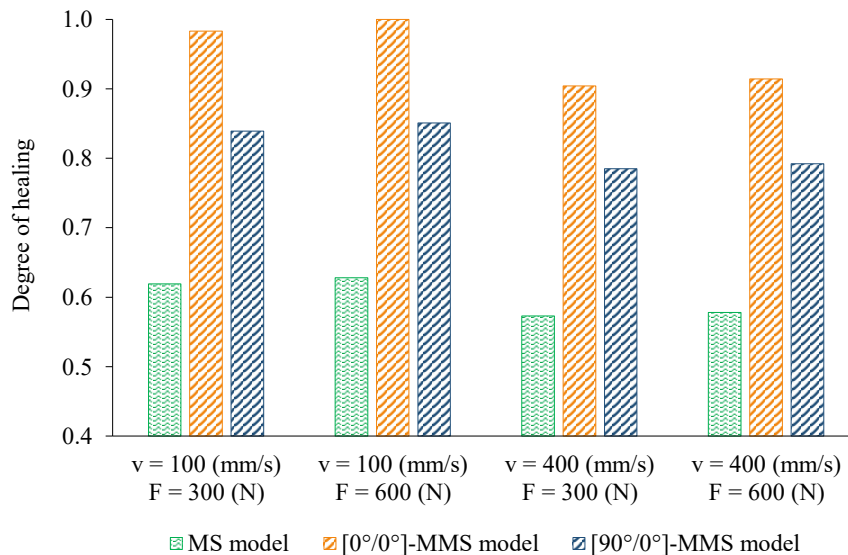


Figure 28. Degree of healing results for different process parameters and fiber orientations with intimate contact values derived from MS and MMS models.

3.9.5. Degree of Bonding

In this study, the assessment of the experimental degree of bonding ($D_{b,exp}$) is carried out through the utilization of the T-peel test (see Section 3.5). The outcomes depicting $D_{b,exp}$ values for various fabricated samples (as outlined in Table 5) are displayed in Figure 29. It is worth noting that the laminates with $[0^\circ/0^\circ]$ fiber orientations exhibit notably higher interlaminar bonding strength in comparison to $[90^\circ/0^\circ]$ stacking sequence. Furthermore, the observed trend reveals that an increase in placement speed (resulting in reduced laser exposure and consolidation time) or a reduction in consolidation force leads to a decrease in the $D_{b,exp}$ for both types of laminates. Significantly, the influence of placement speed seems to be more pronounced compared to that of the consolidation force.

To unravel the underlying failure mechanisms within the inter-laminar interfaces of samples featuring varying lamination process parameters and orientations, a scanning electron microscopy (SEM) analysis is conducted on the fracture surfaces resulting from the T-peel tests. The SEM images presented in Figure 30 show damaged surfaces as a result of T-peel tests. SEM analysis is performed on samples with two specific sets of process parameters: those yielding the highest bond strength ($v=100$ mm/s and $F=600$ N) (Figure 30 (a) and (b)) and the lowest bond strength ($v=400$ mm/s and $F=300$ N) (Figure 30 (c) and (d)) for each of the two different fiber orientations. An in-depth examination of the SEM images provides valuable insights. Notably, for the $[0^\circ/0^\circ]$ orientation, discernible plastic deformation within the thermoplastic matrix becomes apparent (Figure 30 (a) and (c)), particularly evident under the conditions of $v=100$ mm/s and $F=600$ N (Figure 30 (a)). This serves as evidence of robust inter-laminar bonding strength. Conversely, in the $[90^\circ/0^\circ]$ orientation, a significant portion of the interface fibers remain devoid of any resin-induced plastic deformation (Figure 30 (b) and (d)) where regions like sections-A exhibit a distinct lack of inter-laminar bonding. These sections underscore the absence of intimate contact in the interface. A closer examination reveals that only specific areas with traces of $[90^\circ]$ fibers exhibit large plastic deformations, implying weak bonding interface due to partial degree of intimate contact. This difference can be attributed to the localized nature of the healing process, which solely transpires in regions of intimate contact. Consequently, areas that exhibit substantial plastic deformations correspond to the initial contact points marked by heightened levels of healing, while the remaining interface is more prone to fracture. Furthermore, the SEM images unveil a

consistent pattern: for both fiber orientations, when employing lower placement speeds and higher consolidation pressures, the entire bonded interface shows extensive plastic deformation. This observation underlines a heightened degree of healing across the entire interface.

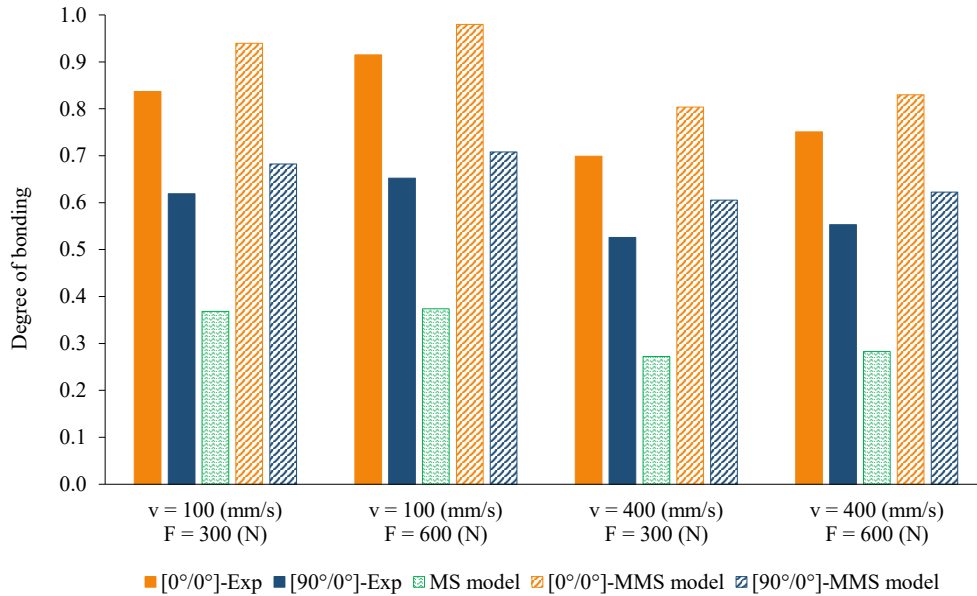


Figure 29. Comparison of experimental degree of bonding for laminates manufactured using different processes with a degree of bonding obtained with the incorporation of Mantell and Springer (MS) and Modified Mantell and Springer (MMS) models.

The degree of bonding is calculated for both MS and MMS models following the procedure given in Figure 25 based on the already computed the degree of intimate contact and healing where $D_{b,MS}$ and $D_{b,MMS}$ stand for degree of bonding values for MS and MMS model, respectively. Figure 29 reveals a clear disparity between the predictions of the MS model and the corresponding experimental values, with the MS model consistently underestimating the degree of bonding. This difference is primarily attributed to the inadequacy of the MS model in accurately predicting both the degree of intimate contact (as discussed in Section 3.9.3) and subsequently, the degree of healing (as outlined in Section 3.9.4). Furthermore, given that MS model does not consider fiber orientation in its formulation, the obtained results for identical set of process parameters are expectedly the same for different fiber orientations. It is important to note the MS model can capture the experimentally observed trend such that the increase in placement speed or reduction in the consolidation force leads to a decrease in the degree of bonding.

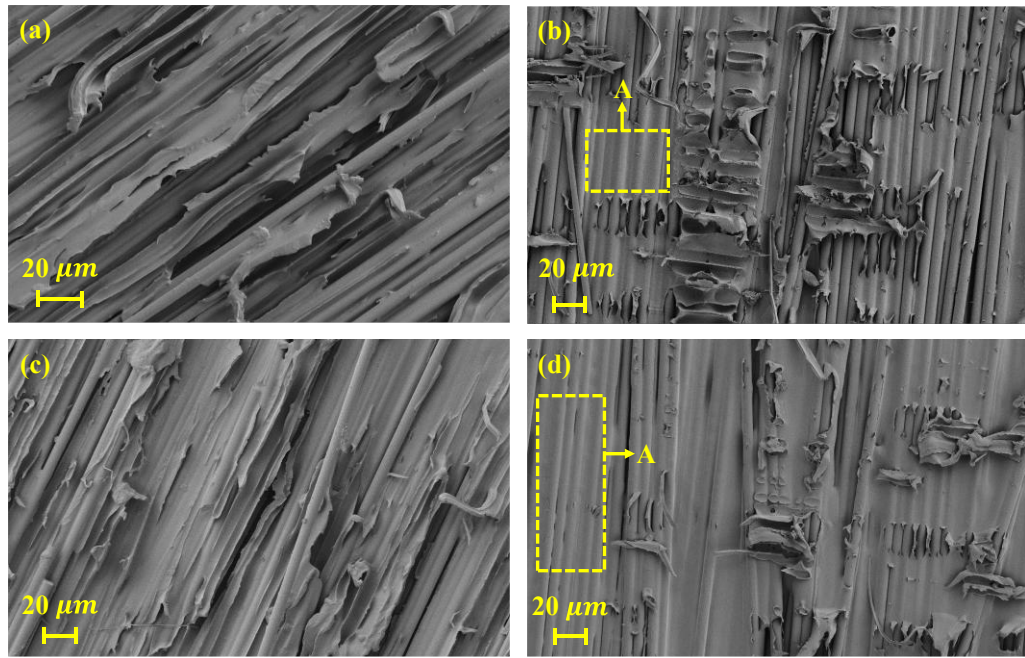


Figure 30. Representative SEM images of the typical fracture surfaces observed in T-peel test specimens for process parameters of 100 mm/s and 600 N (a) Sample #2 at $[0^\circ/0^\circ]$ interface and (b) Sample #6 at $[90^\circ/0^\circ]$ interface, and for process parameters of 400 mm/s and 300 N (c) Sample #3 at $[0^\circ/0^\circ]$ interface, and (d) Sample #7 at $[90^\circ/0^\circ]$ interface.

On the other hand, the usage of MMS model significantly enhances the accuracy of the predicted degree of bonding, achieving closer agreement with the experimental results (Figure 29). Specifically, since the MMS model takes ply orientation into account in calculating degree of intimate contact and healing, it yields accurate results for the degree of bonding as well, which is in alignment with the outcomes of all T-peel test performed on laminates with different stacking sequences. Figure 29 indicates that $[0^\circ/0^\circ]$ laminates show higher degree of bonding (equivalently, higher bonding strength) than $[90^\circ/0^\circ]$ which is in alignment with the SEM analysis such that the specimens with higher degree of bonding undergoes larger plastic deformation which is apparent from the fracture surface. Among the LAFP process parameters studied, lower placement speed and higher consolidation force result in higher interlaminar bonding predictions. Same as the degree of intimate contact, low speed and high force provide sufficient consolidation and heat for the development of high degree of intimate contact and healing. In passing, it should be again noted that the placement speed is the most dominant parameter for the degree of bonding.

The results presented in Figure 29 are also tabulated in Table 8, by the inclusion of absolute errors for $D_{b,MS}$ and $D_{b,MMS}$ with reference to $D_{b,exp}$, respectively. The

maximum absolute errors for the degree of bonding between MS model-based predictions and T-peel test results are 62.36% for the $[0^\circ/0^\circ]$ and 48.88% for the $[90^\circ/0^\circ]$ laminates. In contrast, the difference between the results of the MMS based model and T-peel test is drastically reduced to 4.97% for the $[0^\circ/0^\circ]$ and 15.06% for the $[90^\circ/0^\circ]$ laminates.

Table 8. Degree of bonding values obtained from the experiment (T-peel test), Mantell and Springer (MS), and Modified Mantell and Springer (MMS) methods, relative to normalized AFP process parameters.

Sample No.	$\hat{\theta}$	$\hat{\nu}$	\hat{F}	$D_{b,exp}$	$D_{b,MS}$	$D_{b,MMS}$	Abs. Err. (%) -MS	Abs. Err. (%) -MMS
#1	0	0.25	0.3	0.837	0.368	0.940	56.00	12.28
#2	0	0.25	0.6	0.915	0.374	0.980	59.16	7.10
#3	0	1	0.3	0.699	0.272	0.804	61.06	14.97
#4	0	1	0.6	0.751	0.283	0.830	62.36	10.51
#5	1	0.25	0.3	0.619	0.368	0.682	40.50	10.19
#6	1	0.25	0.6	0.652	0.374	0.708	42.69	8.59
#7	1	1	0.3	0.526	0.272	0.605	48.25	15.06
#8	1	1	0.6	0.553	0.283	0.623	48.88	12.56

3.10. Summary

In conclusion, this study has tackled the sophisticated challenge of predicting inter-laminar bonding strength in thermoplastic materials, specifically CF/PEKK, manufactured with Laser-Assisted Automated Fiber Placement (LAFP) processes. The novel approach of the Modified Mantell and Springer (MMS) model for the degree of intimate contact surpasses the capabilities of the traditional Mantell and Springer (MS) model. By integrating a correction factor (CF_{LR}) rooted in empirical data, the MMS model effectively bridges the gap between predictive simulations and experimental results, significantly enhancing the accuracy of degree of bonding predictions.

The study's findings underline the comprehensive nature of bonding strength in thermoplastic LAFP processes. Process parameters, such as placement speed and

consolidation force, hold the key to achieving optimal bonding quality. Lower placement speeds and higher consolidation forces not only contribute to a higher degree of healing but also facilitate the development of greater intimate contact between layers. Additionally, the MMS model successfully captures the impact of fiber orientation for the degree of bonding calculation through improved degree of intimate contact and degree of healing results. The distinct behavior of different fiber orientations, specifically $[0^\circ/0^\circ]$ and $[90^\circ/0]$, has been highlighted, with the former consistently displaying better bonding strength owing to enhanced fiber nesting and resin permeability.

The validation process, conducted through T-peel tests, explicitly confirms the precision of the MMS model in projecting the degree of bonding outcomes for the degree of intimate contact. Manufacturers can leverage this improved model to make informed decisions, optimize manufacturing processes, enhance product quality, and support structural integrity in the future applications of LAFP. Ultimately, this study significantly advances our understanding of inter-laminar bonding strength in thermoplastic LAFP. By correcting the limitations of existing models, the MMS model emerges as a more accurate tool for guiding AFP manufacturing processes, contributing to continuous innovation and excellence in composite manufacturing practices.

CHAPTER 4: MULTI-SCALE PERMEABILITY CHARACTERIZATION OF COMPOSITES FABRICATED VIA LASER-ASSISTED FIBER PLACEMENT: A COMPARATIVE ANALYSIS OF PULSE-DECAY AND MICROCT TECHNIQUES

In this chapter, the permeability of thermoplastic composites manufactured using Laser-Assisted Fiber Placement (LAFP) was evaluated through a dual-scale methodology: the pulse-decay technique at the macro-scale and micro-CT analysis at the micro scale. Permeability, a crucial factor in Out-of-Autoclave (OoA) processes, governs air evacuation and void reduction, thereby directly influencing the quality of the final composite material. Laminates with varying fiber orientations and lay-up velocities were fabricated and analyzed to investigate the interplay between process parameters, void formation, and permeability.

Both the pulse-decay method and micro-CT analysis consistently revealed that increased lay-up velocities and greater variation in fiber orientations resulted in higher permeability, primarily due to enhanced void connectivity. A comparative evaluation showed strong agreement between the two techniques, highlighting their suitability as complementary approaches for permeability characterization. These insights provide valuable guidelines for optimizing LAFP process parameters to achieve high-quality, in-situ consolidated thermoplastic composites, with significant implications for advanced aerospace and automotive applications.

4.1. Introduction

Automated Fiber Placement (AFP) is an advanced manufacturing process widely used for fabricating composite materials with high precision and efficiency. AFP involves the use

of a robotic system that deposits pre-impregnated composite tapes (slit tapes) layer by layer along designated paths. This method offers significant advantages, such as material savings, reduced labor costs, enhanced repeatability, and suitability for complex geometries. Given these benefits, AFP has become essential in industries like aerospace, automotive, and energy, where lightweight, durable, and high-performance components are required [13].

Traditionally, thermoset composites have been used in AFP processes due to their ease of processing and high mechanical strength. However, thermosets require long curing cycles, have limited shelf lives, and their brittle nature makes them prone to crack propagation. To address these drawbacks, the focus has shifted towards thermoplastic composites, such as CF/PEKK (carbon fiber/polyetherketoneketone) and CF/PEEK (carbon fiber/polyetheretherketone) [11]. Thermoplastics offer superior fracture toughness, resistance to chemicals, and recyclability, along with shorter processing times due to their ability to consolidate under heat and pressure during layup. These advantages make thermoplastics increasingly popular in high performance applications, particularly for next-generation aerospace components that require high tolerance to service conditions [93].

However, the AFP process for thermoplastic composites presents unique challenges. Due to the high viscosity of thermoplastic resins at processing temperatures, achieving proper consolidation between layers is difficult, which can result in voids forming during lay-up. Achieving intimate contact between layers requires careful control of parameters such as compaction force, laser heating, and lay-up speed [14].

Voids in AFP-fabricated composites can be categorized into two main types: intra-laminar voids and inter-laminar voids. Intra-laminar voids arise from defects within the tape material, such as air bubbles trapped in the resin or fibers during tape manufacturing. Inter-laminar voids occur between layers during lay-up, often due to insufficient compaction force, inadequate heating, or poor fiber alignment. Key factors influencing void formation include lay-up speed, compaction force, heat flux, and fiber orientation [32].

Several studies have explored the effect of AFP parameters on part quality. Chen et al. [94] studied how layup speed affects part quality in AFP processes, focusing on fiber steering and cut-restart quality. Their research found that higher layup speeds can lead to

defects due to inadequate heat transfer, while slower speeds improve heat distribution and consolidation, enhancing part quality. This highlights the importance of optimizing layup speed to ensure high-quality AFP-manufactured composites in industries like aerospace and automotive. Baho et al. [95] investigated how laser-assisted heat flux affects part quality in AFP processes for thermoplastic composites. Their research focused on the distribution of laser heating and its impact on temperature control and uniform heating projections. The study found that precise control of heat flux parameters is essential for achieving uniform consolidation and high-quality parts, highlighting the critical role of temperature management in AFP processes for aeronautic and aerospace applications. Mathew and Joshi [96] studied how roller pressure affects the tensile and flexural properties of carbon fiber reinforced laminates fabricated using AFP. Their research found that higher roller pressures improve the consolidation quality and mechanical properties of the laminates, while lower pressures can lead to defects and reduced part quality. This study highlights the importance of optimizing roller pressure to achieve high-quality AFP-manufactured composite parts. Zanjani et al. [97] investigated the effect of fiber orientation in the AFP process on part quality. Their study focused on how different fiber orientations impact the formability and mechanical properties of self-reinforced polypropylene (SRPP) composites. The research highlighted that specific fiber orientations can significantly enhance structural integrity and reduce defect formation, thereby improving the overall quality of AFP-manufactured parts. Xia et al. [98] studied how nip point temperature and layup velocity affect part quality in AFP processes. Their research utilized numerical simulations to predict the ideal nip point temperature for complex geometries, emphasizing the importance of uniform heat distribution and precise control of layup velocity to optimize part properties. Venkatesan et al. [99] studied how various AFP process parameters affect void content in polyamide-6 carbon fiber prepreg laminates. Their research found that parameters such as temperature, pressure, and layup speed significantly influence void formation, highlighting the importance of optimizing these parameters to achieve high-quality composite parts. Maurer et al. [100] performed a parametric study to explore how lay-up velocity and laser heating settings affect the quality of final components. They identified process windows for the laser's axis position, angle, power, and lay-up speed. The study found that increasing the lay-up velocity reduces the cooling time beneath the roller, with insufficient cooling from both the roller and the surrounding environment, leading to deconsolidation and poor-quality final parts. Moreover, in Chapter 2 the effect of fiber orientation on temperature history during laser-

assisted thermoplastic fiber placement (LAFP) was studied. The results showed that larger differences in fiber orientation between layers reduce intimate contact, increase thermal resistance, and lower cooling rates, affecting laminate crystallinity.

After the AFP process, to ensure structural integrity it is essential to remove or reduce voids during or after the lay-up process. Traditionally, autoclave processing has been used, where composite parts are subjected to high pressure and temperature within a sealed environment to achieve complete consolidation and minimize voids. Although effective, autoclave processing has significant drawbacks, including high capital investment, long processing times, and size limitations due to the dimensions of the autoclave chamber [101]. As an alternative, Out-of-Autoclave (OoA) methods, such as vacuum bagging, have gained popularity. OoA processes offer greater flexibility, lower operational costs, and the ability to process larger parts [102]. However, for OoA methods to be effective, the presence of connected voids and sufficient air permeability is crucial to allow air evacuation during the vacuum cycle. Without adequate permeability, isolated voids may remain trapped within the structure, compromising the quality of the final component [103].

Permeability is thus a critical property in composite manufacturing, especially for OoA processes. It measures the ease with which air or fluids flow through the void network within the laminate. High permeability facilitates air evacuation, enabling effective consolidation, while low permeability increases the risk of isolated voids that degrade mechanical performance. As autoclave processing is expensive and operationally intensive, understanding and controlling permeability is essential for developing reliable OoA strategies.

Several studies have explored permeability in AFP-fabricated composites. Aziz et al. [104] studied the transverse permeability of dry fiber preforms made via AFP. They combined experiments with computational modeling to examine how variations in gap sizes between fibers affect permeability. Using ANSYS simulations and X-CT imaging, they showed that even small deviations in gap size can impact permeability by a factor of five. Their results emphasize the need for precise tape placement to optimize resin flow and mechanical performance in AFP-manufactured composites. Cender et al. [105] studied gas evacuation in partially saturated woven fiber laminates using the pulse-decay method. They found that as resin saturation increases, permeability decreases, limiting gas flow. Their work offers valuable insights for improving vacuum-based composite

manufacturing processes. Zhang et al. [91], [106] conducted experimental studies on the interlayer air permeability of CF/PEEK thermoplastics before and after vacuum bag processing. Their findings highlight that air permeability is influenced by the fiber orientation between adjacent layers. They observed that off-axis laminate configurations promote fiber-to-fiber contact, which helps maintain interlayer air permeability across various temperatures and vacuum hold times.

This chapter investigates the permeability of composites fabricated via Laser-Assisted Fiber Placement (LAFP) using two complementary methods: the pulse-decay method at the macro-scale and micro-CT analysis at the micro scale. A key contribution of this work lies in comparing macro and micro permeability for samples with three different fiber orientations, offering new insights into how fiber architecture influences void formation and air evacuation. This dual-scale analysis bridges the gap between microstructural features and practical permeability performance, guiding the optimization of LAFP parameters for improved quality in Out-of-Autoclave (OoA) processes.

4.2. Materials and Experimental Methods

The methodology employed in this study comprises two main stages: composite manufacturing and permeability analysis. To provide an overview of the workflow, a flowchart summarizing the key steps is presented in Figure 31.

Figure 31 outlines the composite manufacturing process using Laser-Assisted Fiber Placement (LAFP) and the subsequent permeability analysis through two complementary techniques: pulse-decay and micro-CT. The manufacturing stage begins with fabricating laminates using three stacking sequences ($[0^\circ/0^\circ/0^\circ]$, $[0^\circ/45^\circ/0^\circ]$, and $[0^\circ/90^\circ/0^\circ]$) under varying placement speeds (100 mm/s and 400 mm/s) and a constant compaction force (500 N). Following this, permeability analysis involves two pathways: the pulse-decay method, which includes experimental testing and post-processing in MATLAB to calculate permeability over porosity, and micro-CT analysis, which involves 3D reconstruction, porosity analysis, and permeability calculations using pore geometry. This flowchart serves as a roadmap, linking the experimental workflow to the research objectives and offering a clear structure to the methodology.

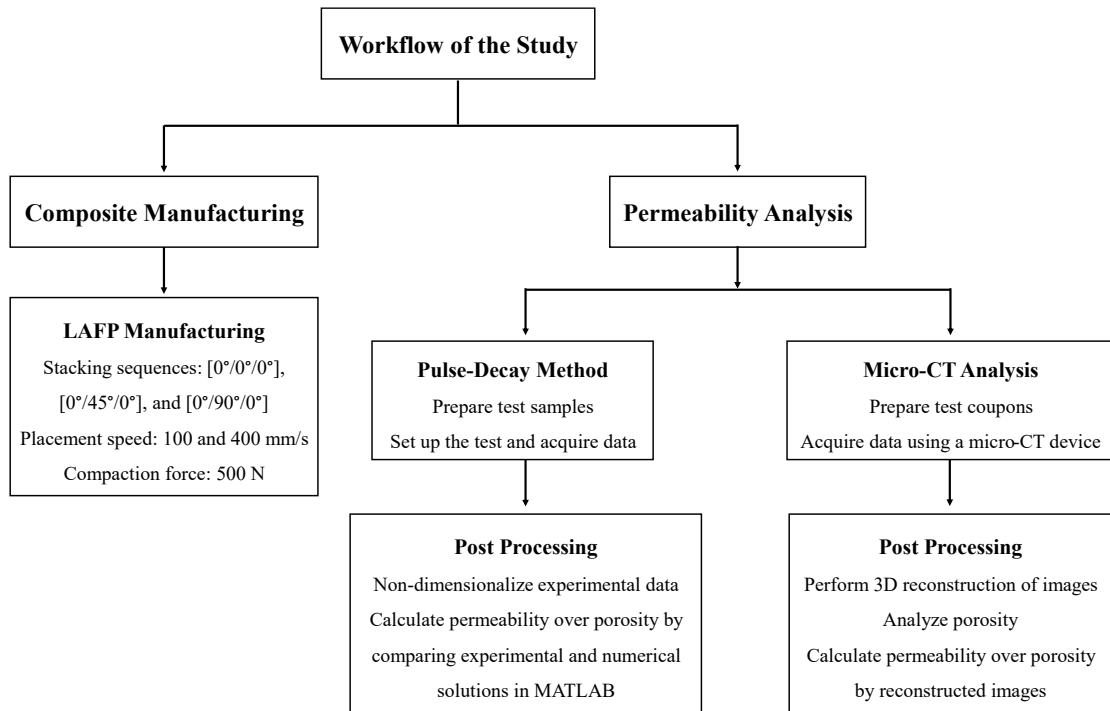


Figure 31. Workflow of the study showing the steps involved in composite manufacturing using LAFP and permeability analysis through pulse-decay and micro-CT methods.

The LAFP machine used in this study features a fiber placement head that can lay up to eight 6.35 mm wide tapes at once, with a maximum nominal lay-up speed of 800 mm/s. It includes a 6 kW Laserline LDF series diode laser with an optic lens that has a 250 mm focal distance, creating a rectangular laser spot measuring 8 mm × 56 mm. The machine is equipped with a conformable compaction roller that has a shore hardness of 60 and a diameter of 70 mm, with a maximum compaction force of 1000 N. This setup helps in-situ compaction and consolidation between layers. For successful lamination, the tool temperature is set at 155°C, close to the glass transition temperature of PEKK. Tool temperature control is managed by four electrical heater units under the tool and monitored by four thermocouples at the corners, validated with a thermal camera on the LAFP head. Furthermore, during the manufacturing of laminates, the laser power is adjusted according to different layup speeds to maintain a consistent visible nip point temperature.

In this study, the LAFP machine laminates three layers of thermoplastic slit tapes from Toray Cetex, marked as TC1320 CF/PEKK. These tapes have a fiber volume fraction of 66%, a thickness of 0.15 mm, and a width of 6.35 mm. The sample manufacturing employs three different stacking sequences: [0°/0°/0°], [0°/45°/0°], and [0°/90°/0°],

forming laminates each 1100 mm long and 50.8 mm wide. The lay-up process uses specific parameters for placement speed, consolidation force, and fiber orientation, with laser power settings detailed in Table 9.

Initially, all samples intended for processing and permeability characterization, originally 1100 mm in length, were reduced to 900 mm by cutting 100 mm from each end. This step was taken to exclude areas with significant fluctuations in process parameters, which occur at the beginning and end of the LAFP layup process. The cutting was executed using a Kuka KR16 Ultra F robot equipped with a high-performance water jet pump. Subsequently, three coupons, each measuring 10 mm × 10 mm, were extracted from the midline of the 900 mm length at positions of 350, 450, and 550 mm, using the same water jet cutting system for micro-CT permeability analysis.

Table 9. LAFP placement trial parameters for the fabrication of the samples.

Sample No.	Laminate stacking sequence	Placement speed (mm/s)	Consolidation force (N)	Corresponding laser power (W)
1	[0°/0°/0°]	100	500	1386
2	[0°/45°/0°]	100	500	1386
3	[0°/90°/0°]	100	500	1386
4	[0°/0°/0°]	400	500	3427
5	[0°/45°/0°]	400	500	3427
6	[0°/90°/0°]	400	500	3427

4.2.1. Air Permeability Assessment with Pulse-Decay Method

The air permeability of the samples post-AFP lay-up was assessed using the pulse-decay method. This technique involves applying a vacuum to one end of the sample while a pressure transducer at the opposite end measures the pressure decay from atmospheric pressure. A schematic and experimental setup for the pulse-decay gas flow characterization is depicted in Figure 32. The pressure transducer is directly connected to one end of the sample. To ensure that the gas flow is restricted to the sample's pores, silicone grease is used as a sealant between the upper surface of the samples and the vacuum bag, as well as between the bottom and top surfaces of the samples. The presence of bubbles in the sealant grease on the top surface was noted during test preparation. These bubbles were monitored at the beginning and end of the tests to check for air leaks on both the top and bottom surfaces, as well as through the thickness of the samples. The

bubbles maintained fixed shapes and locations throughout the experiments, indicating effective sealing. Tacky tapes were strategically placed along the sample edges to ensure complete sealing. A laboratory vacuum line with an absolute pressure of 0.07 bar was connected to the experimental setup to maintain a vacuum during testing. A GEM 3500 compact low-pressure OEM pressure transmitter was employed to measure the absolute pressure at the other end of the samples. Additional tacky tape was used to seal the setup connection of the pressure transducer to block any air influx. Once the setup was complete and the vacuum applied, the pressure transducer began recording pressure decay at a rate of 110 data per second using the LabView program. This recording continued for 24 hours for each sample. All measurements were taken at room temperature, 25°C, under the assumption that the PEKK material would retain its pore structures and porosity due to its non-viscous behavior at this temperature.

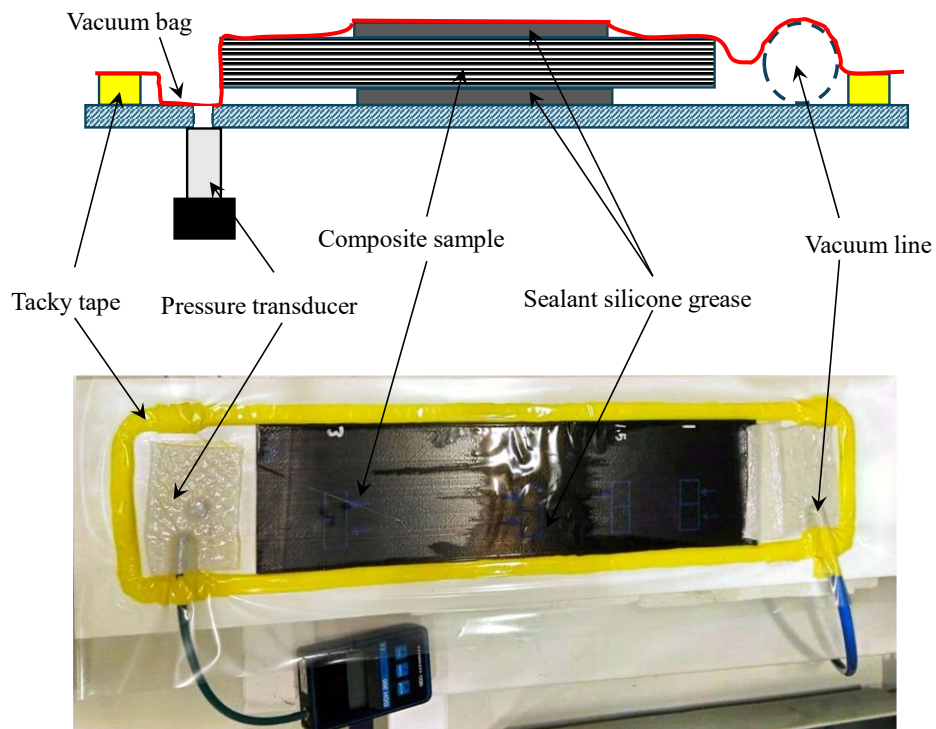


Figure 32. Schematic (top) and experimental setup (bottom) of pulse-decay gas flow characterization.

Following the measurement of pressure decay values in LAFP-fabricated in situ consolidated samples, the mathematical methodology proposed by Cender et al. [105] is applied to compute air permeability. This approach begins by solving the compressible continuity equation within porous media, which considers the volume-averaged Darcy's velocity and adheres to the ideal gas law. Subsequently, the primary equation undergoes nondimensionalization using the equations below, where L is the sample's length, P_i denotes the initial atmospheric pressure, and P_f represents the final vacuum pressure and $\Delta P = P_i - P_f$.

$$\hat{x} = \frac{x}{L}, \hat{P} = \frac{P - P_f}{\Delta P}, \hat{t} = \frac{t}{t_c} \quad (4.1)$$

where t_c is the characteristic time and defined to normalize time:

$$t_c = \frac{\emptyset \mu L^2}{K_i \Delta P} \quad (4.2)$$

In this context, \emptyset represents the effective porosity, defined as the volume of connected voids allowing airflow, μ is the air's viscosity, and K_i is the intrinsic liquid permeability. These parameters contribute to the dimensionless formulation of the governing partial differential equation (PDE). The PDE is then numerically solved using finite difference discretization, as below:

$$\frac{\partial \hat{P}}{\partial \hat{t}} = \frac{\partial}{\partial \hat{x}} \left((\hat{P} + \hat{P}_s) \frac{\partial \hat{P}}{\partial \hat{x}} \right) \quad (4.3)$$

where

$$\hat{P}_s = \frac{P_f + b}{\Delta P} \quad (4.4)$$

It is a dimensionless pseudo-pressure introduced in [107] to describe the system, where the value of \hat{P}_s determines the shape of the pressure decay function, and b is the Klinkenberg parameter.

Determining \hat{P}_s and t_c allows for the calculation of the Klinkenberg parameter, b , and the ratio of liquid permeability to porosity, K_i/\emptyset , as outlined in Equations (4.4) and (4.2) respectively. The variable t_c is used to scale the experimental pressure decay data, and \hat{P}_s influences the shape of the pressure decay curve necessary for numerical solutions. The numerical solution of Equation (4.3) is achieved through a forward finite differencing approach, executed in MATLAB. For each sample, the relevant experimental data is interpolated and continuously compared against the numerically resolved pressure decay data until the residual sum of squares (RRSQ) reaches a minimum. When alignment

between experimental and numerical curves is attained for a sample, the respective values for \widehat{P}_s and t_c are determined. These diagrams facilitate the calculation of \widehat{P}_s using numerical data and t_c using experimental data. The Klinkenberg parameter, b , which is expressed in pressure units, exclusively depends on the effective pore diameter; a smaller b value indicates a larger pore diameter. Additionally, a correlation factor, $1 + \frac{b}{P_f}$, is introduced to relate the gas permeability (K_g) to the liquid permeability (K_l), as below:

$$K_g = K_l \left(1 + \frac{b}{P_f} \right) \quad (4.5)$$

By dividing both sides of Equation (4.5) by effective porosity (\emptyset), the gas permeability normalized by porosity (K_g/\emptyset) for each sample is calculated.

4.2.2. X-ray Micro Computed Tomography

X-ray computed tomography (XCT) is a non-destructive imaging technique that produces three-dimensional (3D) volumes, enabling detailed examination of a specimen's internal structures at the micro scale. A typical XCT setup for capturing X-ray projections consists of four main components: an X-ray source, a detector, a stage for securing the test sample, and an operating system with data storage capabilities. These components are schematically illustrated in Figure 33. Widely used in materials science, XCT systems often employ cone-beam geometry with micro focus or nano-focus X-ray sources and high-resolution flat-panel detectors [108], [109], [110].

The principle of XCT relies on the attenuation of X-rays as they pass through materials, which is influenced by the material's density, atomic composition, and the beam's travel distance. By measuring attenuation, radiographic projections are generated, each representing a specific orientation of the sample. Multiple projections are acquired by incrementally rotating the specimen or the X-ray source and detector. These 2D projections are reconstructed into 3D volumes using algorithms like filtered back projection.

To enhance image quality, filters are employed to reduce noise and improve contrast. X-ray filters, placed in the beam path, adjust the wavelength distribution by absorbing lower-energy photons that scatter more and degrade image quality, resulting in cleaner, noise-reduced images. During scanning, the specimen is mounted on a rotary stage and imaged

from various angles. The reconstructed 3D dataset assigns each voxel a gray value corresponding to the material's X-ray attenuation coefficient, providing insights into density and composition.

Post-processing is performed using software like VGSTUDIO MAX, which offers advanced tools for visualization, segmentation, and quantitative analysis. This enables precise characterization of internal microstructures, such as the calculation of permeability based on pore geometry.

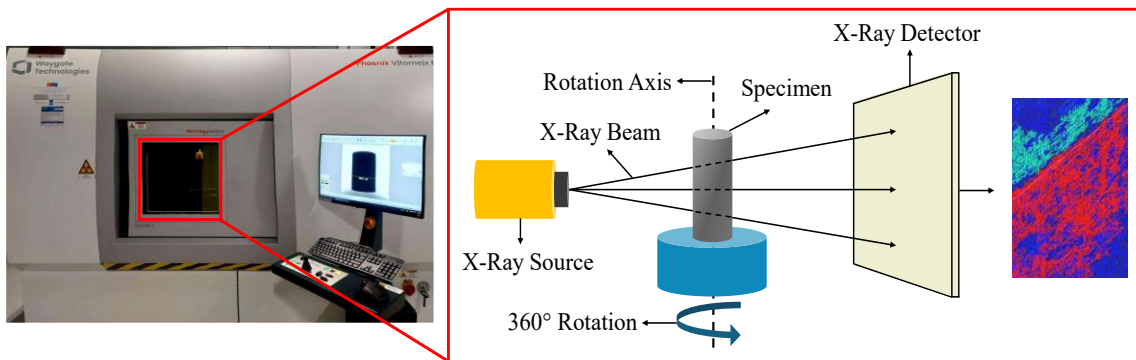


Figure 33. Working principle of a micro computed tomography system.

The samples were scanned with a Phoenix X-ray micro computed tomography (XCT) system. A 6 mm × 6 mm viewing area was chosen to ensure sufficient sample size for accurate porosity calculation. A spatial resolution of 8 μm per voxel was applied, with each voxel representing a volume of 8 × 8 × 8 μm³. Scanning and reconstruction for each sample took approximately 2 hours, and the 3D image stack was generated using Phoenix's proprietary software. The 3D reconstruction image for Sample #5 is presented in Figure 34 as a representative example.

To assess the porosity quantitatively, six equally spaced cross-sectional slices were extracted along the length of the LAFP layup. Each cross-section was analyzed with ImageJ to determine its porosity values, offering a detailed understanding of void distribution across the sample. Among these, the cross-section labeled A-B, which exhibited the lowest porosity, was selected for permeability calculations. The reason for selecting the cross-section with the lowest porosity stems from the critical role of interconnected voids in permeability. Voids are present along the entire length of the part; however, isolated voids do not contribute to fluid flow. A cross-section with lower porosity indicates a higher proportion of interconnected voids and fewer isolated ones, making it more representative of the pathways required for fluid transport. This makes it

the most representative region for accurately evaluating the material's permeability. By focusing on this section, the analysis ensures that the calculated permeability reflects the material's capacity for fluid flow through its interconnected void network.

In this selected cross-section, the total porosity area (the total red area of porosity shown in cross-section A-B in Figure 34) was treated as a circular flow channel, and the equivalent average pore radius, R_{eq} , was calculated. Permeability, K , was then estimated using Equation (4.6). This approach is based on the analogy between Darcy's law for porous media flow and the Hagen-Poiseuille equation for flow in cylindrical pipes, under the assumption of laminar flow with no-slip boundary conditions at the pore walls [111]. It serves as a reliable first-order approximation. This analogy has been thoroughly explored in the literature (e.g., Kozeny & Carman [112], [113]).

$$K = \frac{R_{eq}^2}{8} \quad (4.6)$$

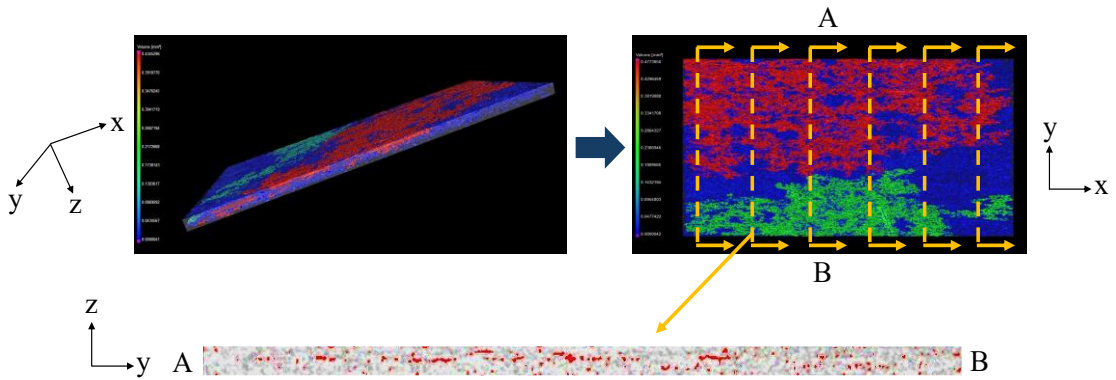


Figure 34. Cross-section A-B with lowest porosity from 3D micro-CT reconstruction for permeability analysis

4.3. Results and Discussion

4.3.1. Pulse-Decay Method Permeability Calculation

Figure 35 shows the pressure behavior recorded using the pulse-decay method for each stacking sequence at different fabricated lay-up velocities, offering valuable insights into the integrity and permeability characteristics of the samples. As can be seen, the $[0^\circ/0^\circ/0^\circ]$ stacking sequences, both at velocities of 100 mm/s and 400 mm/s, maintain a consistent pressure at 1 bar throughout the duration of the test, indicating a robust and impermeable

structure in the unidirectional (UD) layers. This uniformity suggests that under these lay-up conditions, the laminate is likely dense with minimal to no connected voids, which corroborates its potential suitability for high-strength applications where air permeability may be detrimental.

In contrast, the $[0^\circ/45^\circ/0^\circ]$ and $[0^\circ/90^\circ/0^\circ]$ stacking sequences exhibit notable pressure drops, highlighting differences in their structural porosity and void connectivity. For both angles, as the lay-up velocity increases from 100 mm/s to 400 mm/s, the pressure decay curves become steeper, particularly noticeable within the first few hours of the test. This quicker pressure decay at higher velocities suggests that the process speed leads to more pronounced void networks, facilitating air passage.

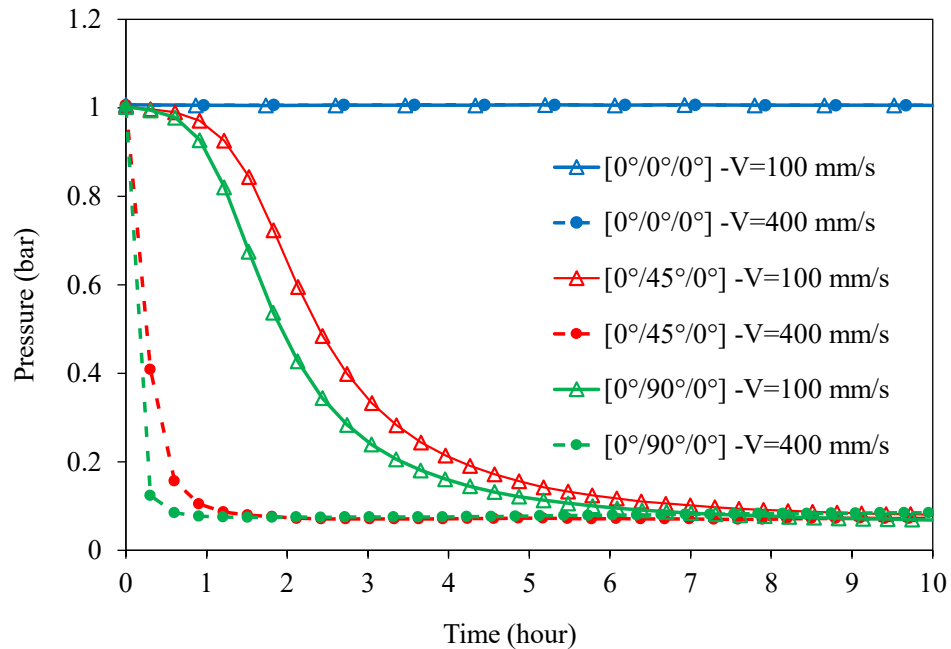


Figure 35. Pressure records from the pulse-decay method for different samples over time.

Moreover, while the $[0^\circ/45^\circ/0^\circ]$ and $[0^\circ/90^\circ/0^\circ]$ sequences show similar trends in pressure behavior, the extent of pressure drop and the rate at which it occurs could be indicative of how fiber orientation affects the formation of voids. The similar patterns between these orientations at corresponding speeds suggest that void formation is not solely dependent on the angle of fiber lay-up but also significantly influenced by the velocity at which the fibers are deposited.

These observations from the $[0^\circ/45^\circ/0^\circ]$ and $[0^\circ/90^\circ/0^\circ]$ sequences also point to potential variability in the mechanical properties and the quality of the laminate, as more

pronounced voids can compromise material strength and uniformity. Thus, adjusting the lay-up velocity could be a crucial parameter in optimizing the production process to balance between structural integrity and necessary permeability for specific applications. This analysis underscores the importance of closely monitoring and controlling lay-up conditions to achieve desired material characteristics and performance.

Figure 36 presents the non-dimensional pressure (\hat{P}) versus non-dimensional time (\hat{t}) curves for the $[0^\circ/45^\circ/0^\circ]$ and $[0^\circ/90^\circ/0^\circ]$ stacking sequences at lay-up velocities of 100 mm/s and 400 mm/s. These curves compare experimental data with numerical solutions derived from the governing partial differential equation, as described in Section 4.2.1. Since the unidirectional (UD) samples ($[0^\circ/0^\circ/0^\circ]$, Sample #1 and 4) did not exhibit any measurable pressure decay during the test period, they were excluded from the comparison.

The strong agreement observed between experimental and numerical curves for the $[0^\circ/45^\circ/0^\circ]$ and $[0^\circ/90^\circ/0^\circ]$ sequences demonstrate the validity of the procedure outlined in Section 4.2.1. By iteratively minimizing the residual sum of squares (RRSQ) between the experimental and numerical data, the characteristic time (t_c) and pseudo-pressure (\hat{P}_s) were determined. These parameters were then used to calculate the gas permeability normalized by porosity (K_g/ϕ), with the results summarized in Table 10.

Table 10 indicates that, for the same placement speed, the K_g/ϕ value for the $[0^\circ/90^\circ/0^\circ]$ stacking sequence is higher, and the Klinkenberg parameter b is lower compared to the $[0^\circ/45^\circ/0^\circ]$ sequence. This difference arises because increased fiber orientation results in more connected voids. Additionally, at the same fiber orientation, an increase in placement speed leads to an increase in K_g/ϕ and a decrease in b , due to insufficient consolidation pressure and heat flux.

It is noteworthy that the increase in K_g/ϕ from the $[0^\circ/45^\circ/0^\circ]$ to the $[0^\circ/90^\circ/0^\circ]$ stacking sequence at placement speeds of 100 mm/s and 400 mm/s is 22.26% and 36.21%, respectively. This indicates that, as placement speed rises, the impact of fiber orientation on K_g/ϕ becomes more significant due to the reduced time available for layer compaction.

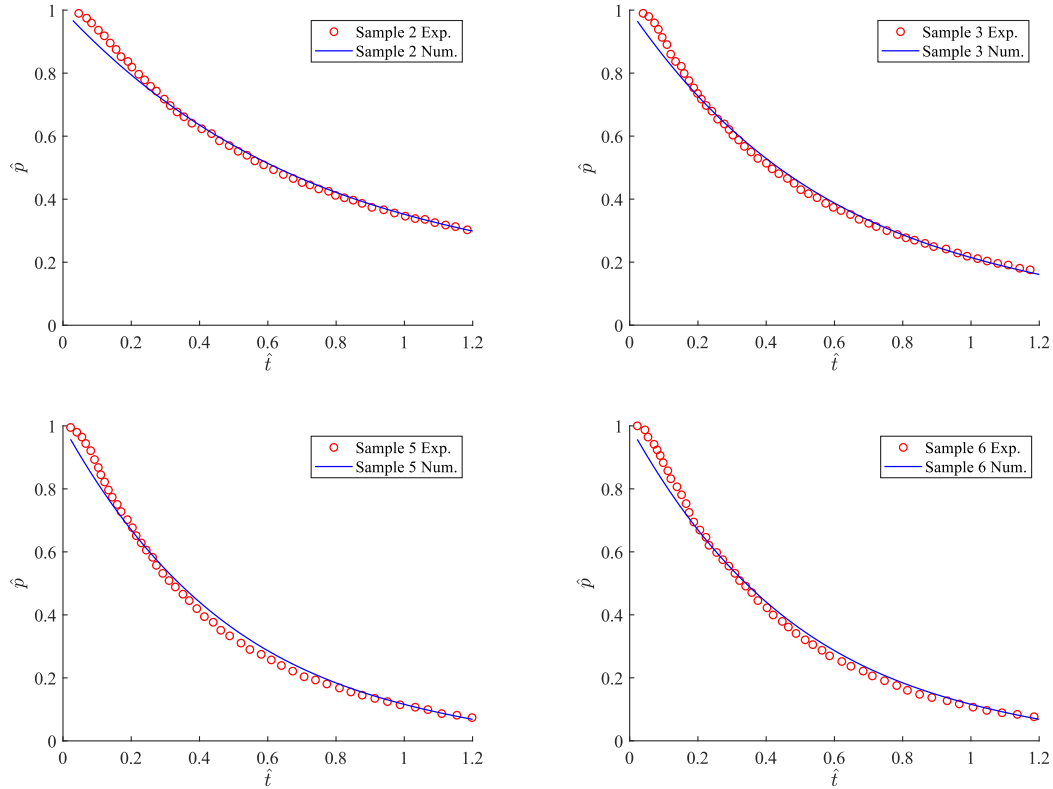


Figure 36. Numerical and experimental nondimensional pressure–time diagrams for in situ consolidated LAFP samples.

Table 10. Manufacturing and permeability characteristics of in situ consolidated LAFP samples.

Sample No.	Lay-up velocity (mm/s)	K_i/\emptyset (mm ²)	b (KPa)	K_g/\emptyset (mm ²)
1	100	-	-	-
2	100	7.51E-6	26.69	2.75E-5
3	100	1.04E-5	24.17	3.54E-5
4	400	-	-	-
5	400	1.66E-5	15.74	4.27E-5
6	400	3.02E-5	12.26	6.70E-5

Moreover, the difference in K_g/\emptyset value between the 100 mm/s and 400 mm/s placement speeds is 55.31% for the $[0^\circ/45^\circ/0^\circ]$ stacking sequence and 89.28% for the $[0^\circ/90^\circ/0^\circ]$ stacking sequence. This implies that the effect of increasing placement speed on K_g/\emptyset is more pronounced for higher fiber orientation differences, such as in the $[0^\circ/90^\circ/0^\circ]$ sequence.

4.3.2. Micro-CT Permeability Analysis

The images in Figure 37 depict the micro-CT scans of all samples. The voids are color-coded by their volume, providing a visual representation of the porosity variation throughout the sample. Cooler colors (e.g., blue) represent areas of the matrix or smaller voids, while warmer colors (e.g., red, yellow) indicate larger voids or regions with higher porosity.

The $[0^\circ/0^\circ/0^\circ]$ sequence (top row) demonstrates low void content, regardless of the layup velocity. At both 100 mm/s and 400 mm/s, the laminates maintain high quality, with minimal interconnected voids. This indicates that unidirectional stacking is less susceptible to void formation, even at higher layup speeds, likely due to the absence of intersecting fiber orientations. In contrast, the $[0^\circ/45^\circ/0^\circ]$ (middle row) and $[0^\circ/90^\circ/0^\circ]$ (bottom row) sequences show an increase in void content, particularly in the form of interconnected voids, when transitioning from unidirectional stacking ($[0^\circ/0^\circ/0^\circ]$) to oriented stacking. The introduction of off-axis and orthogonal plies creates more complex interfaces, leading to challenges in achieving complete consolidation and higher void interconnectivity. This effect is exacerbated at the higher layup velocity of 400 mm/s, where the rapid deposition reduces the time available for fiber compaction and matrix flow, further increasing the void content. Notably, the $[0^\circ/0^\circ/0^\circ]$ laminates at both 100 mm/s and 400 mm/s exhibit consistently good quality, with low void content and minimal void interconnectivity. This highlights the robustness of unidirectional stacking under varying LAFP parameters, while oriented stacking sequences are more sensitive to the interplay between layup velocity and consolidation quality. These findings underscore the importance of stacking sequence and layup velocity as key parameters in LAFP process optimization, with implications for achieving high-quality composite laminates with minimal defects.

For Sample #2 at 100 mm/s lay-up velocity, the equivalent radius was measured at 4.88E-03 mm, with a porosity of 0.12 and a permeability over porosity of 2.48E-5 mm². When the stacking sequence was changed to $[0^\circ/90^\circ/0^\circ]$ (Sample #3) at the same lay-up velocity, both the equivalent radius and porosity increased to 7.98E-03 mm and 0.21, respectively, with a corresponding increase in permeability over porosity to 3.79E-6 mm².

At the higher lay-up velocity of 400 mm/s, the Sample #5 demonstrated an equivalent radius of 8.16E-03 mm, a porosity of 0.18, and a permeability over porosity of 4.62E-5

mm². The stacking sequence of [0°/90°/0°] (Sample #6), showed further increases, with an equivalent radius of 1.15E-02 mm, a porosity of 0.28, and the highest permeability over porosity value observed at 5.93E-5 mm².

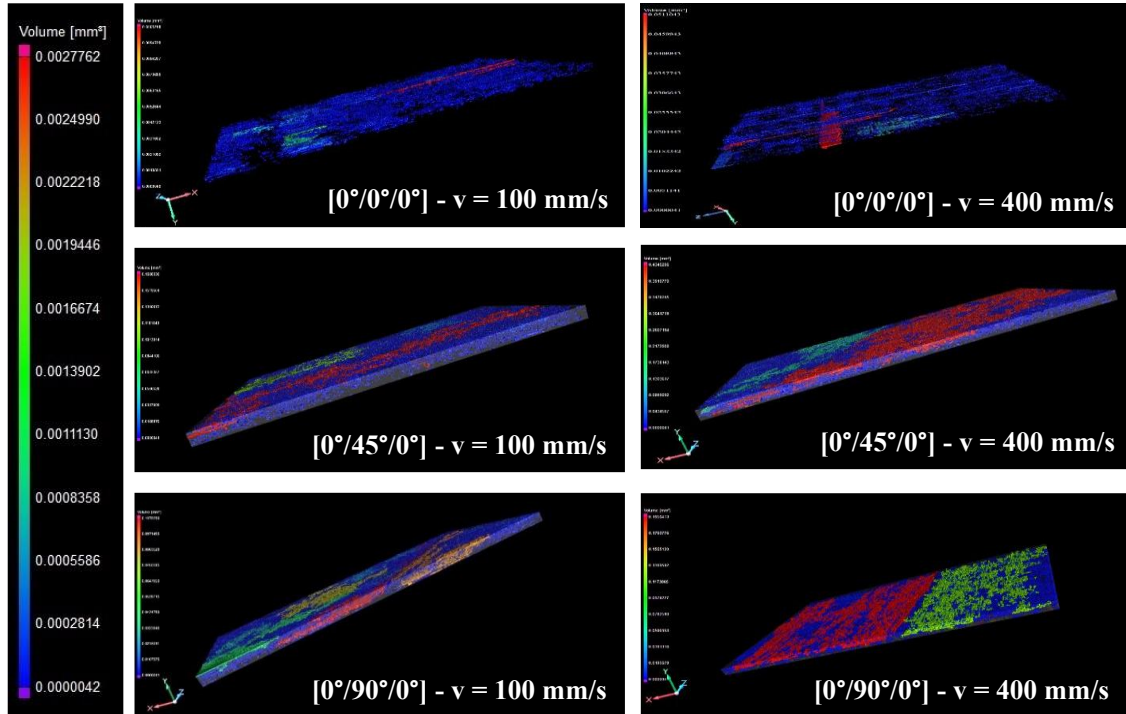


Figure 37. Micro-CT scans of CF/PEKK laminates fabricated using LAFP with three stacking sequences ([0°/0°/0°], [0°/45°/0°], [0°/90°/0°]) and two layup velocities (100 mm/s and 400 mm/s).

These findings reveal that the increase in lay-up velocity leads to larger equivalent radii and higher porosity in the samples. Additionally, the [0°/90°/0°] stacking sequence consistently exhibits greater porosity and permeability compared to the [0°/45°/0°] sequence at both lay-up velocities, indicating that the fiber orientation significantly impacts the void distribution and the permeability characteristics of the composites.

Table 11 presents the micro-CT permeability analysis (which is described in Section 4.2.2) for different stacking sequences of composite samples at lay-up velocities of 100 mm/s and 400 mm/s. The parameters assessed include the equivalent radius (R_{eq}), porosity (\emptyset), and the permeability over porosity (K_g/\emptyset) for each configuration. Notably, for UD stacking sequences (Sample #1 and 4), a cross-section with almost no voids was observed, indicating the absence of interconnected voids throughout the length of the sample, and consequently, the lack of a continuous fluid flow channel.

Table 11. Micro-CT analysis results for equivalent radius, porosity, and permeability over porosity for various stacking sequences at different lay-up velocities.

Sample No.	Lay-up velocity (mm/s)	R_{eq} (mm)	ϕ	K_g/ϕ (mm ²)
1	100	-	-	-
2	100	4.88E-03	0.12	2.48E-5
3	100	7.98E-03	0.21	3.79E-5
4	400	-	-	-
5	400	8.16E-03	0.18	4.62E-5
6	400	1.15E-02	0.28	5.93E-5

Figure 38 illustrates the comparison of permeability over porosity (K_g/ϕ) values obtained using the pulse-decay method (PDM) and micro-CT (μ CT) analysis for two stacking sequences, $[0^\circ/45^\circ/0^\circ]$ and $[0^\circ/90^\circ/0^\circ]$, at two different lay-up velocities (100 mm/s and 400 mm/s). The results indicate that while there is no universal trend in the permeability values between the PDM and μ CT methods, their alignment across different conditions supports the validity of both approaches for assessing permeability. The close agreement observed suggests that micro-CT imaging, which operates at smaller scales, provides permeability over porosity values comparable to those obtained through PDM, which typically considers larger-scale measurements.

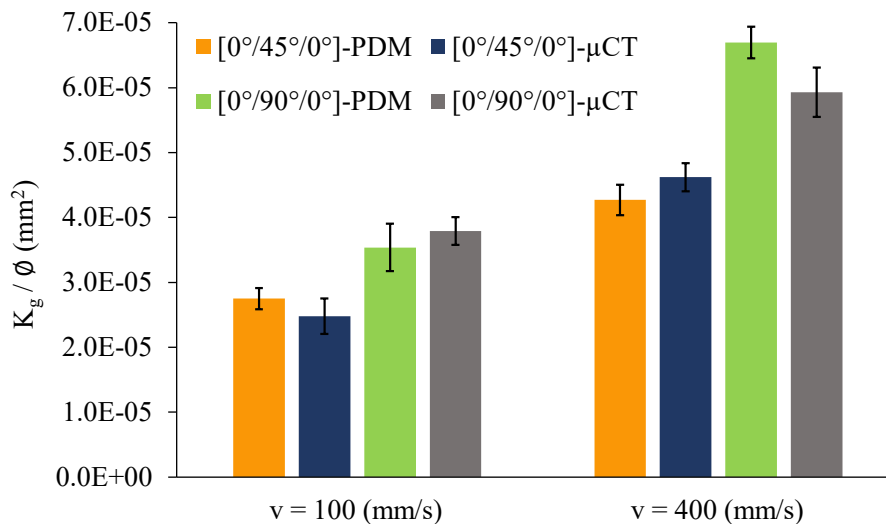


Figure 38. Comparison of permeability determined using the pulse-decay method (PDM) and micro-CT (μ CT) for $[0^\circ/45^\circ/0^\circ]$ and $[0^\circ/90^\circ/0^\circ]$ laminates at flow velocities of 100 mm/s and 400 mm/s.

This finding underscores the potential of using micro-CT as a reliable and efficient method for permeability evaluation in AFP-manufactured composite parts, particularly for sampling in stabilized regions of the part where process parameters are consistent. Such an approach can streamline permeability assessment processes, offering detailed insights while reducing dependency on larger-scale experimental setups.

4.4. Summary

This study investigated the multi-scale permeability characterization of thermoplastic composites fabricated using Laser-Assisted Fiber Placement (LAFP), employing pulse-decay and micro-CT techniques to analyze the influence of fiber orientation and lay-up velocity on permeability and void distribution. The findings revealed that increased lay-up velocities and greater fiber orientation variations ($[0^\circ/90^\circ/0^\circ]$ and $[0^\circ/45^\circ/0^\circ]$) enhance permeability due to the formation of interconnected void networks. This underscores the critical relationship between process parameters, microstructural features, and composite quality.

The comparison between pulse-decay and micro-CT techniques demonstrated their complementary strengths, with micro-CT providing detailed insights into microstructural characteristics while yielding permeability values consistent with macro-scale pulse-decay measurements. Unidirectional stacking ($[0^\circ/0^\circ/0^\circ]$) produced laminates with minimal void content and excellent structural integrity, while off-axis stacking sequences resulted in higher permeability and porosity, offering valuable guidelines for tailoring LAFP parameters to achieve desired material properties.

Importantly, the study highlights that higher permeability, observed in laminates with off-axis and orthogonal plies, can be beneficial for Out-of-Autoclave (OoA) processes. Enhanced permeability facilitates efficient air evacuation during vacuum bagging or similar techniques, ensuring effective void reduction and improved consolidation quality. This balance between structural integrity and permeability is essential for optimizing the performance of thermoplastic composites in advanced aerospace and automotive applications.

CHAPTER 5: GENERAL CONCLUSION AND FUTURE STUDIES

5.1. General Conclusion

This thesis presents a detailed investigation into the design and optimization of thermoplastic composite manufacturing using Automated Fiber Placement (AFP) with a focus on in-situ consolidation. The growing demand for lightweight and high-performance materials, particularly in aerospace and automotive industries, has driven the need for advanced manufacturing techniques capable of meeting stringent performance requirements. In this context, this research provides significant contributions to understanding and advancing AFP technology for thermoplastic composites, particularly CF/PEKK laminates. The major findings and contributions of this work are summarized below:

1. Thermal Dynamics and Process Modeling:

- A key focus of this study was understanding the thermal dynamics during the AFP process. A comprehensive thermal model was developed, incorporating thermal contact resistance to predict the temperature history at the tape-substrate interface accurately.
- Validation of the thermal model through experimental data demonstrated its robustness and applicability, showing that factors such as fiber orientation and layup speed significantly influence the temperature distribution and subsequent consolidation quality.
- The study highlighted the importance of temperature control in achieving uniform bonding and reducing defects, providing a foundational understanding for future process optimization.

2. Improving Interlaminar Bonding Quality:

- Interlaminar bonding, a critical determinant of composite performance, was rigorously analyzed. By introducing a novel correction factor approach, this research improved the predictive accuracy of bonding quality models.
- Experimental investigations confirmed that fiber orientation and processing parameters, such as layup speed and pressure, directly affect the degree of intimate contact and interlaminar bonding strength.
- The findings underscore the ability to enhance structural integrity through informed adjustments to AFP parameters, paving the way for more reliable and high-performing thermoplastic laminates.

3. Permeability and Microstructural Analysis:

- Multi-scale permeability analysis was carried out using pulse-decay and micro-computed tomography (micro-CT) methods. These techniques offered complementary insights into porosity, permeability, and microstructural characteristics of the manufactured composites.
- Results revealed the interdependence between process parameters, microstructural features, and permeability, highlighting areas where parameter optimization could lead to reduced void content and improved mechanical properties.

4. Experimental Validation and Practical Relevance:

- The combination of experimental and numerical methods throughout the research ensured that the models and hypotheses were grounded in practical application. This validation reinforces the relevance of the findings to industrial contexts, where precision and reproducibility are critical.
- Recommendations for optimizing AFP parameters, including adjustments to laser power, consolidation force, and layup speed, are directly applicable to real-world manufacturing processes.

5. Broader Impact and Framework:

- This work offers a comprehensive framework for integrating advanced manufacturing techniques with materials science to address industry challenges. It bridges gaps in existing knowledge, particularly concerning the thermal and mechanical behavior of CF/PEKK composites under AFP.
- The research contributes to a deeper understanding of how AFP parameters interact with material properties, offering pathways for developing more sustainable, efficient, and high-quality composite manufacturing processes.

In summary, this thesis not only advances the theoretical understanding of thermoplastic composite manufacturing but also provides actionable insights that can drive innovation in high-performance industries. By addressing key challenges in AFP, such as thermal control, bonding quality, and microstructural optimization, this work establishes a solid foundation for further advancements in automated composite manufacturing technologies.

5.2. Future Studies

While this thesis has addressed critical aspects of thermoplastic composite manufacturing using AFP, there are still areas that warrant further research to improve the process and its applications. The following are suggested directions for future studies:

1. Refinement of Process Parameters:

- Further investigation into the optimization of layup speed, consolidation pressure, and laser power to improve bonding quality and reduce void formation.
- Exploration of the effects of different stacking sequences on thermal and mechanical performance.

2. Material Developments:

- Testing alternative thermoplastic resins or hybrid materials to enhance bonding strength and thermal stability.

- Study of fiber-matrix interactions to improve interlaminar bonding and overall composite performance.

3. Advanced Optimization Techniques:

- Application of machine learning algorithms to optimize thermal and mechanical conditions dynamically, enabling more efficient and adaptive AFP processes.

4. Sustainability Focus:

- Investigating recycling methods for CF/PEKK composites and assessing their environmental impact.
- Developing strategies to make AFP processes more energy-efficient and cost-effective.

5. Application Expansion:

- Exploring the use of AFP technology for other high-performance industries, such as automotive and renewable energy, where lightweight materials are in demand.

These studies will build on the findings of this thesis and contribute to further advancements in AFP technology and thermoplastic composite manufacturing.

REFERENCES

- [1] P. K. Mallick, “Fiber-Reinforced Composites : Materials, Manufacturing, and Design, Third Edition,” Nov. 2007, doi: 10.1201/9781420005981.
- [2] R. F. . Gibson, “Principles of composite material mechanics,” p. 653, 2012.
- [3] A. Brent. Strong and C. A. . Ploskonka, “Fundamentals of composites manufacturing: materials, methods and applicationsA. Brent Strong, edited by Catherine A. Plonska Society of Manufacturing Engineers, USA, 1989 ISBN 0-87263-358-6, *Composites Manufacturing*, p. 252, Jan. 1991, Accessed: Dec. 24, 2024.
- [4] A. R. Offringa, “Thermoplastic composites—rapid processing applications,” *Compos Part A Appl Sci Manuf*, vol. 27, no. 4, pp. 329–336, Jan. 1996, doi: 10.1016/1359-835X(95)00048-7.
- [5] T. Choupin, “Mechanical performances of PEKK thermoplastic composites linked to their processing parameters,” 2017.
- [6] F. C. Campbell, “Manufacturing Processes for Advanced Composites,” *Manufacturing Processes for Advanced Composites*, pp. 1–517, Jan. 2003, doi: 10.1016/B978-1-85617-415-2.X5000-X.
- [7] D. H. J. A. Lukaszewicz, C. Ward, and K. D. Potter, “The engineering aspects of automated prepreg layup: History, present and future,” *Compos B Eng*, vol. 43, no. 3, pp. 997–1009, Apr. 2012, doi: 10.1016/J.COMPOSITESB.2011.12.003.
- [8] F. Islam, C. Wanigasekara, G. Rajan, A. Swain, and B. G. Prusty, “An approach for process optimisation of the Automated Fibre Placement (AFP) based thermoplastic composites manufacturing using Machine Learning, photonic sensing and thermo-mechanics modelling,” *Manuf Lett*, vol. 32, pp. 10–14, Apr. 2022, doi: 10.1016/J.MFGLET.2022.01.002.

- [9] K. Yassin and M. Hojjati, "Processing of thermoplastic matrix composites through automated fiber placement and tape laying methods: A review," *Journal of Thermoplastic Composite Materials*, vol. 31, no. 12, pp. 1676–1725, Dec. 2018, doi: 10.1177/0892705717738305/ASSET/IMAGES/LARGE/10.1177_0892705717738305-FIG14.JPEG.
- [10] M. J. Donough, Shafaq, N. A. St John, A. W. Philips, and B. Gangadhara Prusty, "Process modelling of In-situ consolidated thermoplastic composite by automated fibre placement – A review," *Compos Part A Appl Sci Manuf*, vol. 163, p. 107179, Dec. 2022, doi: 10.1016/J.COMPOSITESA.2022.107179.
- [11] I. Martin, D. Saenz Del Castillo, A. Fernandez, and A. Güemes, "Advanced Thermoplastic Composite Manufacturing by In-Situ Consolidation: A Review," *Journal of Composites Science 2020, Vol. 4, Page 149*, vol. 4, no. 4, p. 149, Oct. 2020, doi: 10.3390/JCS4040149.
- [12] U. P. Breuer, "Commercial aircraft composite technology," *Commercial Aircraft Composite Technology*, pp. 1–257, Jan. 2016, doi: 10.1007/978-3-319-31918-6.
- [13] A. Brasington, C. Sacco, J. Halbritter, R. Wehbe, and R. Harik, "Automated fiber placement: A review of history, current technologies, and future paths forward," *Composites Part C: Open Access*, vol. 6, p. 100182, Oct. 2021, doi: 10.1016/J.JCOMC.2021.100182.
- [14] E. Oromiehie, B. G. Prusty, P. Compston, and G. Rajan, "Automated fibre placement based composite structures: Review on the defects, impacts and inspections techniques," *Compos Struct*, vol. 224, p. 110987, Sep. 2019, doi: 10.1016/J.COMPSTRUCT.2019.110987.
- [15] R. Schledjewski, "Thermoplastic tape placement process – in situ consolidation is reachable," *Plastics, Rubber and Composites*, vol. 38, no. 9–10, pp. 379–386, Dec. 2009, doi: 10.1179/146580109X12540995045804.
- [16] W. J. B. Groupe, "Weld strength of laser-assisted tape-placed thermoplastic composites," Aug. 2012, doi: 10.3990/1.9789036533928.
- [17] C. M. Stokes-Griffin and P. Compston, "The effect of processing temperature and placement rate on the short beam strength of carbon fibre–PEEK manufactured

- using a laser tape placement process,” *Compos Part A Appl Sci Manuf*, vol. 78, pp. 274–283, Nov. 2015, doi: 10.1016/J.COMPOSITESA.2015.08.008.
- [18] J. Tierney and J. W. Gillespie, “Modeling of In Situ Strength Development for the Thermoplastic Composite Tow Placement Process,” <http://dx.doi.org/10.1177/0021998306060162>, vol. 40, no. 16, pp. 1487–1506, Aug. 2006, doi: 10.1177/0021998306060162.
- [19] H. Xiong, N. Hamila, and P. Boisse, “Consolidation Modeling during Thermoforming of Thermoplastic Composite Prepregs,” *Materials 2019, Vol. 12, Page 2853*, vol. 12, no. 18, p. 2853, Sep. 2019, doi: 10.3390/MA12182853.
- [20] A. Leon, C. Argerich, A. Barasinski, E. Soccard, and F. Chinesta, “Effects of material and process parameters on in-situ consolidation,” *International Journal of Material Forming*, vol. 12, no. 4, pp. 491–503, Jul. 2019, doi: 10.1007/S12289-018-1430-7/FIGURES/18.
- [21] F. Yang and R. Pitchumani, “A fractal Cantor set based description of interlaminar contact evolution during thermoplastic composites processing,” *J Mater Sci*, vol. 36, no. 19, pp. 4661–4671, Oct. 2001, doi: 10.1023/A:1017950215945/METRICS.
- [22] A. J. Comer *et al.*, “Mechanical characterisation of carbon fibre–PEEK manufactured by laser-assisted automated-tape-placement and autoclave,” *Compos Part A Appl Sci Manuf*, vol. 69, pp. 10–20, Feb. 2015, doi: 10.1016/J.COMPOSITESA.2014.10.003.
- [23] C. M. Stokes-Griffin and P. Compston, “An inverse model for optimisation of laser heat flux distributions in an automated laser tape placement process for carbon-fibre/PEEK,” *Compos Part A Appl Sci Manuf*, vol. 88, pp. 190–197, Sep. 2016, doi: 10.1016/J.COMPOSITESA.2016.05.034.
- [24] J. Tierney and J. W. Gillespie, “Modeling of Heat Transfer and Void Dynamics for the Thermoplastic Composite Tow-Placement Process,” <http://dx.doi.org/10.1177/002199803035188>, vol. 37, no. 19, pp. 1745–1768, Oct. 2003, doi: 10.1177/002199803035188.
- [25] S. Ranganathan, S. G. Advani, and M. A. Lamontia, “A Non-Isothermal Process Model for Consolidation and Void Reduction during In-Situ Tow Placement of

- Thermoplastic Composites,” *J Compos Mater*, vol. 29, no. 8, pp. 1040–1062, 1995, doi: 10.1177/002199839502900803.
- [26] T. Bayerl, M. Brzeski, M. Martínez-Tafalla, R. Schledjewski, and P. Mitschang, “Thermal degradation analysis of short-time heated polymers,” *Journal of Thermoplastic Composite Materials*, vol. 28, no. 3, pp. 390–414, Mar. 2015, doi: 10.1177/0892705713486122/ASSET/IMAGES/LARGE/10.1177_0892705713486122-FIG14.JPEG.
- [27] S. Van Hoa, M. Duc Hoang, and J. Simpson, “Manufacturing procedure to make flat thermoplastic composite laminates by automated fibre placement and their mechanical properties,” *Journal of Thermoplastic Composite Materials*, vol. 30, no. 12, pp. 1693–1712, Dec. 2017, doi: 10.1177/0892705716662516/ASSET/IMAGES/LARGE/10.1177_0892705716662516-FIG14.JPEG.
- [28] F. O. Sonmez and H. T. Hahn, “Analysis of the On-Line Consolidation Process in Thermoplastic Composite Tape Placement,” <http://dx.doi.org/10.1177/089270579701000604>, vol. 10, no. 6, pp. 543–572, Nov. 1997, doi: 10.1177/089270579701000604.
- [29] D. Ray *et al.*, “Fracture toughness of carbon fiber/polyether ether ketone composites manufactured by autoclave and laser-assisted automated tape placement,” *J Appl Polym Sci*, vol. 132, no. 11, Mar. 2015, doi: 10.1002/APP.41643.
- [30] C. M. Pistor and S. I. Güçeri, “Crystallinity of On-Line Consolidated Thermoplastic Composites,” *J Compos Mater*, vol. 33, no. 4, pp. 306–324, 1999, doi: 10.1177/002199839903300401.
- [31] A. Levy, D. Heider, J. Tierney, and J. W. Gillespie, “Inter-layer thermal contact resistance evolution with the degree of intimate contact in the processing of thermoplastic composite laminates,” *J Compos Mater*, vol. 48, no. 4, pp. 491–503, Feb. 2014, doi: 10.1177/0021998313476318/ASSET/IMAGES/LARGE/10.1177_0021998313476318-FIG10.JPEG.

- [32] T. Kok, "On the consolidation quality in laser assisted fiber placement: The role of the heating phase," Sep. 2018, doi: 10.3990/1.9789036546065.
- [33] Q. I. Zhao, S. V. Hoa, and Z. J. Gao, "Thermal stresses in rings of thermoplastic composites made by automated fiber placement process," *Science and Engineering of Composite Materials*, vol. 18, no. 1–2, pp. 35–49, Jun. 2011, doi: 10.1515/SECM.2011.006/MACHINEREADABLECITATION/RIS.
- [34] Z. Li, T. Yang, and Y. Du, "Dynamic finite element simulation and transient temperature field analysis in thermoplastic composite tape lay-up process," *Journal of Thermoplastic Composite Materials*, vol. 28, no. 4, pp. 558–573, Apr. 2015, doi: 10.1177/0892705713486135/ASSET/IMAGES/LARGE/10.1177_0892705713486135-FIG9.JPEG.
- [35] A. Kollmannsberger, R. Lichtinger, F. Hohenester, C. Ebel, and K. Drechsler, "Numerical analysis of the temperature profile during the laser-assisted automated fiber placement of CFRP tapes with thermoplastic matrix," *Journal of Thermoplastic Composite Materials*, vol. 31, no. 12, pp. 1563–1586, Dec. 2018, doi: 10.1177/0892705717738304/ASSET/IMAGES/LARGE/10.1177_0892705717738304-FIG17.JPEG.
- [36] O. Çelik *et al.*, "The influence of inter-laminar thermal contact resistance on the cooling of material during laser assisted fiber placement," *Compos Part A Appl Sci Manuf*, vol. 145, p. 106367, Jun. 2021, doi: 10.1016/J.COMPOSITESA.2021.106367.
- [37] G. Jeyakodi, "Finite Element Simulation of the In - Situ AFP process for Thermoplastic Composites using Abaqus," 2016.
- [38] C. M. Stokes-Griffin and P. Compston, "A combined optical-thermal model for near-infrared laser heating of thermoplastic composites in an automated tape placement process," *Compos Part A Appl Sci Manuf*, vol. 75, pp. 104–115, Aug. 2015, doi: 10.1016/J.COMPOSITESA.2014.08.006.

- [39] J. Reichardt, I. Baran, and R. Akkerman, “New analytical and numerical optical model for the laser assisted tape winding process,” *Compos Part A Appl Sci Manuf*, vol. 107, pp. 647–656, Apr. 2018, doi: 10.1016/J.COMPOSITESA.2018.01.029.
- [40] J. Jiang *et al.*, “Effect of Nesting on the Permeability of Multilayer Unidirectional Fabrics,” *Applied Composite Materials*, vol. 24, no. 3, pp. 625–642, Jun. 2017, doi: 10.1007/S10443-016-9531-2/FIGURES/12.
- [41] O. Çelik, D. Peeters, C. Dransfeld, and J. Teuwen, “Intimate contact development during laser assisted fiber placement: Microstructure and effect of process parameters,” *Compos Part A Appl Sci Manuf*, vol. 134, p. 105888, Jul. 2020, doi: 10.1016/J.COMPOSITESA.2020.105888.
- [42] H. S. Sas, E. B. Wurtzel, P. Simacek, and S. G. Advani, “Effect of relative ply orientation on the through-thickness permeability of unidirectional fabrics,” *Compos Sci Technol*, vol. 96, pp. 116–121, May 2014, doi: 10.1016/J.COMPSCITECH.2014.03.007.
- [43] C. Ageorges, L. Ye, Y. W. Mai, and M. Hou, “Characteristics of resistance welding of lap shear coupons. Part I: Heat transfer,” *Compos Part A Appl Sci Manuf*, vol. 29, no. 8, pp. 899–909, 1998, doi: 10.1016/S1359-835X(98)00022-0.
- [44] W. Il Lee and G. S. Springer, “A Model of the Manufacturing Process of Thermoplastic Matrix Composites,” *J Compos Mater*, vol. 21, no. 11, pp. 1017–1055, 1987, doi: 10.1177/002199838702101103.
- [45] P. M. Schaefer, T. Guglhoer, M. G. R. Sause, and K. Drechsler, “Development of intimate contact during processing of carbon fiber reinforced Polyamide-6 tapes,” *Journal of Reinforced Plastics and Composites*, vol. 36, no. 8, pp. 593–607, Apr. 2017, doi: 10.1177/0731684416687041/ASSET/IMAGES/LARGE/10.1177_0731684416687041-FIG15.JPEG.
- [46] N. L. Batista, P. Olivier, G. Bernhart, M. C. Rezende, and E. C. Botelho, “Correlation between degree of crystallinity, morphology and mechanical properties of PPS/carbon fiber laminates,” *Materials Research*, vol. 19, no. 1, pp. 195–201, Feb. 2016, doi: 10.1590/1980-5373-MR-2015-0453.

- [47] L. Quiroga Cortés, N. Caussé, E. Dantras, A. Lonjon, and C. Lacabanne, “Morphology and dynamical mechanical properties of poly ether ketone ketone (PEKK) with meta phenyl links,” *J Appl Polym Sci*, vol. 133, no. 19, May 2016, doi: 10.1002/APP.43396.
- [48] M. Di Francesco, L. Veldenz, G. Dell’Anno, and K. Potter, “Heater power control for multi-material, variable speed Automated Fibre Placement,” *Compos Part A Appl Sci Manuf*, vol. 101, pp. 408–421, Oct. 2017, doi: 10.1016/J.COMPOSITESA.2017.06.015.
- [49] C. M. Stokes-Griffin and P. Compston, “Optical characterisation and modelling for oblique near-infrared laser heating of carbon fibre reinforced thermoplastic composites,” *Opt Lasers Eng*, vol. 72, pp. 1–11, Sep. 2015, doi: 10.1016/J.OPTLASENG.2015.03.016.
- [50] A. Danezis, D. Williams, M. Edwards, and A. A. Skordos, “Heat transfer modelling of flashlamp heating for automated tape placement of thermoplastic composites,” *Compos Part A Appl Sci Manuf*, vol. 145, p. 106381, Jun. 2021, doi: 10.1016/J.COMPOSITESA.2021.106381.
- [51] R. C. Lam and J. L. Kardos, “The permeability and compressibility of aligned and cross-plyed carbon fiber beds during processing of composites,” *Polym Eng Sci*, vol. 31, no. 14, pp. 1064–1070, Jul. 1991, doi: 10.1002/PEN.760311411.
- [52] V. Le Louët *et al.*, “Directional spectral reflectivity measurements of a carbon fibre reinforced composite up to 450 °C,” *Int J Heat Mass Transf*, vol. 112, pp. 882–890, Sep. 2017, doi: 10.1016/J.IJHEATMASSTRANSFER.2017.04.125.
- [53] N. Lona Batista, K. Anagnostopoulos, E. Cocchieri Botelho, and H. Kim, “Influence of crystallinity on interlaminar fracture toughness and impact properties of polyphenylene sulfide/carbon fiber laminates,” *Eng Fail Anal*, vol. 119, p. 104976, Jan. 2021, doi: 10.1016/J.ENGFAILANAL.2020.104976.
- [54] J. Cousineau, “Effect of Cooling Rate and Mold Counter Pressure on the Crystallinity and Foaming Control In Microcellular Injection Molded Polypropylene Parts,” 2012.
- [55] T. Aized and B. Shirinzadeh, “Robotic fiber placement process analysis and optimization using response surface method,” *The International Journal of*

- Advanced Manufacturing Technology*, vol. 55, no. 1–4, pp. 393–404, Jul. 2011, doi: 10.1007/s00170-010-3028-1.
- [56] D. H. J. A. Lukaszewicz, C. Ward, and K. D. Potter, “The engineering aspects of automated prepreg layup: History, present and future,” *Compos B Eng*, vol. 43, no. 3, pp. 997–1009, 2012, doi: 10.1016/j.compositesb.2011.12.003.
- [57] F. N. Cogswell, *Thermoplastic aromatic polymer composites: a study of the structure, processing and properties of carbon fibre reinforced polyetheretherketone and related materials*. Elsevier, 2013.
- [58] O. Baho, G. Ausias, Y. Grohens, M. Barile, L. Lecce, and J. Férec, “Automated fibre placement process for a new hybrid material: A numerical tool for predicting an efficient heating law,” *Compos Part A Appl Sci Manuf*, vol. 144, p. 106360, May 2021, doi: 10.1016/j.compositesa.2021.106360.
- [59] D. Heider, M. J. Piovoso, and J. W. Gillespie, “A neural network model-based open-loop optimization for the automated thermoplastic composite tow-placement system,” *Compos Part A Appl Sci Manuf*, vol. 34, no. 8, pp. 791–799, Aug. 2003, doi: 10.1016/S1359-835X(03)00120-9.
- [60] G. Doll, “Thermoplastic composites technologies for future aircraft structures,” in *Vehicles of Tomorrow 2019: Concepts-Materials-Design*, Springer, 2021, pp. 129–138.
- [61] W. J. B. Grouve, L. L. Warnet, and R. Akkerman, “Critical assessment of the mandrel peel test for fiber reinforced thermoplastic laminates,” *Eng Fract Mech*, vol. 101, pp. 96–108, Mar. 2013, doi: 10.1016/j.engfracmech.2012.07.005.
- [62] S. C. Dai and L. Ye, “Characteristics of CF/PEI tape winding process with on-line consolidation,” *Compos Part A Appl Sci Manuf*, vol. 33, no. 9, pp. 1227–1238, Sep. 2002, doi: 10.1016/S1359-835X(02)00083-0.
- [63] M. Hou, L. Ye, H. J. Lee, and Y. W. Mai, “Manufacture of a carbon-fabric-reinforced polyetherimide (CF/PEI) composite material,” *Compos Sci Technol*, vol. 58, no. 2, pp. 181–190, Jan. 1998, doi: 10.1016/S0266-3538(97)00117-6.
- [64] E. F. Sukur, S. Elmas, V. Eskizeybek, H. S. Sas, and M. Yildiz, “An experimental implication of long-term hot-wet-aged carbon fiber/polyether ketone ketone

- composites: The impact of automated fiber placement process parameters and process-induced defects,” *J Appl Polym Sci*, vol. 140, no. 29, Aug. 2023, doi: 10.1002/app.54076.
- [65] H. Liu *et al.*, “Modelling damage in fibre-reinforced thermoplastic composite laminates subjected to three-point bend loading,” *Compos Struct*, vol. 236, p. 111889, Mar. 2020, doi: 10.1016/j.compstruct.2020.111889.
- [66] K. Shirasu, J. Tsuyuki, R. Higuchi, S. Onodera, and T. Okabe, “Experimental and numerical study on open-hole tension/compression properties of carbon-fiber-reinforced thermoplastic laminates,” *J Compos Mater*, vol. 56, no. 14, pp. 2211–2225, Jun. 2022, doi: 10.1177/00219983221096880.
- [67] Z. Zhang, Y. Long, Z. Yang, K. Fu, and Y. Li, “An investigation into printing pressure of 3D printed continuous carbon fiber reinforced composites,” *Compos Part A Appl Sci Manuf*, vol. 162, p. 107162, Nov. 2022, doi: 10.1016/j.compositesa.2022.107162.
- [68] Y. Hoshikawa, K. Shirasu, R. Higuchi, Y. Kawagoe, H. Tohmyoh, and T. Okabe, “Experimental and numerical investigation of the relationship between material defects and elastoplasticity behavior of 3D-printed carbon-fiber-reinforced thermoplastics under compressive loading,” *Compos Sci Technol*, vol. 241, p. 110116, Aug. 2023, doi: 10.1016/j.compscitech.2023.110116.
- [69] C. M. Stokes-Griffin and P. Compston, “Investigation of sub-melt temperature bonding of carbon-fibre/PEEK in an automated laser tape placement process,” *Compos Part A Appl Sci Manuf*, vol. 84, pp. 17–25, May 2016, doi: 10.1016/J.COMPOSITESA.2015.12.019.
- [70] N. Heathman, P. Koirala, T. Yap, A. Emami, and M. Tehrani, “In situ consolidation of carbon fiber PAEK via laser-assisted automated fiber placement,” *Compos B Eng*, vol. 249, p. 110405, Jan. 2023, doi: 10.1016/j.compositesb.2022.110405.
- [71] J. Avenet, T. A. Cender, S. Le Corre, J.-L. Bailleul, and A. Levy, “Adhesion of High Temperature Thermoplastic Composites,” *Procedia Manuf*, vol. 47, pp. 925–932, 2020, doi: 10.1016/j.promfg.2020.04.284.

- [72] F. Yang and R. Pitchumani, "Healing of thermoplastic polymers at an interface under nonisothermal conditions," *Macromolecules*, vol. 35, no. 8, pp. 3213–3224, 2002.
- [73] K. Shirasu, Y. Yamaguchi, Y. Hoshikawa, G. Kikugawa, H. Tohmyoh, and T. Okabe, "Micromechanics study of short carbon fiber-reinforced thermoplastics fabricated via 3D printing using design of experiments," *Materials Science and Engineering: A*, vol. 891, p. 145971, Jan. 2024, doi: 10.1016/j.msea.2023.145971.
- [74] C. Yildirim, I. E. Tabrizi, A. Al-Nadhari, S. Topal, B. Beylergil, and M. Yildiz, "Characterizing damage evolution of CF/PEKK composites under tensile loading through multi-instrument structural health monitoring techniques," *Compos Part A Appl Sci Manuf*, vol. 175, p. 107817, Dec. 2023, doi: 10.1016/j.compositesa.2023.107817.
- [75] P. H. Dara and A. C. Loos, "Thermoplastic matrix composite processing model," 1985.
- [76] S. C. Mantell and G. S. Springer, "Manufacturing process models for thermoplastic composites," *J Compos Mater*, vol. 26, no. 16, pp. 2348–2377, 1992, doi: 10.1177/002199839202601602.
- [77] A. Khodaei and F. Shadmehri, "Intimate contact development for automated fiber placement of thermoplastic composites," *Composites Part C: Open Access*, vol. 8, p. 100290, 2022.
- [78] W. J. B. Grouve, L. L. Warnet, B. Rietman, H. A. Visser, and R. Akkerman, "Optimization of the tape placement process parameters for carbon–PPS composites," *Compos Part A Appl Sci Manuf*, vol. 50, pp. 44–53, Jul. 2013, doi: 10.1016/J.COMPOSITESA.2013.03.003.
- [79] C. A. Butler, R. L. Mccullough, R. Pitchumani, and J. W. Gillespie, "An Analysis of Mechanisms Governing Fusion Bonding of Thermoplastic Composites," *Journal of Thermoplastic Composite Materials*, vol. 11, no. 4, pp. 338–363, Jul. 1998, doi: 10.1177/089270579801100404.
- [80] P. G. de Gennes, "Reptation of a Polymer Chain in the Presence of Fixed Obstacles," *J Chem Phys*, vol. 55, no. 2, pp. 572–579, Jul. 1971, doi: 10.1063/1.1675789.

- [81] Rp. Wool and K. M. O’connor, “A theory crack healing in polymers,” *J Appl Phys*, vol. 52, no. 10, pp. 5953–5963, 1981.
- [82] L. J. Bastien and J. W. Gillespie Jr, “A non-isothermal healing model for strength and toughness of fusion bonded joints of amorphous thermoplastics,” *Polym Eng Sci*, vol. 31, no. 24, pp. 1720–1730, 1991.
- [83] F. Yang and R. Pitchumani, “Nonisothermal Healing and Interlaminar Bond Strength Evolution During Thermoplastic Matrix Composites Processing,” *Polym Compos*, vol. 24, no. 2, pp. 263–278, 2003, doi: 10.1002/pc.10027.
- [84] M. A. Khan, P. Mitschang, and R. Schledjewski, “Identification of some optimal parameters to achieve higher laminate quality through tape placement process,” *Advances in Polymer Technology*, vol. 29, no. 2, pp. 98–111, Jul. 2010, doi: 10.1002/adv.20177.
- [85] C. M. Stokes-Griffin and P. Compston, “Laser-assisted tape placement of thermoplastic composites: the effect of process parameters on bond strength,” in *Sustainable Automotive Technologies 2013: Proceedings of the 5th International Conference ICSAT 2013*, Springer, 2013, pp. 133–141.
- [86] E. F. Sukur, S. Elmas, M. Seyyednourani, V. Eskizeybek, M. Yildiz, and H. S. Sas, “A rational study on the hydrothermal aging of AFP manufactured CF/polyetherketoneketone composites with in situ consolidation supported by acoustic emission inspection,” *J Appl Polym Sci*, no. January, pp. 1–14, Apr. 2022, doi: 10.1002/app.52480.
- [87] Toray, “Toray Cetex ® TC1320 PEKK PRODUCT DATA SHEET,” vol. 31, no. 0, pp. 1–3, 2019.
- [88] C. M. Stokes-Griffin, A. Kollmannsberger, P. Compston, and K. Drechsler, “The effect of processing temperature on wedge peel strength of CF/PA 6 laminates manufactured in a laser tape placement process,” *Compos Part A Appl Sci Manuf*, vol. 121, pp. 84–91, 2019.
- [89] A. Barzegar, S. Karimi, E. F. Sukur, H. S. Sas, and M. Yildiz, “Effect of fiber orientation on temperature history during laser-assisted thermoplastic fiber placement,” *Journal of Reinforced Plastics and Composites*, p. 073168442211434, Nov. 2022, doi: 10.1177/07316844221143448.

- [90] H.-R. Lin and S. G. Advani, "Processing models and characterization of thermoplastic composite wound parts," *Polym Compos*, vol. 18, no. 3, pp. 405–411, Jun. 1997, doi: 10.1002/pc.10291.
- [91] D. Zhang, D. Heider, and J. W. Gillespie, "Characterization of interlayer air permeability of thermoplastic prepreg stacks," *J Compos Mater*, vol. 52, no. 6, pp. 731–745, Mar. 2018, doi: 10.1177/0021998317715089/ASSET/IMAGES/LARGE/10.1177_0021998317715089-FIG18.JPEG.
- [92] K. Ramaswamy, V. Modi, P. S. Rao, P. P. Martin, C. T. McCarthy, and R. M. O'Higgins, "An investigation of the influence of matrix properties and fibre–matrix interface behaviour on the mechanical performance of carbon fibre-reinforced PEKK and PEEK composites," *Compos Part A Appl Sci Manuf*, vol. 165, p. 107359, Feb. 2023, doi: 10.1016/j.compositesa.2022.107359.
- [93] V. T. Hoang *et al.*, "Postprocessing method-induced mechanical properties of carbon fiber-reinforced thermoplastic composites," *Journal of Thermoplastic Composite Materials*, vol. 36, no. 1, pp. 432–447, Jan. 2023, doi: 10.1177/0892705720945376/ASSET/IMAGES/LARGE/10.1177_0892705720945376-FIG6.JPEG.
- [94] J. Chen, T. Chen-Keat, M. Hojjati, A. Vallee, M. A. Oceau, and A. Yousefpour, "Impact of layup rate on the quality of fiber steering/cut-restart in automated fiber placement processes," *Science and Engineering of Composite Materials*, vol. 22, no. 2, pp. 165–173, Mar. 2015, doi: 10.1515/SECM-2013-0257/MACHINEREADABLECITATION/RIS.
- [95] O. Baho, G. Ausias, Y. Grohens, and J. Férec, "Simulation of laser heating distribution for a thermoplastic composite: effects of AFP head parameters," *International Journal of Advanced Manufacturing Technology*, vol. 110, no. 7–8, pp. 2105–2117, Sep. 2020, doi: 10.1007/S00170-020-05876-9/FIGURES/16.
- [96] E. Mathew and S. C. Joshi, "Effect of Roller Pressure and Base Prepreg Layer on Tensile and Flexural Properties of CFRP Laminates Fabricated Using Automated Fiber Placement," *Journal of Composites Science 2023*, Vol. 7, Page 101, vol. 7, no. 3, p. 101, Mar. 2023, doi: 10.3390/JCS7030101.

- [97] N. A. Zanjani, W. Wang, and S. Kalyanasundaram, “The effect of fiber orientation on the formability and failure behavior of a woven self-reinforced composite,” *Journal of Manufacturing Science and Engineering, Transactions of the ASME*, vol. 137, no. 5, Oct. 2015, doi: 10.1115/1.4030894/377664.
- [98] K. Xia, R. Harik, J. Herrera, J. Patel, and B. W. Grimsley, “Numerical Simulation of AFP Nip Point Temperature Prediction for Complex Geometries,” 2018.
- [99] C. Venkatesan, R. Velu, N. Vaheed, F. Raspall, T. E. Tay, and A. Silva, “Effect of process parameters on polyamide-6 carbon fibre prepreg laminated by IR-assisted automated fibre placement,” *International Journal of Advanced Manufacturing Technology*, vol. 108, no. 4, pp. 1275–1284, May 2020, doi: 10.1007/S00170-020-05230-Z/FIGURES/10.
- [100] D. Maurer and P. Mitschang, “Laser-powered tape placement process – simulation and optimization,” *Advanced Manufacturing: Polymer & Composites Science*, vol. 1, no. 3, pp. 129–137, Jul. 2015, doi: 10.1080/20550340.2015.1114798.
- [101] J. Lee *et al.*, “Advanced carbon fiber composite out-of-autoclave laminate manufacture via nanostructured out-of-oven conductive curing,” *Compos Sci Technol*, vol. 166, pp. 150–159, Sep. 2018, doi: 10.1016/J.COMPSCITECH.2018.02.031.
- [102] C. Vernejoux, X. Fischer, S. Deseur, and E. Duc, “Influence of automated fiber placement parameters on thermoplastic composite blanks used on stamp forming process,” *ESAFORM 2021 - 24th International Conference on Material Forming*, 2021, doi: 10.25518/ESAFORM21.366.
- [103] T. Centea, L. K. Grunenfelder, and S. R. Nutt, “A review of out-of-autoclave prepregs – Material properties, process phenomena, and manufacturing considerations,” *Compos Part A Appl Sci Manuf*, vol. 70, pp. 132–154, Mar. 2015, doi: 10.1016/J.COMPOSITESA.2014.09.029.
- [104] A. R. Aziz, M. A. Ali, X. Zeng, R. Umer, P. Schubel, and W. J. Cantwell, “Transverse permeability of dry fiber preforms manufactured by automated fiber placement,” *Compos Sci Technol*, vol. 152, pp. 57–67, Nov. 2017, doi: 10.1016/J.COMPSCITECH.2017.09.011.

- [105] T. A. Cender, P. Simacek, S. Davis, and S. G. Advani, “Gas Evacuation from Partially Saturated Woven Fiber Laminates,” *Transp Porous Media*, vol. 115, no. 3, pp. 541–562, Dec. 2016, doi: 10.1007/S11242-016-0784-X/FIGURES/15.
- [106] D. Zhang, “Void consolidation of thermoplastic composites via non-autoclave processing,” 2017.
- [107] T. A. Cender, P. Šimáček, and S. G. Advani, “A method to determine open pore volume with pulse decay,” *Appl Phys Lett*, vol. 105, no. 13, p. 134101, Sep. 2014, doi: 10.1063/1.4896854/385404.
- [108] P. A. Midgley, E. P. W. Ward, A. B. Hungria, and J. M. Thomas, “Nanotomography in the chemical, biological and materials sciences,” *Chem Soc Rev*, vol. 36, no. 9, pp. 1477–1494, Jul. 2007, doi: 10.1039/B701569K.
- [109] G. Möbus and B. J. Inkson, “Nanoscale tomography in materials science,” *Materials Today*, vol. 10, no. 12, pp. 18–25, Dec. 2007, doi: 10.1016/S1369-7021(07)70304-8.
- [110] J. Kastner, B. Harrer, G. Requena, and O. Brunke, “A comparative study of high resolution cone beam X-ray tomography and synchrotron tomography applied to Fe- and Al-alloys,” *NDT & E International*, vol. 43, no. 7, pp. 599–605, Oct. 2010, doi: 10.1016/J.NDTEINT.2010.06.004.
- [111] T. A. Cender, “Process analysis of manufacturing composites structures with vacuum-bag-only prepregs: quantifying partial resin impregnation and its effect on gas evacuation,” 2017, doi: 10.58088/P6P2-FJ74.
- [112] “Kozeny, J. (1927) Ueber kapillare Leitung des Wassers im Boden. Sitzungsber Akad. Wiss., Wien, 136(2a), pp 271-306. - References - Scientific Research Publishing.” Accessed: Nov. 27, 2024. [Online]. Available: <https://www.scirp.org/reference/ReferencesPapers?ReferenceID=1306904>
- [113] P. G. Carman, “Fluid flow through granular beds,” *Chemical Engineering Research and Design*, vol. 75, no. 1 SUPPL., pp. S32–S48, Dec. 1997, doi: 10.1016/S0263-8762(97)80003-2.